DOI: 10.1070/RCR4873

Metal-organic framework structures: adsorbents for natural gas storage

Aslan Yu. Tsivadze,[a] Oleg E. Aksyutin,[b] Alexander G. Ishkov,[b] Marina K. Knyazeva,[a] Olga V. Solovtsova,[a] Ilya E. Men'shchikov,[a] Anatoly A. Fomkin,[a] Andrey V. Shkolin,[a] Elena V. Khozina,[a] Vladimir A. Grachev [a]

[a] A.N.Frumkin Institute of Physical Chemistry and Electrochemistry, Russian Academy of Sciences, Leninsky prosp. 31, korpus 4, 119071 Moscow, Russian Federation
[b] Public Joint Stock Company Gazprom, ul. Nametkina 16, 117997 Moscow, Russian Federation

Natural gas (methane) forms an essential part of modern power supply. However, natural gas storage and transportation are associated with fire and explosion hazard, which restricts extensive application of natural gas as a fuel. The adsorption technique is among the most promising and safe ways for natural gas storage and transportation, which allows a significant increase in the methane density up to values characteristic of liquids as a result of physical adsorption in microporous adsorbents at moderate pressures. The review considers adsorption systems for natural gas (methane) storage based on metal-organic frameworks, which possess high characteristic energy of adsorption and a regular nanoporous structure with high pore volumes and specific surface areas. The possibility of controlling the porous structure and physicochemical behaviour of metal-organic frameworks during their synthesis and functionalization is analyzed, including the fabrication of composites and shaping, which may enhance their performance in the adsorption storage and transportation of natural gas. The bibliography includes 315 references.

Contents

1. Introduction 927
2. Microporous metal-organic frameworks 930
3. Metal-organic frameworks as methane adsorbents 943
4. Composite materials based on metal-organic frameworks 960
5. Scaled methane storage systems based on metal-organic frameworks 968
6. Conclusion 970

A.Yu.Tsivadze. Academician, Doctor of Science in Chemistry, Chief Scientific Adviser, IPCE RAS.
Telephone: +7(495)952 – 5681, e-mail: tsiv@phyche.ac.ru
O.E.Aksyutin. Doctor of Science in Engineering, Deputy Chairman of the Management Committee, PJSC Gazprom, Corresponding Member of the RAS.
Telephone: +7(812)641 – 3503, e-mail: O.Aksiutin@adm.gazprom.ru
A.G.Ishkov. Doctor of Science in Chemistry, Professor, Deputy Head of Department — Head of Division, PJSC Gazprom.
Telephone: +7(812)641 – 3614, e-mail: A.Ishkov@adm.gazprom.ru
M.K.Knyazeva. Researcher at the Laboratory of Sorption Processes, IPCE RAS.
Telephone: +7(495)952 – 5681, e-mail: Batrakovamk@mail.ru
O.V.Solovtsova. Researcher at the same Laboratory.
Telephone: +7(495)952 – 5681, e-mail: Lace25@mail.ru
I.E.Men'schikov. Candidate of Science in Chemistry, Researcher at the same Laboratory.
Telephone: +7(495)952 – 5681, e-mail: i.menschikov@mail.ru
A.A.Fomkin. Doctor of Science in Physics and Mathematics, Professor, Head of the same Laboratory.
Telephone: +7(495)952 – 5681, e-mail: fomkinaa@mail.ru
A.V.Shkolin. Candidate of Science in Chemistry, Leading Researcher of the same Laboratory.
Telephone: +7(495)952 – 5681, e-mail: shkolin@bk.ru
E.V.Khozina. Candidate of Science in Physics and Mathematics, Senior Researcher at the same Laboratory.
Telephone: +7(495)952 – 5681, e-mail: Elena-khozina@rambler.ru
V.A.Grachev. Corresponding Member of the RAS, Doctor of Science in Chemistry, Professor, Dean of the Faculty of Global Studies, MSU, Chief Researcher at the Laboratory of Highly Concentrated Disperse Systems, IPCE RAS.
Telephone: +7(495)952 – 5681, e-mail: vagrachev@gmail.com
Current research interests of the authors: physical and coordination chemistry, supramolecular structures, adsorption and adsorbents, porous materials, natural gas and gas industry, low-carbon energy, energy conservation, energy efficiency, environmental safety, green chemistry.

Received 27 December 2018
Translation: Z.P.Svitanko

© 2019 Uspekhi Khimii, Russian Academy of Sciences and Turpion Ltd.

The following designations and abbreviations are used:

a_s(BET) — Brunauer–Emmett–Teller specific surface area,

D_{fix} — fixed diameter of MOF pores,

D_{free} — free diameter of MOF pores,

d_{cr} — crystal density,

d_p — packing density,

$\varepsilon(P,T)$ — relative efficiency of an adsorption storage system,

E_0 — characteristic energy of adsorption,

H_{ad} — enthalpy of adsorption,

G_f — total gravimetric specific capacity,

G_d — deliverable gravimetric specific capacity of an adsorption storage system,

n_a — total (absolute) adsorption,

P — pressure,

p_i — parameters depending on the thermodynamic conditions of synthesis,

$\rho_g(P,T)$ — density of adsorbed substance,

q_{st} — differential molar isosteric heat of adsorption,

Q_{st} — integral molar isosteric heat of adsorption,

T — temperature,

V_d — specific deliverable volumetric capacity of an adsorption storage system,

V_f — total volumetric specific capacity,

W_t — total specific pore volum,

W_0 — specific volume of micropores,

w — concentration of a binding agent,

X_0 — characteristic size of micropores,

ABTC — azobenzene-3,3′,5,5′-tetracarboxylate,

ADC — acetylenedicarboxylate,

ADIP — 5,5′-(anthracene-9,10-diyl)diisophthalate,

AMMal — amino group modification with maleic anhydride,

ANG — adsorbed natural gas,

BBC — 4,4′,4″-[benzene-1,3,5-triyl-tris(1,1′-biphenyl)-4′-carboxylate],

BCP — 3,5-bis(4-carboxylatoanilinocarbonyl)pyridine,

BCPBD — 4,4′-(buta-1,3-diene-1,4-diyl)dibenzoate,

BTAC — benzene-1,3,5-tri-β-acrylate,

BDC — benzene-1,4-dicarboxylate,

BDCPPI — *N*,*N*′-bis(3,5-dicarboxylatophenyl)pyromellitic diimide,

BDP — 1,4-benzenedipyrazolate,

BDPP — 3,5-bis(3,5-dicarboxylatophenyl)pyridine,

BET — Brunauer–Emmett–Teller,

BHB — 3,3′,3″,5,5′,5″-(benzene-1,3,5-triyl)hexabenzoate,

BPDC — biphenyl-4,4′-dicarboxylate,

BPTC — 1,1′-(biphenyl-3,3′,5,5′)tetracarboxylate,

BPY — 4,4′-bipyridine,

BPYDB — 4,4′-(4,4′-bipyridine-2,6-diyl)dibenzoate,

BTAT — 5,5′,5″-[benzene-1,3,5-tiyltrtis(anthracene-10,9-diyl)]triisophthalate,

BTB — 4,4′,4″-(benzene-1,3,5-triyl)tribenzoate,

BTC — benzene-1,3,5-tricarboxylate,

BTE — 4,4′,4″-[benzene-1,3,5-triyl-tris(ethyne-2,1-diyl)]tribenzoate,

BTTI — 5,5′,5″-[benzene-1,3,5-triyl-tris(1*H*-1,2,3-triazole-4,1-diyl)]triisophthalate,

BTU — British thermal unit,

CNG — compressed natural gas,

CNT — carbon nanotubes.

CPO — Coordination polymers of Oslo,

DABCO — 1,4-diazabicyclo[2.2.2]octane,

DMF — dimethylformamide,

DOBPDC — 4,4′-dioxidobiphenyl-3,3′-dicarboxylate,

DOE — US Department of Energy,

DOT — 2,5-dihydroxyterephthalate,

DUT — MOFs synthesized at the Dresden University of Technology,

Fma — fumaric acid,

FJI — MOFs synthesized at the Fujian Institute of Research on the Structure of Matter,

HKUST-1 — MOFs synthesized at the Hong Kong University of Science and Technology,

HNUST — MOFs synthesized at the Hunan University of Science and Technology,

HPDC — 4,5,9,10-tetrahydropyrene-2,7-dicarboxylate,

IRMOF — isoreticular metal-organic frameworks,

LIFM — MOFs synthesized at the Lehn Institute of Functional Materials,

LNG — liquefied natural gas,

MAX-MIL — MAXISORB activated carbon and MIL-101(Cr) metal-organic framework composite,

MAF — metal azolate frameworks based on pyridine-2-carboxylic acid,

MMEN — *N*,*N*′-dimethylethylenediamine,

MFM — Manchester framework material (MOFs synthesized at the Manchester University),

MIL — materials of Institute Lavoisier,

MOF — metal-organic framework,

MOP-1 — metal-organic polyhedron,

MOVE — methane opportunities for vehicular energy, Advanced Research Project Agency of US DOE,

MTAF — metal triazolate framework,

MWCNT — multiwalled carbon nanotubes,

NDC — 1,4-naphthalenedicarboxylate,

NG — natural gas,

NJU-Bai — MOFs synthesized at the Nanjing University by Bai's group,

NOTT — isoreticular MOFs synthesized at the University of Nottingham,

NTBD — 4′,4″,4‴-nitrilotribiphenyl-3,5-dicarboxylate,

NTP — normal temperature and pressure,

NU — MOFs synthesized at the Northwestern University,

OMS — open metal sites,

PCN — porous coordination network,

PDC — pyrene-2,7-dicarboxylate,

PDDI — 5,5′-pyridine-2,5-diyl)diisophthalate,

PPN — porous polymer network,

PTEI — 5,5′,5″-[benzene-1,3,5-triyl-tris(benzene-4,1-diylethyne-2,1-diyl)]triisophthalate,

PVA — polyvinyl alcohol,

PYPZ — 2-(1*H*-pyrazol-2-yl)pyridine,

rt — room temperature,

SBU — secondary building unit,

SNU — MOFs synthesized at the Seoul University,

ST — MOFs synthesized at the Shanghai Technical University,

STP — standard temperature and pressure,

TATAB — 4,4′,4″-1,3,5-triazine-2,4,6-triyl-tribenzoate,

TATB — 5,5',5''-[1,3,5-triazine-2,4,6-triyl-tris(1,4-benzamido)]triisophthalate,

TBCPPM — tetrakis{3,5-bis[(4-carboxylato)phenyl]-phenyl}methane,

TCEPBB — 1,3,5-tris[(1,3-carboxylate-5-(4-(ethynyl)-phenyl))butadiynyl]-benzene,

TDBB — benzene-1,3,5-tris[(1,1′-biphenyl-4-yl)-3′,5′-dicarboxylate],

TDPAT — 2,4,6-tris(3,5-dicarboxylatophenylamino)-1,3,5-triazine,

TED — triethylenediamine,

TMBDI — 2,3,5,6-tetramethylbenzene-1,4-diisophthalate,
TPDC — *p*-terphenyl-4,4″-dicarboxylate,
TPT — 2,4,6-tris(4-pyridyl)-1,3,5-triazine,
TTCA — triphenylene-2,6,10-tricarboxylate,
UiO — MOFs synthesized at the Oslo University (Universitetet i Oslo),
UTSA — MOFs synthesized at the University of Texas at San Antonio,
ZIF — zeolitic imidazolate framework,
ZJNU — MOFs synthesized at the Zhejiang Normal University,
ZJU — MOFs synthesized at the Zhejiang University.

1. Introduction

The growth of Earth population and development of industry and transport generate increasing demand in the basic energy sources (oil, coal, natural gas). Depletion of oil and coal reserves, together with the environmental problems associated with their use bring about a gradual decrease in the share of oil and coal in the global energy consumption in favour of natural gas.[1] According to the International Energy Agency data, the share of natural gas in the global energy consumption was 21% in 2017, and during three quarters of 2018, the consumption of natural gas increased by 4.7% in comparison with the same period of 2017.[1–3] From the standpoint of environmental safety and human health effect, the use of natural gas as a source of energy has some advantages, the main of which are the absence of solid particulates in the combustion products and minor contents of sulfur compounds, carbon dioxide, nitrogen oxides and hydrocarbons (Table 1).[3]

The key limitations for the use of natural gas include complicated transportation and storage. Despite the extensive network of gas pipelines, gas supply is not available everywhere. These problems are partially solved by using liquefaction (LNG) and compression (CNG) techniques; however, the application of these techniques is associated with certain risks and requires expensive equipment. For example, CNG systems imply 200–250-fold compression of the mainstream gas (up to 20–25 MPa) by means of expensive high-pressure compressors, which are difficult to maintain and which do not always reliably meet safety criteria. Furthermore, for the storage of the compressed gas, strong thick-walled gas cylinders are needed. As a result, the weight of a CNG kit is >100 kg. Hence, depending on the number of CNG cylinders, the weight of the truck increases by 400–900 kg.[4] The use of compressed natural gas in transport vehicles at low winter temperatures (down to −50 °C) is faced with the problem of gas hydrate formation in the gas dispensers of filling stations, which leads to decreasing CNG pressure.[5] A vehicle can travel a 3.5 times shorter distance when operated by compressed natural gas than when operated by liquefied natural gas, with the gas cylinder volumes being equal:[4] the CNG cylinder contains a relatively small amount of natural gas, that is, ~240 $m^3\ m^{-3}$ at 20 MPa and 293 K.

The natural gas liquefaction technique implies conversion of the gas to a liquid at a temperature of −161 °C with a ~600-fold decrease in the volume. As a result, an LNG system contains a two times greater amount of the gas (~500–560 $m^3\ m^{-3}$) than a CNG system of the same volume. Liquefied gas is stored in cryogenic tanks and transported using special tankers; for conversion to the gaseous state, regasification terminals are required. On the vehicles, this gas is stored in heat-insulated cryogenic cylinders. Although LNG systems imply gas storage at a slight excessive pressure (0.2 atm) and natural gas in the liquid state is not explosive or flammable without contact with an open flame source, nevertheless, the safety requirements are very strict. Below we list the key risk factors arising during operation of LNG systems:[6, 7]

— expansion of the liquid upon a change in the system temperature; therefore, good heat insulation and strong tanks are required;
— appearance of vapour above liquefied gas, which requires the discharge;
— probability of LNG separation into two layers upon topping-up of a vessel; this may give rise to a rollover effect and finally induce transition of a part of the liquid to the gas phase, which would result in a pressure rise and possible damage of the LNG tank;
— release of the liquefied gas under pressure and explosions of gas clouds.

Note that evaporation of one cubic metre of spilled liquefied methane at −161 °C can give >600 m^3 of methane gas and, hence, >12 000 m^3 of a flammable and explosiive mixture.[8] The destruction of storage vessels, spills and explosions of gas clouds can be avoided only *via* solution of numerous engineering, thermophysical and strength problems. Thus, the economic benefits of the high energy density of LNG are largely eliminated by the complexity and high cost of cryogenic equipment, which requires skilled personnel for operation, and by the fact that LNG terminals cannot be located in the close vicinity to gas consumers for safety reasons.

For solving the above problems faced when using CNG and LNG techniques, new engineering approaches are required. For example, methane storage and transportation as gas hydrates have been proposed; it is assumed that 1 m^3 of gas hydrates can be converted to 160 m^3 of methane.[9] However, this method has not yet found practical use because of low volume of methane stored in this way and complex conditions of hydrate formation. Takeya *et al.*[10] investigated the stability of methane hydrates obtained in brine or in sea water as a function of temperature and NaCl concentration. It was found that at temperatures below the eutectic point of the $H_2O-NaCl$ system ($T = 252$ K), the CH_4 hydrates with NaCl content of up to 2.7 mass % are stable due to ice formation.

A highly promising method for natural gas storage and transportation is the adsorption storage. The benefits of this method are due, first of all, to the state of methane, the

Table 1. Emissions from the use of fossil fuels.[3]

Pollutant	Natural gas		Oil		Coal	
	see [a]	see [b]	see [a]	see [b]	see [a]	see [b]
CO_2	117 000	53.071	164 000	74.389	208 000	94.347
CO	40	0.018	33	0.015	208	0.094
NO_2	92	0.042	448	0.203	457	0.207
SO_2	1	$4.5 \cdot 10^{-4}$	1122	0.509	2591	1.175
Solid particulates	7	0.003	84	0.038	2744	1.245
Mercury	0.000	0.000	0.007	3×10^{-6}	0.016	7×10^{-6}

[a] The values are given in pounds per billion BTU (BTU is British thermal unit); [b] The values are given in tons per billion BTU.

major component of natural gas, adsorbed in microporous materials. The absence of a dipole (or quadrupole) moment and, as a consequence, the absence of electrostatic interactions of methane molecules provides their adsorption only *via* dispersion forces that arise in micropores with high characteristic energies of adsorption. The benefits of the adsorption storage of natural gas (ANG) are discussed in detail in a number of reviews of foreign [11] and Russian [12, 13] researchers. The key benefits are the following:

— storage and transportation occur at relatively low temperature (233 to 323 K);

— adsorption storage of the gas takes place at ambient pressure (lower than 3.5 MPa);

— enhanced fire and explosion safety of adsorption storage systems associated with a special nanodispersed state of the adsorbed gas molecules in the micropores, which are exposed to the field of adsorption forces.

It follows from the above factors that adsorption and storage of natural gas do not require special conditions or complex power-intensive and expensive equipment; this storage can be arranged by means of well-known reliable and rather easily implementable engineering solutions. This accounts for intensive development of practical implementations of the adsorption storage of natural gas, which started at the end of 20th century [14–18] and is still in progress.

One of the key requirements for effective adsorption storage of natural gas, which was formulated by the US Advanced Research Project Agency for the Department of Energy (DOE) in 2012, is that the gravimetric capacity for methane storage should be 0.5 g (CH_4) g(adsorbent)$^{-1}$ and the specific volumetric capacity for a monolithic block of the adsorbent should be 263 m^3 m^{-3} at a pressure of 3.5(6.5) MPa and a temperature of 298 K, which is equivalent to compressed methane storage in cylinders at 25 MPa and energy density of 9.2 MJ m^{-3} (Ref. 19).

This requirement refers to the natural gas discharge upon pressure decrease from 3.5 (6.5) to 0.1 MPa, *i.e.*, to the amount of the gas that can be extracted from the storage device and delivered to the consumer.[20] Considering the fact that the real filling of the tank with the adsorbent is 75% of the whole volume, the target requirement for an ANG system can be attained if the total volumetric capacity of an adsorption system for natural gas storage is 350 m^3 m^{-3}, which provides energy density of 12.5 MJ m^{-3}. The DOE requirements form the target for the development and implementation of ANG technology; however, these values have not been attained as yet. Thus, the search for an optimal microporous adsorbent for the design of an efficient adsorption system for natural gas storage is, beyond doubt, a relevant task. An appropriate adsorbent should possess the following properties:

— optimal relationship between the adsorption and desorption processes, that is, a material with a high adsorption capacity should be able to release the highest gas volume without additional heating;

— micropore size (0.8–1.4 nm) that would ensure gas adsorption and desorption at room temperature;

— high packing density providing a decrease in the volume of the gas phase in the storage systems;

— moderate heat of adsorption with a high heat capacity of the material to avoid thermal oscillations in the system following changes in the environmental temperature;

— extensive transport porosity to provide mass transfer;

— hydrophobicity.

It was noted [13] that a greater part of studies on methane storage are carried out using microporous carbon adsorbents obtained from different raw materials. However, studies in which metal-organic frameworks (MOFs) are proposed as adsorbents for methane storage have been appearing more and more frequently in recent years.[20–23] Indeed, MOFs possess a number of properties appropriate for adsorption materials for natural gas storage: high specific surface area, possibility of modification of functional properties and possibility to control the shape and size of pores during the synthesis.[23, 24]

The possible applications of MOFs include adsorption systems for storage and transportation of not only methane,[25, 26] but also other gases such as H_2 [27] and CO_2 [28] and those for gas separation,[29] liquid-phase adsorption,[30] catalytic processes,[31] drug delivery systems [32] and other. The applications of MOFs are considered in reviews;[24, 33] a review is devoted to the use of MOFs in non-linear optics.[34]

The first patent on the commercial use of MOF-based materials was granted in 1996 to Nalco Chemical Company, and in 2013–2016, the MOF Technologies and Numat Technologies companies started the industrial manufacture of these materials. The review of Rubio-Martinez *et al.*[35] gives data from the catalogues of some companies producing MOFs (Table 2).

An interesting system called ION-X was developed by the NuMat company for the delivery of dopant gases (AsH_3, PH_3, BF_3) in the adsorbed state in the MOF pores below atmospheric pressure. The gases are delivered in containers filled with MOF granules (the composition is not disclosed).[40] The ION-X systems have already been certified and are used in electronic industry.

Metal-organic frameworks obtained in laboratory and in industry are crystalline powders with crystallite sizes ranging from several nanometres to hundreds of micrometres. However, the use of polycrystalline powders in the separation- or purification-related processes often leads to a considerable pressure drop as a gas or a liquid passes through the adsorbent layer. Dusting, attrition, weight loss and difficulty of transportation and processing of these powders also deserve mention.

Lately, researchers have paid particular attention to the development of composites based on MOFs and carbon materials (active carbons,[41] graphene,[42] carbon aerogels [43]), polymers (polylactic acid [44]), nano-sized metal particles [9, 45, 46] or metal oxide particles,[46] semiconducting colloidal quantum dots [47, 48] and so on. The preparation methods and applications of MOF-based composites have been analyzed in detail in reviews.[49, 50]

It is noteworthy that the formation of beads, spheres and films [50] was proposed to enhance the performance of MOF-based composites. Several procedures were developed to grow MOF crystals directly during the synthesis in the silica pores.[51, 52] Other procedures imply the introduction of MOF into a substrate of a definite shape during composite shaping. For example, monolithic composites were fabricated using liquid-phase epitaxy: the pores of a mesoporous silica monolith were filled with nanoparticles of the HKUST-1 metal-organic framework (see Table 2).[52]

It is evident that the synergistic combination of MOFs (regular porosity, high crystallinity) and functional materials with unique magnetic, optical and catalytic properties implemented in composite materials considerably extends their scope of applicability, including adsorption storage and transportation of methane. Quite a few recent publica-

Table 2. Commercially manufactured metal-organic frameworks (as per 2016 according to Rubio-Martinez *et al.*[35] and as per February, 2019, according to the websites of manufacturers [36 – 40]).

Designation	Formula	Brand name	Manufacturer	Potential applications	Ref.
Al(OH)-Fumarate	$[Al(OH)(O_2CCH{=}CHCO_2)]$	Porolite Al, Basolite® A520	MOF Technologies, BASF	Catalysis, drying and water collection techniques; natural gas desulfurization; storage and separation of gases (H_2, CH_4) and volatile organic compounds; energy recuperation and utilization	36, 37
HKUST-1, Cu-BTC, MOF-199	$Cu_3(BTC)_2$ ($C_{18}H_6Cu_3O_{12}$)	Basolite® C300, Porolite C1, CuBTC	BASF, MOF Technologies, STREM Chemicals, KRICT, Inven2, Framergy, American Elements	Natural gas adsorption and purification; storage and separation of gases (H_2, N_2, CO_2)	37, 38
Fe-BTC	$C_9H_3FeO_6$	Basolite® F300,	BASF, MOF Technologies	Catalytic capture of volatile organic compounds; dye removal from waste water	36, 37
PCN-250-Fe_3, MIL-127	$C_{48}H_{20}N_6O_{32}Fe_3$	Porolite F3, AYRSORB® F250, CONEKTIC F250	MOF Technologies, Framergle, STREM, American Elements	ANG technology; industrial waste treatment; natural gas desulfurization; storage and separation of gases (H_2, CO_2, H_2S) and volatile organic compounds	36, 38
MOF-74, M-CPO-27	$M_2C_8H_2O_{60}$ (M = Mg, Co, Ni, Cu)	Porolite M7, Porolite D7, Porolite N7, Porolite C7	MOF Technologies	Carbon dioxide capture and storage; anaesthetic gas supply systems; natural gas desulfurization; storage and separation of gases (H_2, CO_2, NO_x); industrial wastewater treatment	36
MIL-100(Fe)	$C_{18}H_8Fe_3O_{16}$	KRICT F100	KRICT	Storage and separation of gases; catalysis; drug delivery; magnetic and optical devices	39
MIL-53(Al)	$C_8H_2AlO_5$	Basolite® A100	BASF	Separation of alkylaromatic hydrocarbons; hydrogen adsorption	39
MOF-177	$C_{54}H_{30}O_{13}Zn_4$	Basolite® Z377	BASF	Adsorption of gases (H_2, CO_2, N_2) and volatile organic compounds	37
Zr-MOF	$Zr_6O_4(OH)_4(BDC)_6$	UiO-66	Inven2, MOF Apps, ProfMOF	Adsorption processes involving CO_2	39
ZIF-8	$C_8H_{10}N_4Zn$	Basolite® Z1200, Porolite Z8, ZIF-8	BASF, MOF Technologies, MOF Apps, STREM Chemicals	Storage and separation of gases (H_2, CO_2, N_2, CH_4) and volatile organic compounds; natural gas desulfurization	36, 37
ZIF-67	$C_8H_{10}N_4Co$	ZIF-67, Porolite D6	American Elements, MOF Technologies	ANG technology; industrial wastewater treatment; natural gas desulfurization; storage and separation of gases (H_2, CO_2) and volatile organic compounds	36
Zn-SIFSIX-pyrazine	$[Zn(C_4H_4N_2)_2SiF_6]_n$	Porolite Z6	MOF Technologies	Carbon capture and storage; natural gas desulfurization; storage and separation of gases (H_2, CO_2, N_2, CH_4)	36

Note. The following designations are used: BTC is benzene-1,3,5-tricarboxylate; CPO are coordination polymers manufactured at the University of Oslo (coordination polymers of Oslo); HKUST-1 is a metal-organic framework manufactured at the Hong Kong University of Science and Technology; MIL is a metal-organic framework obtained at the Institute Lavoisier (materials of Institute Lavoisier); MOF is a metal-organic framework; PCN is a porous coordination network; ZIF is a zeolitic imidazolate framework.

tions have been devoted to the use of MOFs and composites based on them as adsorbents for methane storage.[20–26, 53, 54]

The purpose of this review is to analyze the results on the targeted synthesis of MOFs, the porous structure and adsorption properties of which are optimal for the adsorption storage of methane. Classification of the existing MOFs is given and the methods for their preparation, their morphology and porous structure, and their adsorption properties towards methane are discussed. It seemed important to us to consider the methods for preparation of adsorption materials (MOFs in the pure state and composites based on them) of the optimal shape to be used for the adsorption storage and transportation of natural gas.

2. Microporous metal-organic frameworks

2.1. General characteristics of metal-organic frameworks

The end of the 20th century witnessed vigorous progress in the research dealing with the synthesis of a new subclass of coordination compounds, that is, metal-organic frameworks, which consist of metal ions or clusters coordinated and linked by organic ligands (linkers).[55] It is noteworthy that MOFs do not refer to the class of coordination compounds formed by bonds between carbon and metal atoms.[55, 56] According to the IUPAC terminology (2013), a metal-organic framework (MOF) is a coordination network with organic ligands containing potential voids (pores).[57]

Due to the similarity of some textural and adsorption characteristics (such as three-dimensional framework, high crystallinity and porosity) of MOFs and zeolites, the former are called zeolitic materials.[58]

While summarizing the data on MOFs, Yaghi and coworkers[59–61] developed a concept based on the network topology. According to this concept, organic ligands and metal ions are considered as secondary building units (SBU) that form the MOF. It is noteworthy that the notion of secondary building units is accepted in the chemistry of zeolite and refers to SiO_4 or AlO_4.[62] Secondary building units of MOFs are represented as simple geometric figures corresponding to the geometry of inorganic clusters or coordination spheres of doubly, triply or, more rarely, quadruply charged metal cations (Cu^{2+}, Ni^{2+}, Zn^{2+}, Mn^{2+}, Fe^{2+}, Co^{2+}, Cr^{3+}, Al^{3+}, Fe^{3+}, Zr^{4+}, Hf^{4+}, Ti^{4+}, Sc^{4+}), which are connected by organic groups to form a framework.[58, 60, 61]

Most often, bi-, tri- or tetradentate organic ligands are aromatic carboxylic acids or heterocycles. Examples of organic ligands used for the synthesis of MOFs are presented in Table 3. The abbreviated designations of ligands mentioned below, but not included in the Table are expanded in the text. Note benzene-1,4-dicarboxylic (terephthalic) acid and its substituted derivatives, which provide steric rigidity and diverse coordination modes.

Apart from mono- and dicarboxylate bridging ligands, sterically rigid, highly polarized aromatic ligands with three or four carboxylate groups (*e.g.*, H_3BTC, see Table 3) are used rather frequently; this gives rise to MOFs with more complex topology and more rigid frameworks.

Figure 1 shows the scheme of MOF formation as a crystal lattice (on the right) in which the nodes occupied by inorganic clusters or ions (at the centre) are linked by bridging organic ligands, BDC (on the left).

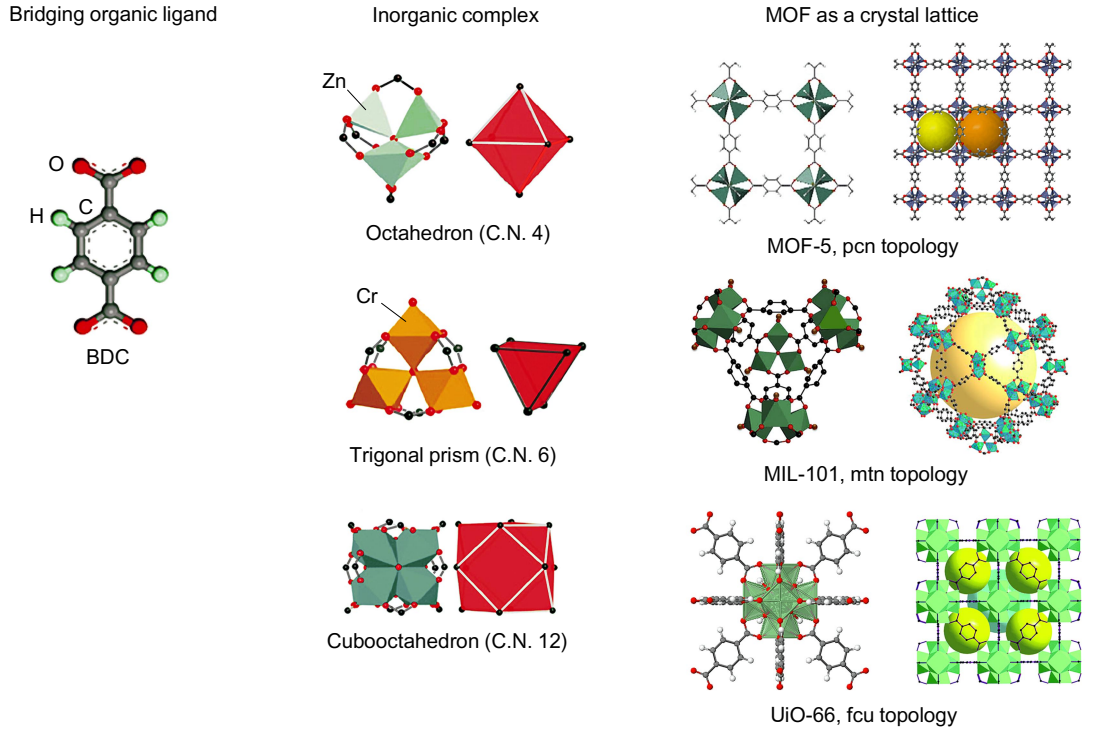


Figure 1. Scheme of formation of MOFs from terephthalic acid (H_2BDC) as the source of an organic linker (BDC) and metal clusters (Zn, Cr, Zr).
The polyhedra show the metal atom coordination in secondary building units: the geometry of oxygen atom environment is shown on the right and the geometry of core clusters determined by carbon atom positions is on the left. The coordination numbers correspond to the number of linkers coordinated to each metal cluster[24, 62–65] and spheres correspond to free volumes inside the cages of MOF-5, MIL-101 and UiO-66. The types of topology are given in Refs 66–69.

Table 3. Most popular ligand sources and MOFs based on them.

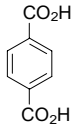
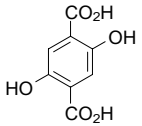
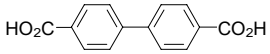
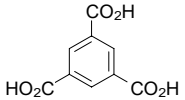
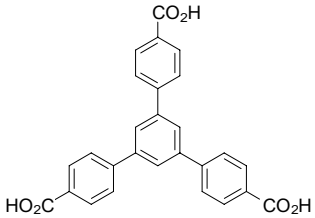
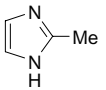
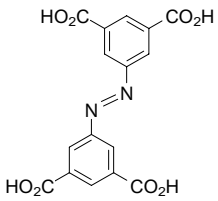
Ligand name	Ligand source		Metal-organic framework	
	designation	structural formula	accepted designation	formula
Benzene-1,4-dicarboxylate (BDC)	H_2BDC		MOF-5 MIL-53(Al) UiO-66 MIL-101	$Zn_4O(BDC)_3$ $Al(OH)(BDC)$ $Zr_6O_4(OH)_4(BDC)_6$, $Cr_3O(H_2O)_2F(BDC)_3$
Dihydroxyterephthalate (DOT)	H_2DOT		M-MOF-74 (M-CPO-27)	M_2DOT (M = Ni, Co, Mg)
Biphenyl-4,4′-dicarboxylate (BPDC)	H_2BPDC		IRMOF-10 UiO-67	$Zn_4O(BPDC)$ $Zr_6O_6(BPDC)_6$
Benzene-1,3,5-tricarboxylate (BTC)	H_3BTC		HKUST-1 or MOF-199	Cu_3BTC
4,4′,4″-(Benzene-1,3,5-triyl)tribenzoate (BTB)	H_3BTB		MOF-177	$Zn_4O(BTB)_2$
2-Methylimidazol-1-ide (MIm)	MIm		ZIF-8	$Zn(MIm)_2$
Azobenzene-3,3′,5,5′-tetracarboxylate (ABTC)	H_4ABTC		PCN-250-Fe_3	$Fe_3O(ABTC)$

Table 3 (continued).

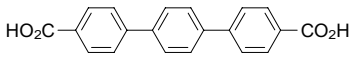
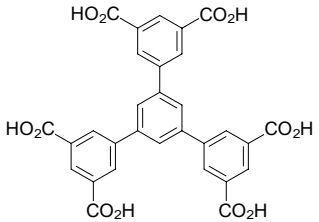
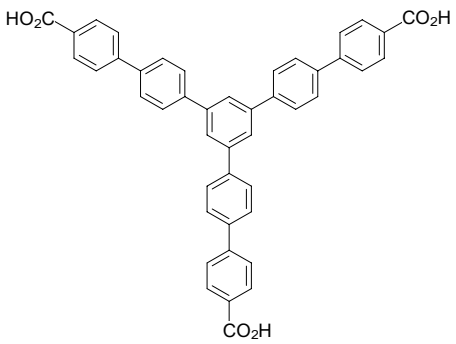
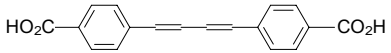
Ligand name	Ligand source		Metal-organic framework	
	designation	structural formula	accepted designation	formula
p-Terphenyl-4,4″-dicarboxylate (TPDC)	H_2TPDC		IRMOF-16	$Zn_4(\mu_4\text{-}O)(TPDC)_3$
3,3′,3″,5,5′,5″-(benzene-1,3,5-triyl)hexabenzoate (BHB)	H_6BHB		UTSA-20	Cu_3BHB
4,4′,4″-[Benzene-1,3,5-triyl-tris(1,1′-biphenyl)-4′-carboxylate] (BBC)	H_3BBC		DUT-60	$Zn_4O(BCPBD)(BBC)_{4/3}$
4,4′-(Buta-1,3-diene-1,4-diyl)dibenzoate (BCPBD)	H_2BCPBD		DUT-60	$Zn_4O(BCPBD)(BBC)_{4/3}$

Table 3 (continued).

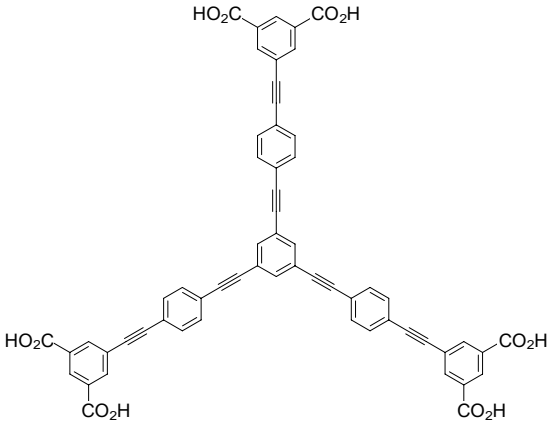
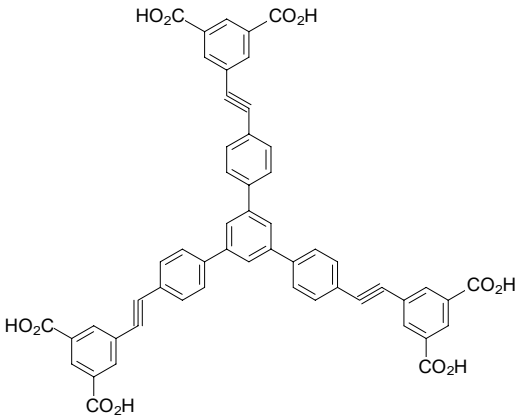
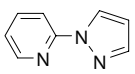
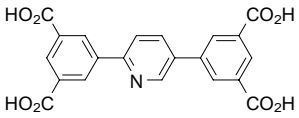
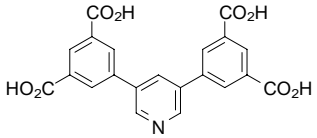
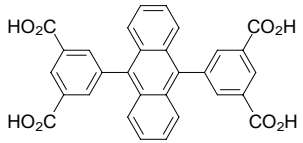
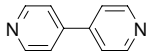
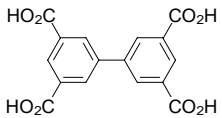
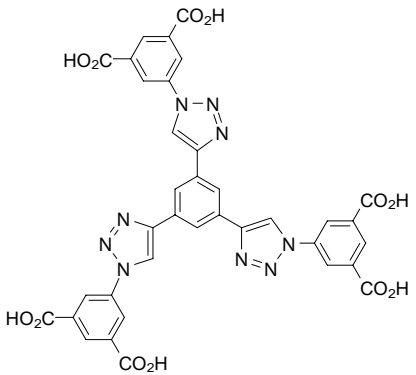
Ligand name	Ligand source		Metal-organic framework	
	designation	structural formula	accepted designation	formula
1,3,5-tris[(1,3-carboxylate-5-(4-(ethynyl)phenyl))butadiynyl]-benzene (TCEPBB)	H_3TCEPBB		NU-111	Cu_3(TCEPBB)
5,5′,5″-[Benzene-1,3,5-triyl-tris(benzene-1,4-diylethyne-1,2-diyl)]triisophthalate (PTEI)	H_6PTEI		NOTT-116 (PCN-68)	$Cu_3(C_{54}H_{24}O_{12})(H_2O)_3$ Cu_2(PTEI)
2-(1*H*-Pyrazol-2-yl)pyridine (PYPZ)	HPYPZ		MAF-38	$Zn_3(PYPZ)_3(BTC)$
5,5′-Pyridine-2,5-diyl)diisophthalate (PDDI)	H_4PDDI		ZJU-5	$[Cu_2(PDDI)(H_2O)_2](DMF)_4(H_2O)_6$

Table 3 (continued).

Ligand name	Ligand source		Metal-organic framework	
	designation	structural formula	accepted designation	formula
3,5-bis(3,5-dicarboxylatophenyl)pyridine (BDPP)	H_4BDPP		NJU-Bai10	$Cu_6(BDPP)_3(H_2O)_6$
5,5′-(Anthracene-9,10-diyl)diisophthalate (ADIP)	H_4ADIP		PCN-14	$Cu_2(H_2O)_2(ADIP)$
1,4-Diazabicyclo[2.2.2]octane (DABCO)	DABCO		–	$Zn_2(BDC)_2(DABCO)$
4,4′- Bipyridine (BPY)	H_2BPY		–	$Co_2(4,4'\text{-}BPY)_3(NO_3)_4$
1,1′-(Biphenyl-3,3′,5,5′)tetracarboxylate (BPTC)	H_4BPTC		MOF-505	$Cu_2(BPTC)(H_2O)_2(DMF)_3(H_2O)$
5,5′,5″-[Benzene-1,3,5-triyl-tris(1*H*-1,2,3-triazole-4,1-diyl)]triisophthalate (BTTI)	H_6BTTI		NOTT-122	$[Cu_3(BTTI)(H_2O)_3]\cdot$ $\cdot 10\,(DMF)\cdot 10\,H_2O$

Note. The following designations are used: DUT are MOFs synthesized at the Dresden University of Technology; MAF metal azolate frameworks based on pyridine-2-carboxylic acid; NOTT are isoreticular MOFs synthesized at the University of Nottingham; NJU-Bai are isoreticular MOFs synthesized at the Nanjing University by Bai's group; UTSA are MOFs synthesized at the University of Texas at San Antonio; ZJU are isoreticular MOFs synthesized at the Zhejiang University.

It is clear that the SBUs dictate the geometry of the synthesized MOF. In addition, in each geometry, the replacement of the central metal atom is possible, which further increases the number of MOFs with diverse geometric configurations differing in functional properties.

In turn, the SBUs can be combined into a framework *via* organic ligands. The ligand can be chosen in two ways:

— with retention of the initial framework geometry, but changing unit cell parameters of the MOF crystal upon elongation of the ligand carbon chain;[24,64] this gives so-called isoreticular structures with the same topology and formula of the inorganic cluster (Fig. 2);

— with a change in the relative positions of the functional groups in the ligand and changing framework geometry (Fig. 3).

Analysis of MOF topologies resulted in compilation of the MOF database,[69,72] which formed the basis for rational design of MOFs. It is evident that by using the numerous types of organic ligands and crystal structure topologies contained in the Reticular Chemistry Structure Resource database,[68] one can gain a multitude of topology–SBU combinations, which form the so-called space of hypothetical MOFs with unique properties.[69,72] This knowledge underlies the synthesis of isoreticular MOFs of a specified composition from definite building units. In the last decade, several tens of thousands of structures were generated in this way: 69 666 of MOFs were present in the Cambridge Crystallographic Data Centre by 2017 (http://www.ccdc.cam.ac.uk/products/csd/).[73]

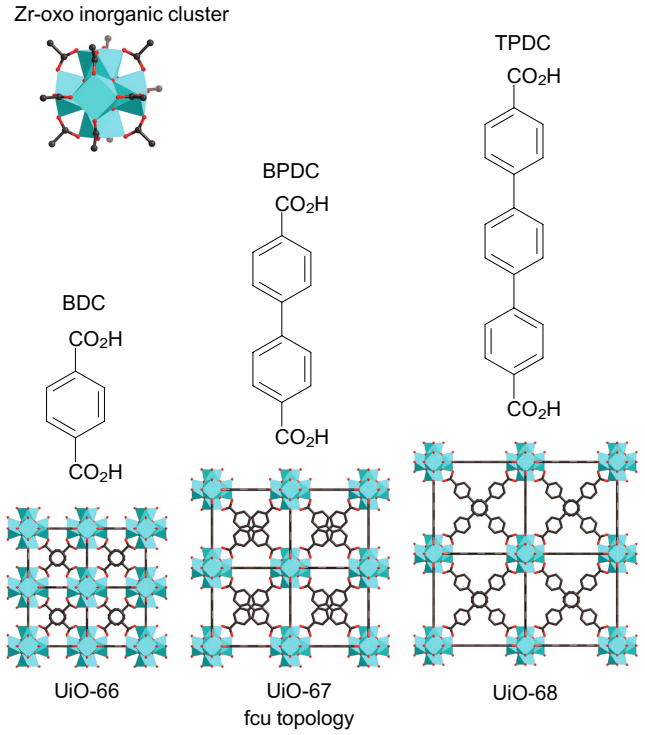


Figure 2. Scheme illustrating retention of the initial MOF symmetry after elongation of the carbon chain of the linker considered in relation to the UiO-66 series.[65] The sources of ligand (linker) are terephthalic acid (H_2BDC) in UiO-66, biphenyl-4,4′-dicarboxylic acid (H_2BPDC) in UiO-67 and *p*-terphenyl-4,4′-dicarboxylic acid (H_2TPDC) in UiO-68.[66]

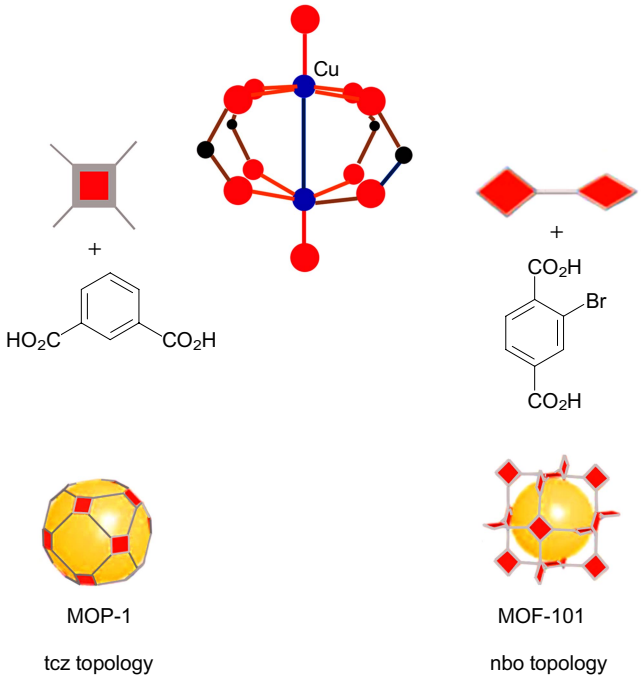


Figure 3. Types of MOF geometry resulting from the change of relative positions of substituents in the linker molecule.[24] In the ball-and-stick model of the $Cu_2(CO_2)_4$ secondary building unit, the first coordination sphere of copper is composed of oxygen atoms and the second one is formed by carbon atoms. MOP-1 (MOP is a metal-organic polyhedron), $Cu_{24}(m\text{-BDC})_{24}(DMF)_{14}\cdot(H_2O)_{10}$, DMF is dimethylformamide;[70] MOF-101, $Cu_2[o\text{-Br(BDC)}]_2(H_2O)_2$.[71] The yellow spheres correspond to free space within the MOF cage. The Figure is reproduced from the data of Refs 60, 61, 64 and 67–71.

It should be emphasized that the interest in MOFs is caused by the possibility to control the relationship between their hybrid structure and the combination of properties inherent in organic and inorganic components and, hence, to obtain materials with specified physicochemical properties.[67]

2.2. Porous structure of metal-organic frameworks

The above definition of MOFs[57] and the principle of formation of 2D or 3D frameworks by means of rigid organic linkers, which ensure strong interaction with metal cations or clusters, imply the presence of porosity. The extensive porous structure is one of the most important properties of MOFs, which determines their potential applications, in particular, for gas storage and separation. MOFs are characterized by the term ‘permanent porosity’, which means that the framework is retained after the vacuum thermal treatment, which is used to remove guest molecules of the solvent used for the synthesis from the pores (Fig. 4).

According to the IUPAC rules, depending on the pore size, porous materials are subdivided into three classes:[75] microporous (effective linear size of pores $X_0 < 2$ nm); mesoporous ($2 < X_0 < 50$ nm); and macroporous ($50\text{ nm} < X_0$). The syntheses of MOFs usually give micro- and mesoporous compounds.

Parameters of the MOF porosity determined by measuring sorption of gases were published for the first time in 1998.[76] The study was carried out for the MOF-2 frame-

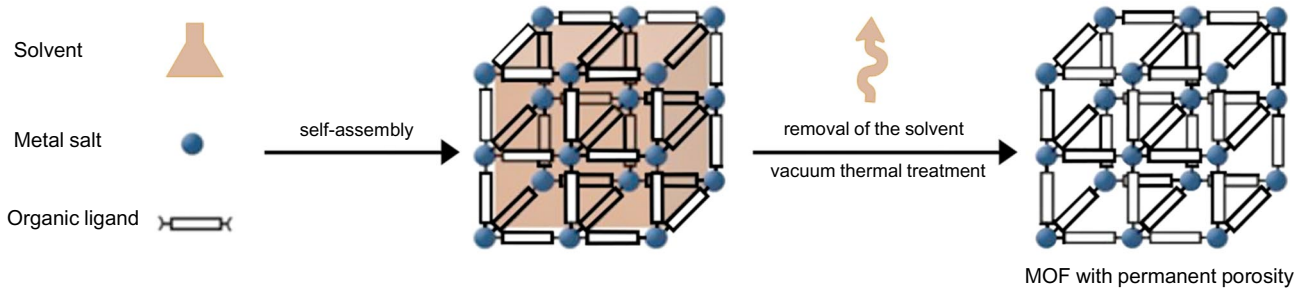


Figure 4. Scheme of formation of permanent porosity of MOFs during the synthesis, including the removal of guest solvent molecules from the framework. The Figure is based on Ref. 74.

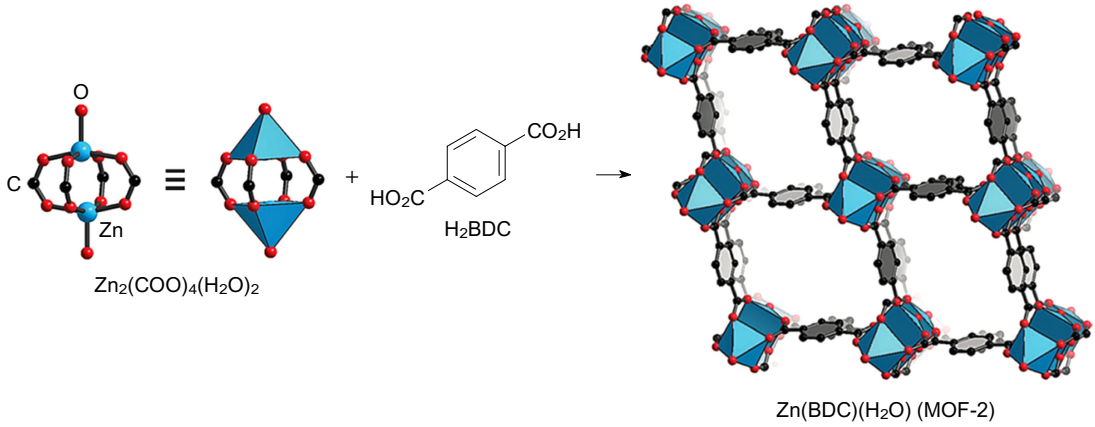


Figure 5. Scheme of formation of MOF-2 framework with channels with rectangular cross-sections (view along the [001] crystallographic axis). The hydrogen atoms are omitted. The Figure is adapted from Ref. 76.

work [Zn(BDC)(H_2O)] formed by paddle-wheel-shaped $Zn_2(COO)_4(H_2O)_2$ building units connected by BDC ligands (Fig. 5).

The two-dimensional lattices are connected to one another by strong hydrogen bonds between water molecules and carboxylate groups of the organic ligand. It was shown that the framework of MOF-2 has voids filled by water and dimethylformamide guest molecules. The vacuum thermal treatment of the product of synthesis afforded the desolvated Zn(BDC) structure. Measurements of the adsorption of nitrogen vapour at 77 K and CO_2 vapour at 195 K revealed permanent porosity. The specific surface area (270 to 310 $m^2\ g^{-1}$) and the pore volume (0.094 to 0.086 $cm^3\ g^{-1}$) were determined; the averaged pore size was 0.42 nm.[76]

Further development of synthetic routes to MOFs gave three-dimensional MOF-3 [$Zn_3(BDC)_3$)] and MOF-4 [$Zn_2(BTC)(NO_3)$)],[76,77] which were also shown to have permanent porosity. Among the MOF series, the structure MOF-5 proved to be most advantageous (Fig. 6*a*). The tetrahedral $[Zn_4O]^{6+}$ building units are connected by dicarboxylate ligands. The MOF-5 framework can be described as a regular cubic lattice. As follows from Fig. 6*b*, adsorption isotherms refer to type I (Ref. 80) or Ia,[81] which directly indicates that the MOF-5 structure is microporous. The specific surface area (2900 $m^2\ g^{-1}$) and pore volume (1.04 $cm^3\ g^{-1}$) substantially exceed these parameters for other micro- and mesoporous adsorbents such as activated carbons, zeolites and silicas.

The so-called tuning of MOF porosity, that is, a change in the inner size of framework voids depending on the type of the organic ligand was demonstrated in relation to MOF-5 (Fig. 7). A series of isoreticular three-dimensional metal-organic frameworks, IRMOF-*n*, has been developed, where IRMOF-1 corresponds to MOF-5. Figure 7 depicts only IRMOF-*n* synthesized using carboxylate ligands without functional groups. According to X-ray diffraction and elemental microanalysis data,[82] the introduction of functional groups does not change the IRMOF-*n* network structure. It can be seen that an elongation of the organic ligand leads to increasing pore size in MOFs, that is, increases the maximum diameter of the imaginary sphere that can be inscribed into the greatest pores (fixed diameter, D_{fix}) and the maximum diameter of the sphere that can pass through the smallest pores (free diameter, D_{free}). The D_{fix} and D_{free} values are estimated taking into account the van der Waals radii of the atoms that form the MOF.

A similar change in the porosity resulting from a change in the ligand chain length was demonstrated above for the series UiO-66 (see Fig. 2):[65,66] on going from UiO-66 to UiO-67 and UiO-68, the D_{fix} and D_{free} values vary in the following way:

MOF	UiO-66	UiO-67	UiO-68
D_{fix} /nm	1.1	1.6	1.7
D_{free} /nm	0.8	1.2	1.3

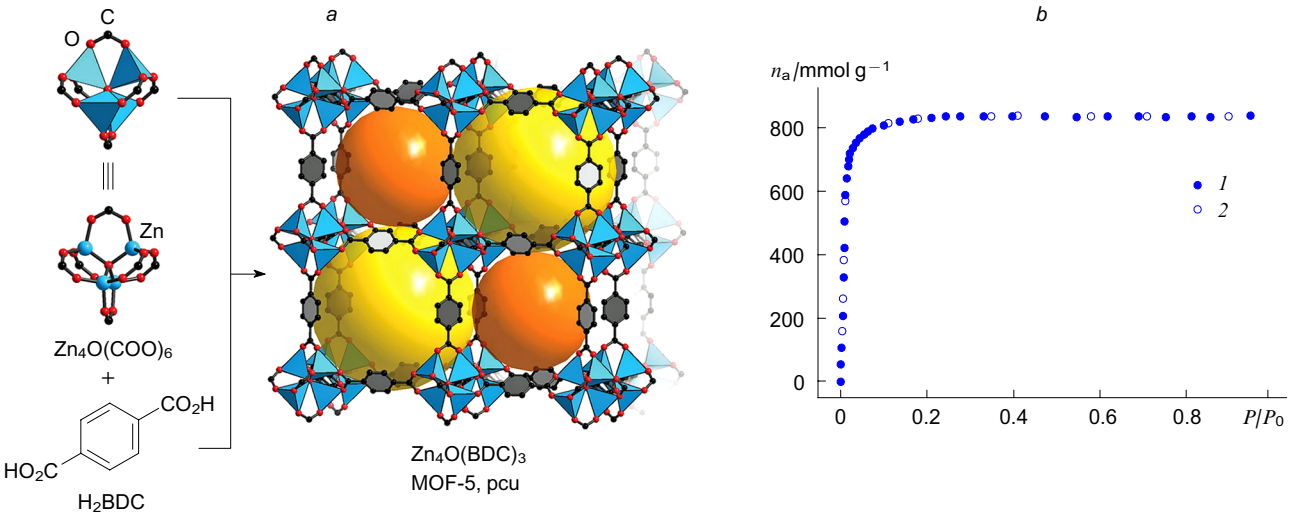


Figure 6. Scheme illustrating the composition of the crystal of MOF-5 (*a*)[78] and total adsorption (n_a) isotherms during adsorption (*1*) and desorption (*2*) of nitrogen vapour at 77 K in the pores of this MOF (*b*).[79]
The crystal is formed by the $Zn_4O(COO)_6$ building units connected by BDC into a cubic framework; the yellow and orange spheres 1.51 and 1.10 nm in diameter correspond to free spaces within the cubic cage. The hydrogen atoms are omitted; pcu is the primitive cubic unit cell topology.[68]

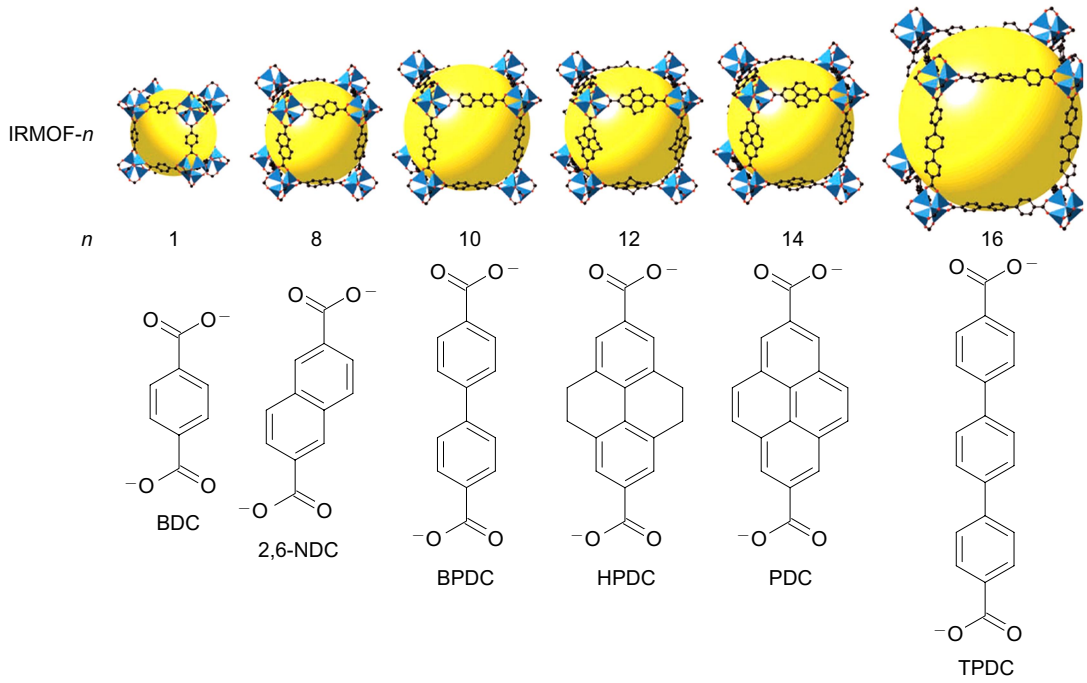


Figure 7. Change in the framework porosity depending on the type of organic ligands in the IRMOF-*n* series.
The yellow colour indicates spheres with the fixed diameter (D_{fix}) which can be inscribed into the greatest pore. The free diameters (D_{free}) for spheres that can pass through the smallest pores in the MOF are given. The hydrogen atoms are omitted. The Figure is based on the data of Ref. 82.

Thus, depending on the size of organic ligands (linkers) connecting the inorganic blocks, the porous 3D lattice structures, IRMOF-*n*, are formed, with pore size varying from 0.1 to 2.9 nm. The fraction of the free volume in the IRMOF-*n* crystals varies from 55.8% (IRMOF-5) to 91.1% (IRMOF-16), which exceeds the fraction of free space in open-structure zeolites (45% – 50%) (see Ref. 15 in Ref. 82) and is comparable with the corresponding value for non-crystalline porous structures such as xerogels or aerogels.[82] It was shown that IRMOF-6 (with the 1,2-benzocyclobu-

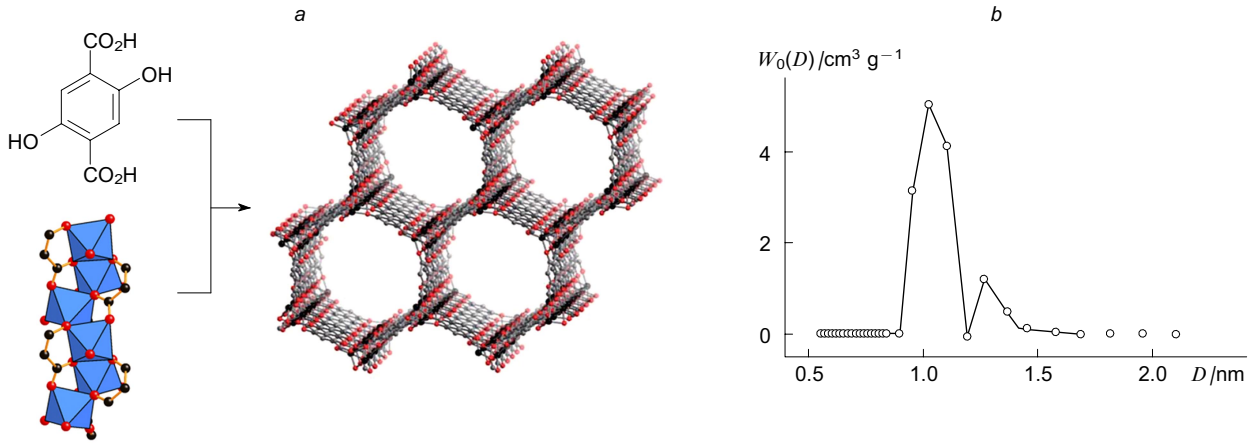


Figure 8. Crystal structure of M-MOF-74 (M = Zn, Mn, Ni, Co) (*a*) and pore size (D) distribution of the pore volume (W_0) in Ni-MOF-74 found from the nitrogen adsorption isotherms.[83]) (*b*). The Figure is adapted from Refs 69, 84 and 85.

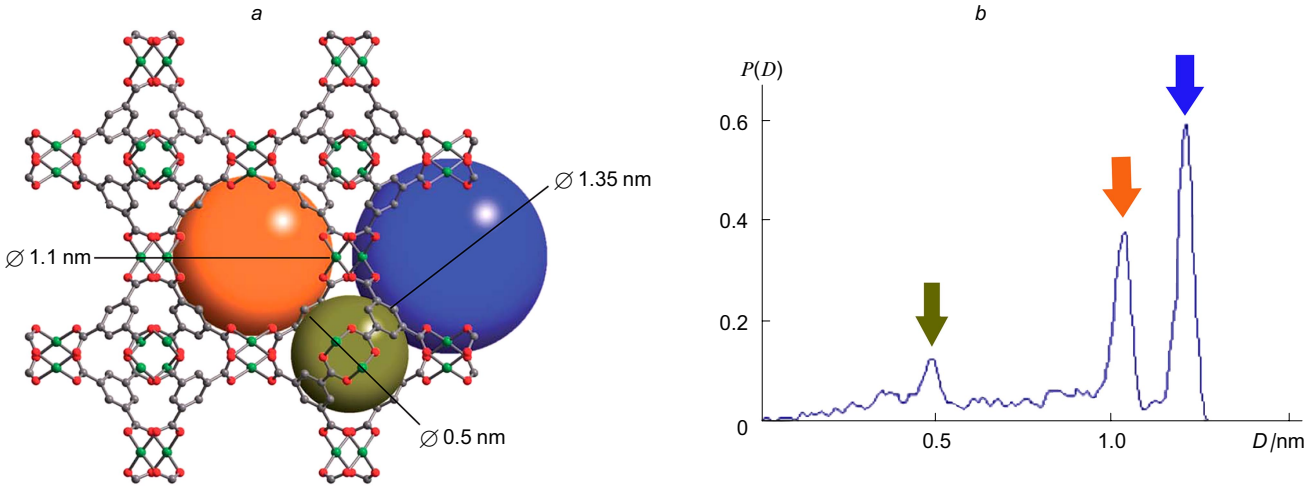


Figure 9. Crystal structure of HKUST-1 with three types of pores designated by differently coloured spheres (*a*), which was used to calculate the dimensionless pore size distribution function [$P(D)$] (*b*). The Figure is adapted from Refs 85 and 86.

tene-3,6-dicarboxylate ligand) demonstrates a high adsorption capacity towards methane:† 240 cm^3(STP) g^{-1} [or 150 m^3(STP) m^{-3}], which proved to be higher than the data for 5A zeolite (see Ref. 17 in Ref. 82).

Eddaoudi *et al.*[82] discovered interpenetration of the frameworks for some IRMOF-*n* (with the BPDC, HPDC, PDC and TPDC ligands), which changes the porous space (the free volume is ~76%). However, by reducing the reactant concentrations, it is possible to obtain non-interpenetrating frameworks, with the free volume increasing up to 81%–91% (IRMOF-16); simultaneously, the crystal density decreases to 0.21 $g\,cm^{-3}$.

Note that the key difference of MOFs from traditional porous materials, such as, molecular sieves or activated carbons, is that the pores are not separated by walls. The regular porosity of MOFs (50% to 90%)[67] is formed by connected open and evenly distributed channels and voids. It should be emphasized that the principle of MOF assembly from secondary building units with a particular geometry specified by the coordination sphere of the metal cation and organic ligands of a definite length allows the prediction of a regular system of pores, pore shape and pore size distribution (Fig. 8). For example, the porous structure of M-MOF-74 (or M-CPO-27, where M = Zn, Mn, Ni, Co, Cu) is a set of 1D channles (see Fig. 8 *a*) and, as follows from nitrogen adsorption data,[83] it is described by a narrow pore size distribution with a maximum at ~1.1 nm, which is in line with calculation results (see Fig. 8 *b*).[84] Meanwhile, in the HKUST framework, the paddle-wheel-shaped $Cu_3(BTC)_2$ secondary building unit [69] forms a more intricate porous structure with three types of pores with characteristic sizes (Fig. 9).[85, 86]

Moreover, the considered principle of MOF assembly enables the manufacture of porous materials with record-high specific surface areas and pore volumes. Indeed, a paper of a research group from Dresden University of Technology published in 2018 [87] describes the synthesis of DUT-60 with the maximum currently known Brunauer–

† The methane volume refers to the standard thermodynamic conditions for gases (standard temperature and pressure, STP): T = 273.15 K, P = 101 325 Pa. The normal temperature and pressure (NTP) for gas volume according to GOST 2939-63 or according to NIST are T = 293.15 K, P = 101 325 Pa.

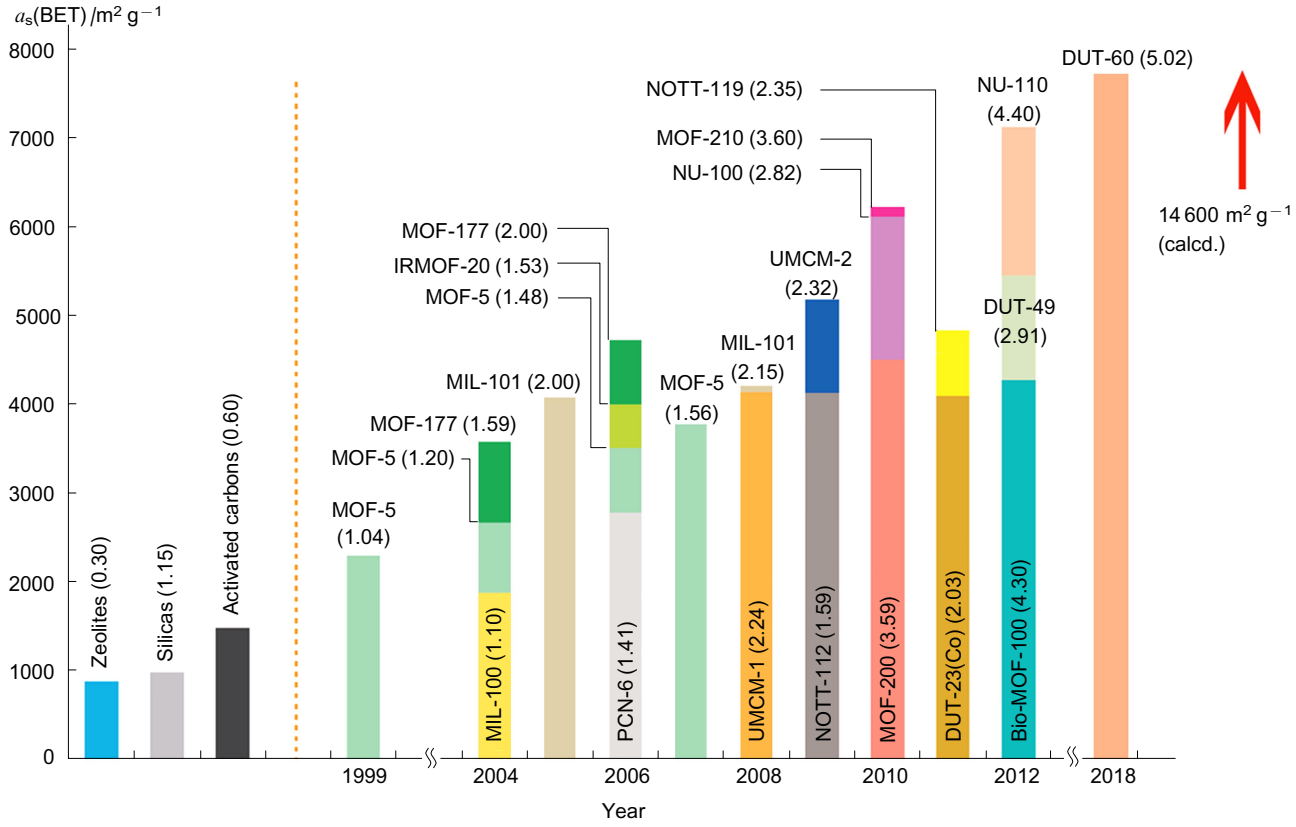


Figure 10. Diagram of variation of the porosity of MOFs synthesized in different years in comparison with conventional porous materials. The values in parentheses are the specific pore volumes in cm^3 g^{-1} (Ref. 69). The diagram is based on the data of Refs 82, 87, 89.

Emmett–Teller (BET) specific surface area determined from a nitrogen adsorption isotherm at 77 K, a_s(BET) = 7839 m^2 g^{-1}.[88] This exceeds the value attained by 2012 for the NU-110 framework, $Zn_4O(BTE)_{4/3}(BPDC)$, which amounted to 7140 m^2 g^{-1} (Fig. 10).[69] Hönicke *et al.*[87] emphasized the repeatability of nitrogen adsorption measurements and the resistance of DUT-60 they synthesized to mechanical load. The crystal topology was confirmed by X-ray diffraction data, the crystal density was 0.187 g cm^{-3} and the porosity was 90.3%. The pore volume was an order of magnitude greater than those of zeolites, silicas and active carbons.[69,87] Also, according to the data of theoretical calculations,[89] the specific surface area of the MOF can reach 14 600 m^2 g^{-1}!

Certainly, an important problem is stability of this type of MOFs. Reviews[66,90,91] give examples of MOFs stable against moisture and heating (up to 400–450 °C). Such MOFs include, in particular, MOF-177 and MIL-101(Cr) with specific surface areas of 5640 (Ref. 90, 91) and 4100 m^2 g^{-1} (Ref. 66).

It should be noted that for most microporous MOFs, high BET specific surface areas[88] are conventional values. Indeed, adsorption in the microporous adsorbents does not imply successive formation of adsorption layers on the micropore surface; instead, the process occurs *via* filling of the adsorption space according to the mechanism described in Dubinin's theory of volume filling of micropores.[92] Therefore, for microporous adsorbents, the notion of surface loses its physical meaning. However, virtually all experimental works dealing with the structure of microporous adsorbents present a_s(BET) values, for example, when comparing MOF- and carbon-based adsorbents.[93] It is commonly believed that a_s(BET) for microporous adsorbents corresponds to some conventional surface and is a characteristic parameter used to compare these adsorbents.[81]

Considering the foregoing, it is natural to assume that the extensive system of MOF pores largely determines their adsorption properties, in particular:

— the presence of voids and channels forming a regular space of micro- and, in some MOFs, also mesopores;

— high controllable adsorption capacity;

— the possibility of formation of active adsorption sites of various strength;

— special electronic properties.

Therefore, MOFs can be considered as potential materials for gas storage, in particular, methane storage.[23,94,95]

2.3. Methods for the preparation of metal-organic frameworks

According to the results of numerous studies, the degree of crystallinity, phase purity and textural properties (specific surface area, porosity) of MOFs, *i.e.*, characteristics that determine the adsorption capacity and stability to chemical, mechanical and thermal impacts, significantly depend on the preparation process, including synthesis, activation and functionalization (Fig. 11).

The methods for the synthesis of MOFs are analyzed in detail in a number of reviews.[24,90,94–97] Mention should be

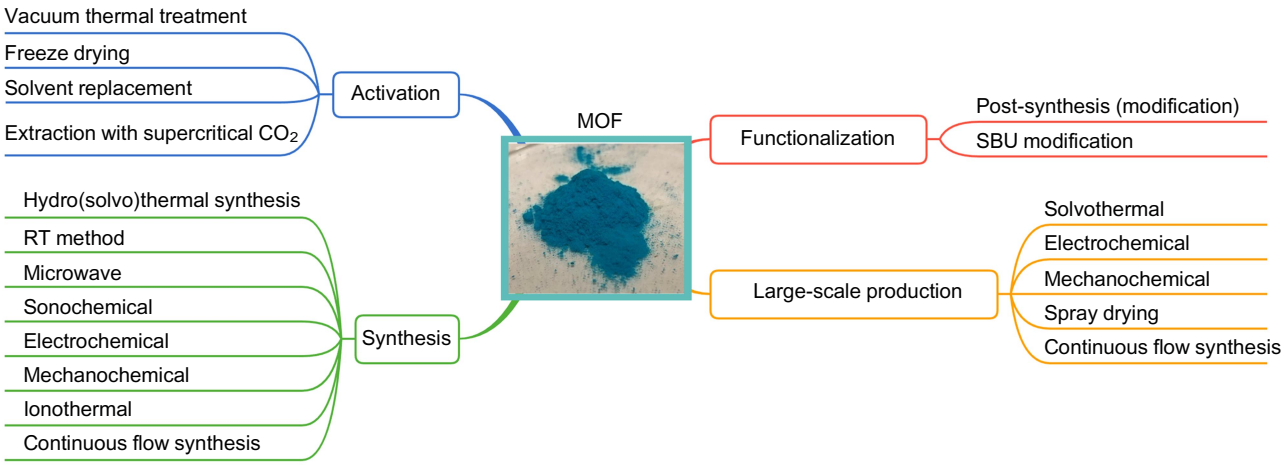


Figure 11. Stages of MOF preparation determining their properties and functions. The Figure is based on Refs 24, 35, 90, 94–96.

made of the review by Rubio-Martinez *et al.*,[35] who not only compare the methods for MOF synthesis, but also discuss the feasibility of their industrial implementation. The techno-economic analysis performed by DeSantis *et al.*[98] includes evaluation of MOF synthesis from the standpoint of engineering complexity, cost of expendable materials and the product yield.

The hydro(solvo)thermal synthesis was successfully accomplished for the first time in 1995 to give $[Cu(4,4'\text{-BPY})_{1.5}]NO_3(H_2O)_{1.25}$.[99] Subsequently, the slow diffusion process was proposed (MOF-2),[78,100] which can give large MOF crystals, but lasts for 1–2 weeks and, therefore, it is considered to be less efficient.

A standard procedure for the preparation of MOFs based on mixing solutions of a metal salt and an organic ligand in water or in an organic solvent (DMF, ethyl alcohol, pyridine, *etc.*) is reflected in Fig. 12.[99–114] In some cases, triethylamine is used to accelerate the reaction without changing the structure of the final product.[101] The organic solvent and/or water act as structuring reagents. Then the reaction mixture is subjected to an external impact inducing the self-assembly of the MOF.

In the hydro(solvo)thermal synthesis, this impact includes heating of the reaction mixture to a temperature equal to or higher than the solvent boiling point.[99–106] The reaction mixture can be exposed to microwave radiation at 120 to 210 W (microwave method[107–111]), which causes local heating. This increases the rate of formation of crystallization centres and, hence, accelerates the growth of MOF crystals. The sonochemical method[112–114] employs ultrasonic treatment, which induces acoustic cavitation. As a result, bubble formation and collapse and the temperature and pressure gradients increase the surface area of the contact between reactants and give rise to active sites with dangling bonds. Consequently, the formation of MOF nanocrystals is considerably accelerated. After completion of the reaction induced by any type of treatment, the precipitate (~2.5 mass %) is separated from the mother liquor by centrifugation (150–300 rpm) and washed many times with water and/or another solvent (methanol, ethanol, DMF or chloroform). The final stage is activation (vacuum thermal treatment, replacement of the solvent or treatment with supercritical CO_2) directed towards the removal of the solvent from the framework.

The necessity to prepare MOFs in various forms (as a finely dispersed crystalline powder, film or coarse crystals) for different applications stimulated active development of the chemistry of MOFs and, as a result, gave rise to new

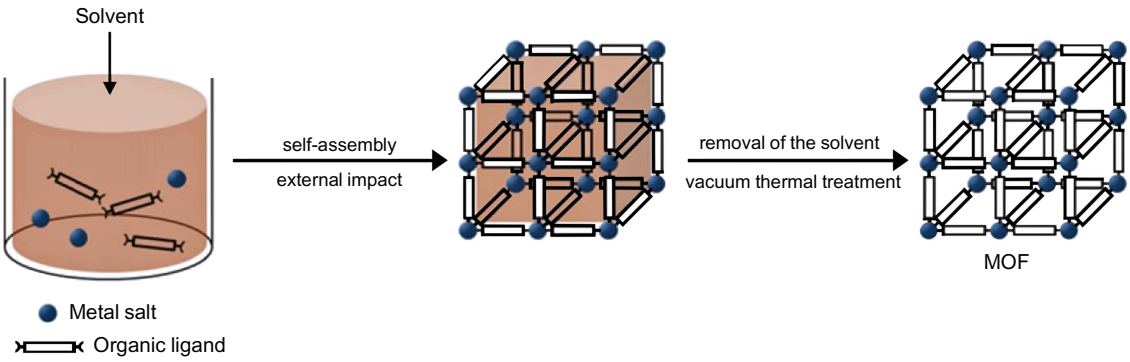


Figure 12. General scheme for the syntheses of MOFs *via* external impact (thermal, microwave, sonochemical) on the reaction mixture containing a metal salt solution and organic ligand in water and/or organic solvent.[99–114]

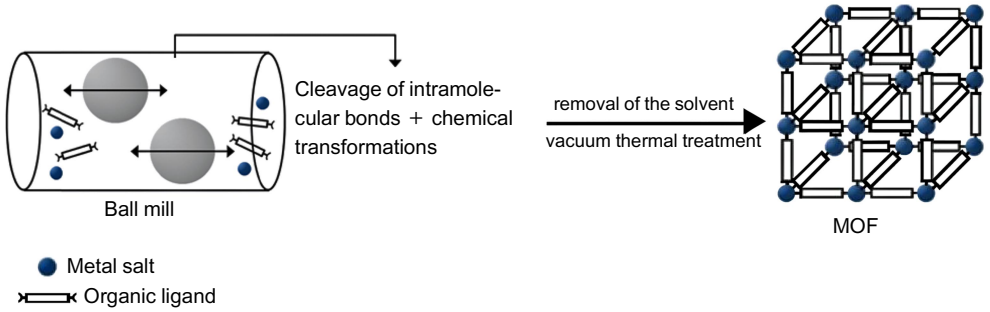


Figure 13. Mechanochemical synthesis of MOFs. The Figure is based on Refs 94–96, 115, 116.

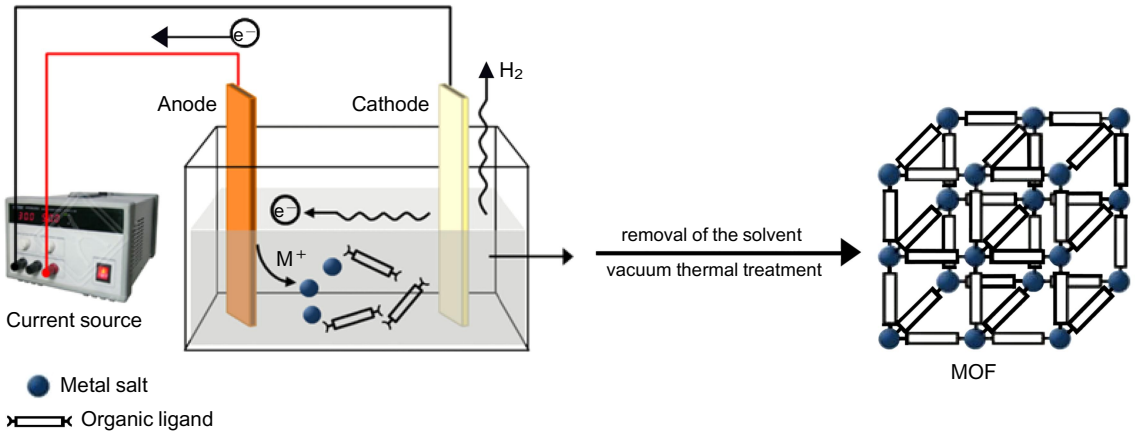


Figure 14. Electrochemical synthesis of MOFs (anodic dissolution). The Figure is based on Refs 94–96, 117.

synthetic procedures. In particular, the mechanochemical method implies the reaction between MOF precursors during their mixing without a solvent or with a small amount of a solvent followed by vigorous ball milling (Fig. 13). Two procedures of electrochemical synthesis are being actively developed.[116–119] According to the first procedure (Fig. 14), a sacrificial anode [in particular, copper plates; BASF patent for the manufacture of Basolite™ C300, Basolite™ Z377 (Ref. 117)] serves as a source of metal ions in the reaction medium (electrolyte + ligand). In this case, protic solvents (*e.g.*, methanol) prevent deposition of metal cations on the cathode. Excessive evolution of hydrogen is prevented by acrylonitrile and esters of acrylic and maleic acids. The second, so-called cathodic deposition, procedure makes use of a three-electrode cell[118] filled with an electrolyte (containing an organic ligand, metal ions and a source of anions) and affords a MOF as a film.

The conditions of synthesis of several MOFs using the most popular methods are summarized in Table 4.

Apart from the methods presented in Table 4, mention should be made of the ionothermal synthesis, which is a sort of solvothermal method using ionic liquids instead of organic solvents.[121, 122] The ionic liquids are low-temperature melts of organic salts (150–220 °C) consisting of bulky organic cations and inorganic (or organic) anions.[121] Ionic liquids were also used in microwave-assisted synthesis.[123]

The room temperature (RT) method is a successful attempt to carry out the synthesis under milder conditions compared with the solvothermal process.[124] Direct mixing of the reactants in the presence of solvents and triethylamine at room temperature afforded the MOF-5 structure. The duration of synthesis was 1–3 h. The RT method has the following advantages:

— the possibility to prepare MOFs with high crystallinity;

— relatively short reaction time;

— high porosity of the final product, which was demonstrated in the synthesis of a number of materials such as MOF-5, M-MOF-74, MOF-177, MOF-199 (HKUST-1) and IRMOF-0 [$Zn_4O(ADC)_4$, where ADC is acetylenedicarboxylate].[125]

Duan *et al.*[126] reported the superfast RT synthesis of zeolitic zinc imidazolate frameworks, ZIF-8, ZIF-61 and ZIF-90, possessing a hierarchical porosity. The synthesis was carried out at atmospheric pressure with organic heterocycles (imidazoles) as templates; the duration of synthesis was ~1 min. The space–time yield of the product was 1.29×10^4 kg m^{-3} day^{-1}. It was proposed to use this method for the preparation of MOFs on an industrial scale.

The synthetic procedures considered above provide gram amounts of MOFs in laboratory. However, effective application of MOFs in various fields of practical human activities requires larger amounts. The routine industrial manufacturing of MOFs, which are more and more in demand, depends on the yield and the accessibility of synthetic procedures. Currently, the companies that offer

Table 4. Key methods and conditions of MOF synthesis.

Method (see Figs 12 – 14)	Conditions				Examples of MOFs	Yield (%)	Ref.
	solvent	T/°C	duration /h	another parameter			
Hydro(solvo)thermal: heating of the	DMF, PhCl	120	24	1 [a]	IRMOF-*n* (MOF-5)	63	82
reaction mixture in an autoclave up to	DMF	120	24	1 [a]	UiO-66	–	102
or above the boiling point of the solvent	H_2O + 1 M HF	220	8	1 [a]	Cr-MIL-101	42	102
	H_2O + EtOH	180	12 – 24	1 [a]	HKUST-1	61	94, 104
	DMF	85	72	1 [a]	ZIF-8	60	105
	H_2O + HF + HNO_3	150	144	1 [a]	Fe-MIL-100	–	106
Microwave: microwaving of the reaction	H_2O + 1 M HF	220	4	–	Cr-MIL-100	44	107
mixture at 120 to 210 W accelerates the	NPM (1-methyl-2-pyrrolidone)	105	0.5	800 [b]	MOF-5	–	107
formation of crystallization sites and enhances the crystal growth	EtOH	140	1	300 [b]	HKUST-1	90	109, 110
	DMF	140	0.3	12 [b]	NH_2-MIL-101(Al)	–	111
Sonochemical: ultrasonic treatment	NPM	–	0.3	60 [b]	MOF-5	–	112
(> 20 kHz)	DMF, EtOH, H_2O	–	1	300 [b]	HKUST-1	–	113
	DMF, Et_3N or Et_3N + NaOH	–	1	300 [b]	ZIF-8	92 – 96	114
Mechanochemical: ball milling without	Without solvent or MeOH	–	0.25	25 [c]	HKUST-1	44	115
a solvent or with a minor amount of a solvent (7.5 mass %) to initiate the reaction	DMF	–	0.85 – 1	30 [c]	ZIF-8	–	116
Electrochemical							
anode (a copper plate) dissolution	MeOH	25	2.5	12 – 19,[d] 1.3 [e]	HKUST-1	–	117
cathode deposition (three-electrode cell;	DMF + MeOH [g]	25 – 40	1 – 3	50 [f]	ZIF-8	–	119
fluorine-doped tin oxide as the cathode;	DMF	25	6	2.5,[d]	MOF-5	–	120
Et_3N as the electrolyte)				0.1 – 100 [h]			

[a] Pressure /atm; [b] power /W; [c] frequency /kHz; [d] voltage /V; [e] current /A; [f] current /mA (zinc electrode; tributylmethylammonium methylsulfate as the electrolyte); [g] the possible variants are DMF + H_2O, DMF + H_2O + MeOH and DMF + EtOH; [h] current density /mA cm^{-2} (Et_3NH_2 as the electrolyte).

various MOFs in their catalogues (see Table 2) use, most often, the solvothermal (BASF, NuMat Technologies), mechanochemical (MOF Technologies, NuMat Technologies) and electrochemical (BASF) methods.

Rubio-Martinez *et al.*[35] listed the following key factors hampering the industrial implementation of most of MOF syntheses for routine commercial production:

— the use of expensive and highly toxic organic ligands (some of them are also fire hazardous);

— poor availability of initial compounds and ligands needed to prepare MOFs; methods for the synthesis of the ligands are also being developed;

— accumulation of corrosive nitrates and chlorides, which are formed when metal salts are used as precursors, in process units; therefore, the use of metal oxides and hydroxides is preferable;

— difficulty of controlling the MOF particle size; for gas storage technologies, large particles and monoliths are preferred, whereas membrane applications require small particles;

— the necessity to remove non-volatile solvents and unreacted starting components from MOF pores *via* the activation stage;

— the necessity of MOF shaping for applications in real industrial processes.

As alternatives to the solvothermal synthesis, the authors [35] proposed the above-mentioned mechanochemical and electrochemical syntheses and also continuous flows [127, 128] and spray dryings[129] processes. In 2018, the MOFapps company [130] reported the successful use of the last-mentioned process in the manufacture of a 30 kg batch of HKUST-1.

While considering the possibility to attain the DOE requirements to the adsorbent cost (10 US dollars per kg) [19] for ANG systems, authors of the techno-economic analysis [98] discussed the ways of reducing the expenses in each stage of solvothermal, hydrothermal and mechanochemical processes while considering the syntheses of four MOFs: HKUST-1, Mg-MOF-74, Ni-MOF-74 and MOF-5. The last-mentioned process implies preliminary wetting of the precursors with a slight amount of the solvent (7.5 mass %). These MOFs were chosen in view of their possible application in the adsorption storage of natural gas and hydrogen. The solvothermal synthesis of Mg-MOF-74 proved to be the most expensive, with expenditures for the solvent and compaction accounting for more than a half of the total cost (79%). The advantages of the mechanochemical method associated with lower cost of the solvent, shorter duration of synthesis and higher product yield were demonstrated.

Despite the above challenges hampering the implementation and the drawbacks of particular methods, BASF, MOF Technologies, NuMat and MOFapps are manufacturing more than 100 sorts of MOFs.[23] The BASF company is the holder of 2.5% of the total number of patents related to the synthesis, functionalization, shaping and various applications of MOFs.[23]

A necessary condition for using MOFs is their resistance to thermal, mechanical and chemical impacts. The instability of MOFs is due to the relatively low energy of coordination bonds. The thermal and chemical stability of MOFs depends on the nature of the organic linker and inorganic component. In the processes related to the separation or purification of gases, water is often present as a component of gas mixture. According to statements of some researchers, certain MOFs are thermally stable and retain their crystal structure in water vapour, *e.g.*, Al-MOF [Basolite™ A520 or Basolite™ A100 (see Table 2)] manufactured by BASF.[131] Zeolitic imidazolate frameworks such as ZIF-8 (Basolite™ Z1200) are hydrophobic materials and are also characterized by high thermal and chemical stability. According to Park *et al.*,[132] the structure of ZIF-8 does not change when it is immersed into boiling methanol or benzene or when it is kept in water for up to 7 days or in a concentrated sodium hydroxide solution at 100 °C for 24 h.

2.4. Functionalizaton of metal-organic frameworks

The formation of MOFs with specified structural and physicochemical properties, including adsorption properties, is possible not only during the synthesis, but also *via* functionalization.[24, 96, 97] In their first studies, Hoskins and Robson [55, 133] already assumed the possible applicability of crystalline micro- and mesoporous MOFs in catalysis or in ion exchange or sorption processes and pointed out the methods of introduction of functional groups both during the synthesis and after the synthesis (post-synthetic modification, see Fig. 10). The methods for MOF functionalization directed towards particular objectives are analyzed in detail in several reviews.[24, 96, 97, 133]

Butova *et al.*[24] noted that the number of publications devoted to MOF functionalization exceeds the number of studies on the synthesis of new compounds and optimization of synthetic methods. For example, when MOFs are used as adsorbents, it should be borne in mind that the MOF crystal lattice can be an inert solid matrix affecting the adsorption selectivity only by generating spatial restrictions. However, the concentration and accessibility of the adsorption sites specific to each adsorbed substance are also important factors affecting the efficacy of adsorbents. New adsorption sites can be generated upon encapsulation of macromolecules, organometallic compounds and metal or metal oxide particles.[133, 134–136] Adsorption sites can appear due to a change in the ligand environment of the metal centres caused by modification of organic linkers.

There are two ways to introduce functional sites into MOFs during the synthesis process: the ship-in-a-bottle method (synthesis of active sites inside the pores) and the bottle-around-a-ship method (formation of the MOF structure around ready active sites, or template synthesis).[134] The latter method was considered [135] in relation to the preparation of HKUST-1 in a solution containing palladium nanoparticles. The hydrogen adsorption capacity of the sample prepared in this way was 74% higher than the value found for palladium nanoparticles; the hydrogen absorption rate also increased after introduction of nanoparticles into the MOF shell. Sugikawa *et al.*[136] obtained highly porous functional materials by introducing gold nanoparticles into the solution during the synthesis of MOF-5.

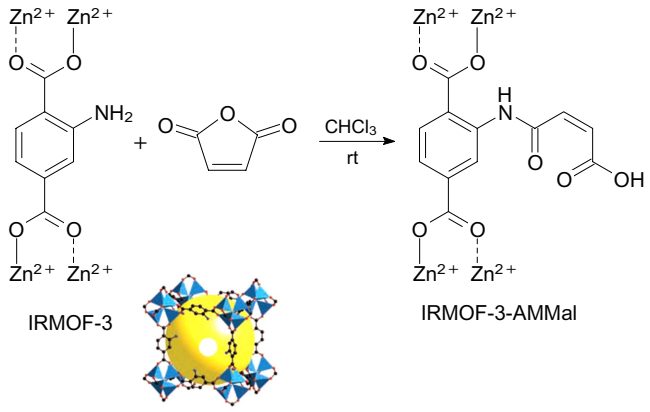


Figure 15. Covalent modification of IRMOF-3 *via* the reaction with maleic anhydride accompanied by ring opening.
AMMal is amino group modification with maleic anhydride. The Figure is adapted from Refs 82, 137.

Functionalization of organic linkers that connect the metal centres can be used to specify the properties of MOFs and, hence, to define the application area. After introduction of functional groups (hydroxy, amino, carbonyl, carboxyl, nitrile, azide, *etc.*) able to coordinate metal ions, the synthesis of MOFs can be retarded or terminated. However, if the chemical reactions with MOFs are conducted after the synthesis, these groups can be introduced into the crystal structure framework and thus it is possible to change (or modify) the properties of the starting material, for example, stability, hydrophobicity, sorption activity, *etc.* Cohen [137] surveyed the approaches to chemical post-synthetic modification of organic linkers within MOFs:

— covalent modification affecting both organic ligands and inorganic building units;

— exchange modification of inorganic building units and organic ligands;

— combining the two above procedures;

— surface modification;

— modification directed towards the formation of definite functional groups in organic ligands.

An example of covalent modification of IRMOF-3 *via* the reaction with cyclic maleic anhydride, which takes place at room temperature and is accompanied by ring opening, is depicted in Fig. 15. It was shown than the introduction of various rings and amide substituents into IRMOF-*n* enhances their capacity for storage of various gases including methane, carbon dioxide and hydrogen,[138] while the introduction of long-chain alkyl groups increases the chemical stability to protic solvents including water.[139, 140]

3. Metal-organic frameworks as methane adsorbents

3.1. Characteristics of the efficiency of natural gas storage systems

In recent years, increasing researchers' attention has been devoted to the adsorption technology of natural gas storage, which, as shown in the Introduction, has a number of advantages over the known CNG and LNG technologies.

Below we introduce the main parameters determining the efficiency of an adsorption system for natural gas storage. The key parameter determining the efficiency of these systems is the amount of the target substance (natural gas) that can be stored under particular thermodynamic conditions determined by the pressure (P) and temperature (T). In the general case, this parameter is represented by the total (absolute) adsorption (n_a /mmol g^{-1})

$$n_a(P,T) = n_e(P,T) + W_0\rho_g(P,T) \quad (1)$$

where $n_e(P,T)$ is the excess adsorption at the specified P and T values (mmol g^{-1}); W_0 is the volume of adsorbent micropores (cm^3 g^{-1}); $\rho_g(P,T)$ is the density of the free (bulk) gas phase at the specified P and T values (mmol cm^{-3}).

For evaluating the integral specific efficiency of an adsorption system representing a vessel filled with an adsorbent, it is necessary to take into account not only the adsorbed phase of the target gas, but also the free gas phase that occupies the adsorbent-free volume. In this case, the total specific capacity of the storage system including both the adsorbed and free gas phases is taken as the criterion.

The total volumetric specific capacity of a storage system (V_f) is the sum of the free and adsorbed phases of the target substance (gas) per unit volume of the closed system containing the adsorbent at specified pressure and temperature converted to standard (STP) or normal (NTP) thermodynamic conditions;[141–143] this value is also called the 'volumetric storage capacity'.[144] The term 'volumetric storage density' equivalent to the volumetric storage capacity is also used in the literature.

The ANG and CNG technologies are compared using the notion of relative efficiency of an adsorption storage system defined as the ratio of $V_{f\,ANG}$ (for an adsorption system) to $V_{f\,CNG}$ (for a compressed gas system) under identical thermodynamic conditions

$$\varepsilon(P,T) = \frac{V_{f\,ANG}(P,T)}{V_{f\,CNG}(P,T)} \quad (2)$$

It is important that apart from the total specific capacity, another important quantity characterizing operation of an ANG system is the deliverable volumetric specific capacity (V_d), *i.e.*, the productivity of the system. The deliverable volumetric specific capacity is defined as the amount of the gas (converted to STP or NTP) that can be recovered from an adsorbent-filled vessel of a particular volume during isothermal gas discharge with a pressure drop in the vessel from the current level P to a specified minimum value P_x divided by the geometric volume of the vessel. The P_x value is chosen considering the operation conditions: in foreign literature, for motor vehicle gas storage systems, it is accepted that $P_x = 0.48–0.58$ MPa, which corresponds to the minimum operation threshold for gas delivery to an engine. In Russian publications, P_x is taken to be equal to the atmospheric pressure.[145] The gas volume remaining in the system after the discharge is called undeliverable. The deliverable capacity V_d is found as the difference between $V_f(P,T)$ and $V_f(P_x,T)$ using the following relation:

$$V_d(P_x,T) = V_f(P,T) - V_f(P_x,T) \quad (3)$$

The graphical determination of V_d for $P = 6.5$ MPa and $P_x = 0.5$ MPa is illustrated in Fig. 16. It can be seen that

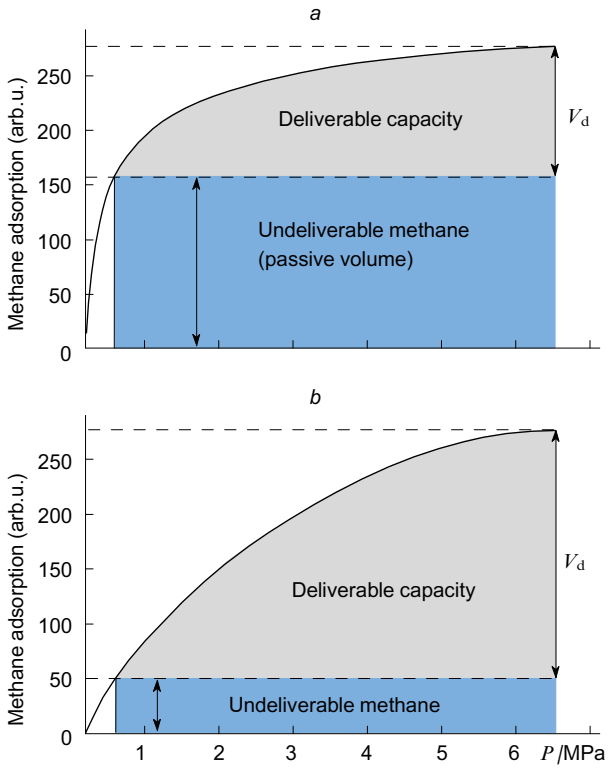


Figure 16. Examples of graphical determination of the deliverable capacity for an ANG system from methane adsorption isotherms (*a*) and for porous materials filling the adsorption tank (*b*) at $P = 6.5$, $P_x = 0.5$ MPa.
It can be seen that higher methane uptake at $P_x = 0.5$ MPa gives rise to a lower deliverable capacity. The Figure is based on Refs 13, 54.

the deliverable volumetric capacity of an ANG system can be maximized by selecting the adsorbent with the lowest possible methane storage capacity at a pressure of 0.5 MPa and the maximum possible capacity at 6.5 MPa.

The programme 'Methane Opportunities for Vehicular Energy' (MOVE) announced in 2012 for the design of methane storage systems,[19] which specified particular targets for V_f and V_d values for ANG systems at moderate pressures (3.5–6.5 MPa) and a temperature of 298 K, stimulated the studies of MOFs as adsorbents for natural gas storage. The pressure range of 3.5–6.5 MPa corresponds to the operating conditions of one- and two-stage compressors.[23, 26, 85]

Recall that natural gas is a mixture in which the methane content varies from 87% to 98%.[146] Hence, in the first approximation, adsorption of methane can be taken as a quite realistic model of natural gas adsorption.

3.2. Evaluation of the efficiency of metal-organic frameworks as adsorbents of methane

In a number of subject reviews (see, for example, Refs 85, 147–155), MOFs are demonstrated to favourably compare with other porous materials due to predictable crystal structure topology,[154, 155] which determines the regular and extensive porosity [82, 85] including the pore size and shape. In addition, the above-described methods for additional functionalization during and after the synthesis of MOFs can serve to control the porosity and openness of the metal

centres and, hence, the concentration of methane adsorption sites.[152, 153]

In the last two decades, investigations of the methane adsorption by MOFs have become more active. The foundation was laid by experiments carried out in 1997–2000 by Kitagawa's research group[156] on measurement of methane adsorption in the coordination hybrids $[M_2(BPY)_3(NO_3)_4](H_2O)_x$ (M = Co, Ni, Zn) and $[CuSiF_6(BPY)](H_2O)_x$ with permanent porosity. The methane uptakes for these structures were ~0.04 (M = Co, 298 K, 3.0 MPa)[157] and 0.104 g g^{-1} (298 K, 3.65 MPa),[156] which are higher than the values for 5 Å zeolite. The results of measurements of methane adsorption by the coordination hybrids are summarized in a review[158] in which comparison with MOFs is carried out, in particular, with the above-mentioned series of 16 highly crystalline IRMOF-*n* (Yaghi research group, 2000).[82]

Quite a few original studies and reviews indicating the efficiency of some MOFs as adsorbents for methane have appeared to date. Important results on the adsorption of methane were obtained for HKUST-1,[159] MIL-101(Cr),[160] UTSA-20,[161] NU-111,[162] NU-125 $\{Cu_3[C_6H_3(COO)_2.(C_2N_3H)]_3[C_6H_3]\}$,[163] PCN-14,[85, 164] NOTT-122,[165] UTSA-76 $[Cu_2L(H_2O)_2$, L is 5,5′-(pyrimidine-2,5-diyl)diisophthalic acid].[166] Mention should be made of the achievements of Professor Bai's group[167] on the development of efficient adsorbents for methane, namely, NJU-Bai series (the basic structure is PCN-14), for example, NJU-Bai-42 $\{[Cu_2(L2)(H_2O)_2]_n\}$ and NJU-Bai-43 $\{[Cu_2(L3)(DMF)_2]_n\}$ [L*n* are carbocyclic compounds derived from 5,5′-(anthracene-9,10-diyl)diisophthalate (ADIP) with heteroatoms in the ring].[167] In 2017, an international research group with participation of Russian scientists reported[168] high methane storage characteristics for materials based on divalent copper — MFM-112a $\{Cu_3(TDBB)(H_2O)_3$, TDBB is benzene-1,3,5-tris[(1,1′-biphenyl-4-yl)-3′,5′-dicarboxylate]} and MFM-115a $[Cu_3(NTBD)(H_2O)_3$, NTBD is 4′,4″,4‴-nitrilotribiphenyl-3,5-dicarboxylate; the letter 'a' implies activated material] (MFM stands for Manchester framework material). In the authors' opinion, the porous structure of MFM-115 is optimal for methane storage.[168] High methane storage characteristics were also found for UTSA-110 — $[Cu_2(L6)(H_2O)_2]_5\}$ — which continues the series of MOFs based on the NOTT-101 structure $[Cu_3(BDP)]$.[169]

Data on methane adsorption in MOFs are summarized in reviews,[147–155] which present estimates for total and deliverable adsorption capacities for methane (in both volumetric and gravimetric units) for tens of MOFs synthesized in the last two decades. In the review publications mentioned above,[85, 54, 147–155, 158] these values are analyzed and the key factors influencing V_f and V_d are elucidated. While looking for the optimal adsorbent for ANG systems that would be suitable for implementing the DOE targets of 2012, it seems important to identify the limiting possible methane uptake by a monolithic crystalline MOF and the amount of the gas released during desorption.

Wilmer *et al.*[170] made an attempt to determine the structure–property (in this case, methane uptake) relationship using high-throughput screening of 137 953 hypothetical MOFs generated as various combinations of 102 secondary building units (materials genome). Further, out of the model MOFs, 350 most efficient adsorbents for methane [$V_f \geqslant 230$ m^3(STP) m^{-3} at 3.5 MPa and 298 K] were successively selected in terms of the correspondence to the structural parameters of real compounds. Calculations and computer simulation of MOFs and methane adsorption isotherms resulted in identification of the optimal MOF, for which the highest V_f value was found: $V_f = 267$ m^3(STP) m^{-3} at 3.5 MPa and 298 K, *i.e.*, the DOE target for a monolithic MOF crystal was met [263–266 m^3(STP) m^{-3}].[19] The optimal hypothetical metal-organic framework actually proved to be a structural analogue of PCN-14 functionalized by methyl groups, namely NOTT-107 [Cu_2(TMBDI), TMBDI is 2,3,5,6-tetramethylbenzene-1,4-diisophthalate], for which $V_f = 213$ m^3(STP) m^{-3} was found experimentally at 3.5 MPa.[171] The difference between the calculated and experimental V_f values was attributed to the insufficient activation of pores after the synthesis of NOTT-107, which was also confirmed by the difference between a_s(BET) values.

The authors[170] also found that the specific surface area of metal-organic structures demonstrating the highest methane uptake at 3.5 MPa varies in the range from 2500 to 3000 m^2 g^{-1}. The optimal size of pores accommodating one and two methane molecules (0.4 and 0.8 nm, respectively) and the fraction of free space accessible for adsorption, or porosity (0.8) were estimated. It was found that the highest methane uptake is inherent in those hypothetical MOFs that contain methyl, ethyl or propyl groups. This gave certain guidelines for the search for the best metal-organic frameworks for methane adsorption. It is noteworthy that the presented estimates correspond to the methane adsorption data for UTSA-20 with two types of pores: 0.34 × 0.48 nm cavities and one-dimensional channels 0.85 nm in diameter [$V_f = 230$ m^3(STP) m^{-3}] at a temperature of 298 K and a pressure of 6.5 MPa. At 300 K and 3.5 MPa, the density of methane adsorbed in UTSA-20 pores is up to 0.22 m^3(STP) g^{-1}, which corresponds to methane density in CNG systems at 300 K and 34.0 MPa.[161]

The efficiency of MOF as a methane adsorbent with the highest deliverable volumetric capacity was confirmed theoretically using high-throughput screening of 650 000 porous materials [zeolites, zeolitic imidazolate frameworks ZIF, MOFs and porous polymer networks (PPNs)].[172, 173] Figure 17 shows the V_d values for methane at 6.5 MPa ($P_x = 0.58$ MPa) for all types of hypothetical adsorbents, depending on the crystal density, in comparison with the experimental data for the same conditions. Analysis of the results leads to the following conclusions:

— MOFs and PPNs have the highest deliverable capacity for methane storage;

— the maximum deliverable capacity calculated for hypothetical structures with the optimal parameters at 6.5 MPa and 298 K is V_d(calcd.) = 196 m^3(STP) m^{-3};

— experimental data for some MOFs are close to the maximum V_d(calcd.) values (Table 5);

— the highest value of 210 m^3(STP) m^{-3} was obtained for MOF-519 $[Al_8(OH)_8(BTB)_4(H_2BTB)_4]$ (Ref. 178).

Lin *et al.*[171] noted that a relatively high methane deliverable capacity is characteristic of MOF crystals with d_{cr} varying from 0.6 to 0.953 kg m^{-3} and the highest packing density for methane molecules is attained when the pore size is 1.1 nm.

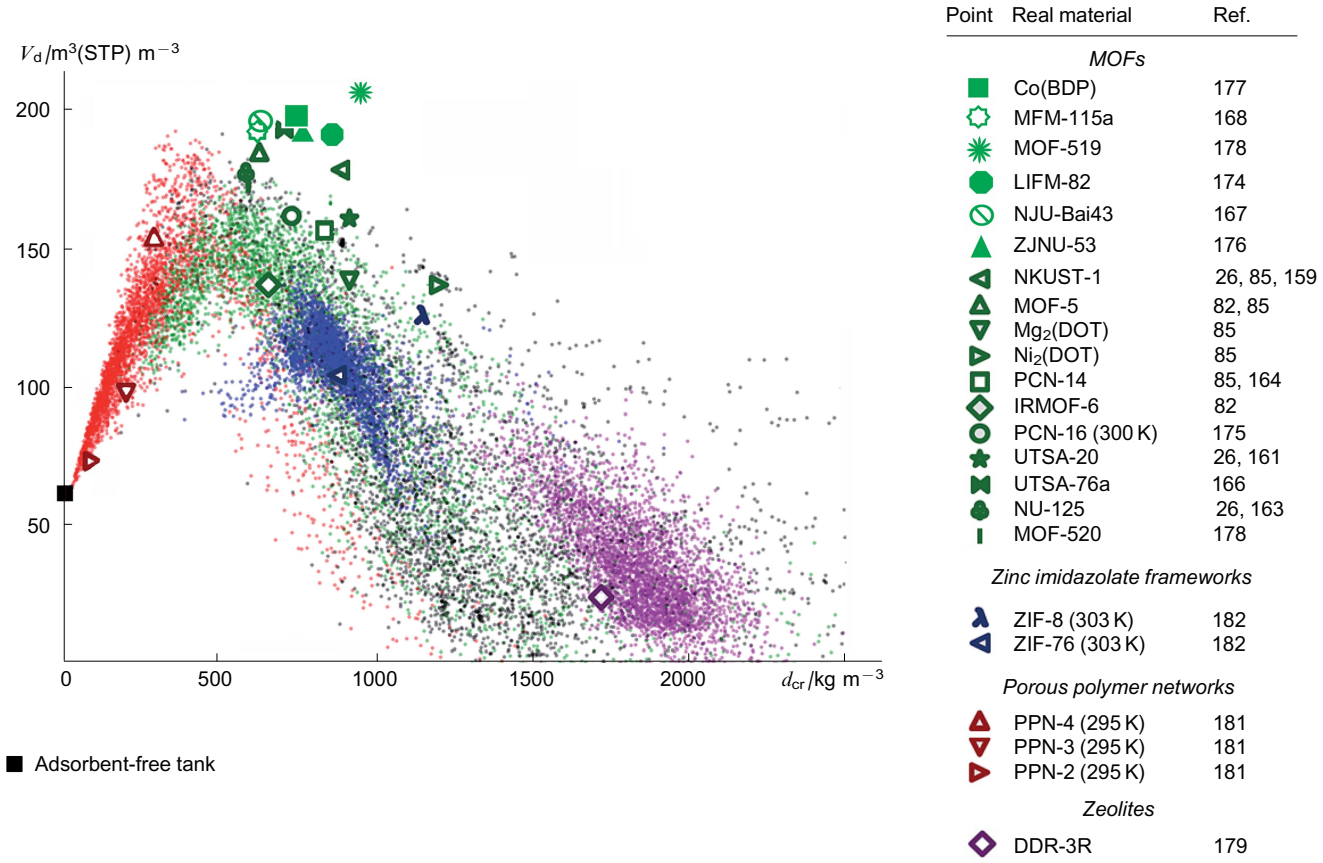


Figure 17. Arrays of points characterizing the dependence of the deliverable volumetric specific capacity for methane storage at $P = 6.5$ MPa ($P_x = 0.58$ MPa) and $T = 298$ K on the crystal density (d_{cr}) for hypothetical porous materials — MOFs (array of green points), ZIF (array of blue points), zeolites (array of red points), porous polymer networks (array of violet points) [172] — in comparison with experimental data for real materials (defined in the notes).
LIFM are MOFs synthesized at the Lehn Institute of Functional Materials; ZJNU are MOFs synthesized at the Zhejiang Normal University. The Figure is based on Refs 82, 85, 157, 158, 163–182.

Table 5. Calculated deliverable specific capacities of some MOFs.

MOF	V_d (calcd.) /m³(STP) m⁻³	Ref.
MOF-5	185	85
HKUST-1	185–190	26, 85, 159
ZJNU-53	190	176
MFM-115	193	168
LIFM-92	193	174
UTSA-76	194	167
Co(BDP)	197	177
NJU-Bai-43	198	167

3.3. Characteristic features of the mechanism of methane adsorption in metal-organic frameworks

The total and deliverable capacities of MOFs for methane storage depend on the adsorption mechanism and are calculated from particular adsorption isotherms of methane under definite thermodynamic conditions.

The nature, concentration and the accessibility (openness) of adsorption sites are important factors affecting the adsorption–desorption processes and, hence, the deliverable specific capacity for methane storage (see Fig. 17). The adsorption of methane molecules in a MOF is determined by electrostatic (Coulomb) interactions with open, coordinatively unsaturated metal ion sites (open metal sites, OMS) and by weaker van der Waals interactions with organic ligand moieties. Simon *et al.*[183] developed a model based on statistical thermodynamics for the adsorption of methane in MOF micropores; in terms of this model, a linear relationship was obtained between the deliverable capacity of the adsorbent and the number of methane adsorption sites. It is assumed that each adsorption site is associated with one MOF cage; the interaction between an adsorption site and a gas molecule being adsorbed can be both van der Waals and electrostatic. If the metal-organic framework is formed by sufficiently mobile ligands linking the adsorption sites in neighbouring cages, adsorption is cooperative. In this case, adsorption isotherms are S-shaped and the maximum methane deliverable capacity of the MOF can be attained.

The effect of spatial distribution and nature of the MOF – methane interaction sites on the methane uptake was considered using the Monte Carlo method [184] with the view of elucidating the theoretical possibility to achieve the DOE target of 2012. The model of adsorption of a methane molecule in MOF was complicated step by step: first, idealized adsorption in special areas of the MOF porous space (so-called adsorption pockets for methane molecules)

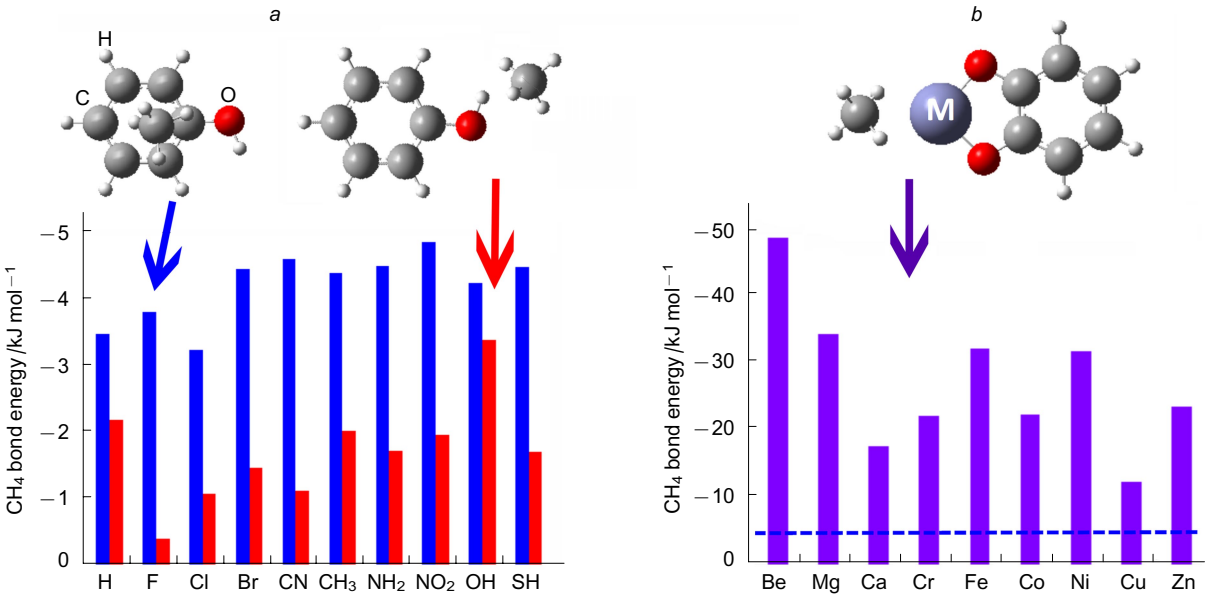


Figure 18. Diagrams of methane interaction energy with various functional groups based on quantum mechanical calculations. (*a*) Two types of binding of a methane molecule benzene ring monosubstituted with various functional groups: one with methane binding on top of the ring (blue bars), and another with methane side binding to the functional group (red bars); (*b*) interaction of a methane molecule with a catechol group incorporating a divalent metal (coordinatively unsaturated site) with the corresponding bond energies; for comparison, dashed line shows the highest bond energy in Fig. *a*. The Figure is adapted from Ref. 184.

was considered; then the MOF cage topology was analyzed and, finally, the interactions of the methane molecule with coordinatively unsaturated sites incorporated into the adsorbent as organic linkers were taken into account. As such sites, metallated catechol groups were proposed (Fig. 18); according to authors's calculations, these groups do not considerably decrease the pore volume and provide values exceeding the DOE requirement [$V_f = 390$, $V_d = 217$ m^3(STP) m^{-3} at 6.5 MPa] for functionalized IRMOF-10 structure [Zn_4(BPDC)]. The optimal MOF cage topologies that provide the highest V_d values are pcu-2 [223 m^3(STP) m^{-3}], bcu-2 [222 m^3(STP) m^{-3}] and dia-1 [254 m^3(STP) m^{-3}] with heats of adsorption of ~18, ~16 and ~14 kJ mol^{-1}.

We will compare the obtained results with the data on methane adsorption measurements for several MOFs with different porous structures and adsorption sites with different natures and densities.[85, 185] The series M-MOF-74 (M = Mg, Mn, Co, Ni, Zn) (see Fig. 8) is characterized by a uniform porous structure and high density of OMS involved in the electrostatic interaction with a methane molecule and, hence, these materials show fairly high total volumetric capacity for methane storage (Table 6).[85] Furthermore, the highest V_f and V_d values are observed for methane adsorption in Ni-MOF-74: 230(267) and 115(142) m^3(STP) m^{-3} at 3.5(6.5) MPa. As follows from the data for M–CH_4 bond energy (see Fig. 18), magnesium and nickel cations are the strongest methane adsorption sites in the given series of MOFs. Analysis of neutron diffraction data demonstrated [185] that all OMS in the M-MOF-74 framework serve as the primary adsorption sites and are bound to only one methane molecule, which thus becomes itself an adsorption site. Nevertheless, it is important that electrostatic interaction between OMS and a methane molecule makes the greatest contribution by increasing adsorption and hampering desorption, which leads to decreasing V_d value.

Table 6. V_f and V_d for M-MOF-74 frameworks (M = Mg, Mn, Co, Ni, Zn).

MOF	V_f /m^3(STP) m^{-3}	V_d /m^3(STP) m^{-3}	Q_{st} /kJ mol^{-1}	Ref.
Ni-MOF-74	230	115	20.6	85, 185
Co-MOF-74	221	110	19.5	85
Mg-MOF-74	200	113	18.5	85
Zn-MOF-74	188	102	18.3	185
Mn-MOF-74	176	100	19.1	185

The positions and orientation of methane molecules in the high-performance HKUST-1 adsorbent were determined by powder neutron diffraction, computer simulation and density functional theory calculations.[186] Like in M-MOF-74, the primary methane adsorption sites are open metal cations (Cu^{2+}); complete filling of these sites results in the volumetric methane storage density of 98 m^3(STP) m^{-3}. However, the more sophisticated pore system in HKUST-1 (the presence of three types of pores, see Fig. 9) generates additional adsorption sites located in four 'windows' to each octahedral cage [85, 186] (Fig. 19). In these windows (adsorption pockets), the methane molecule is involved in van der Waals interactions with several oxygen atoms belonging to the MOF cage, with the O–CH_4 distances ranging from 0.28 to 0.32 nm. According to an estimate,[85] saturation of the weaker sites leads to an increase in the uptake by 66 m^3(STP) m^{-3} and provides a higher gravimetric methane storage capacity

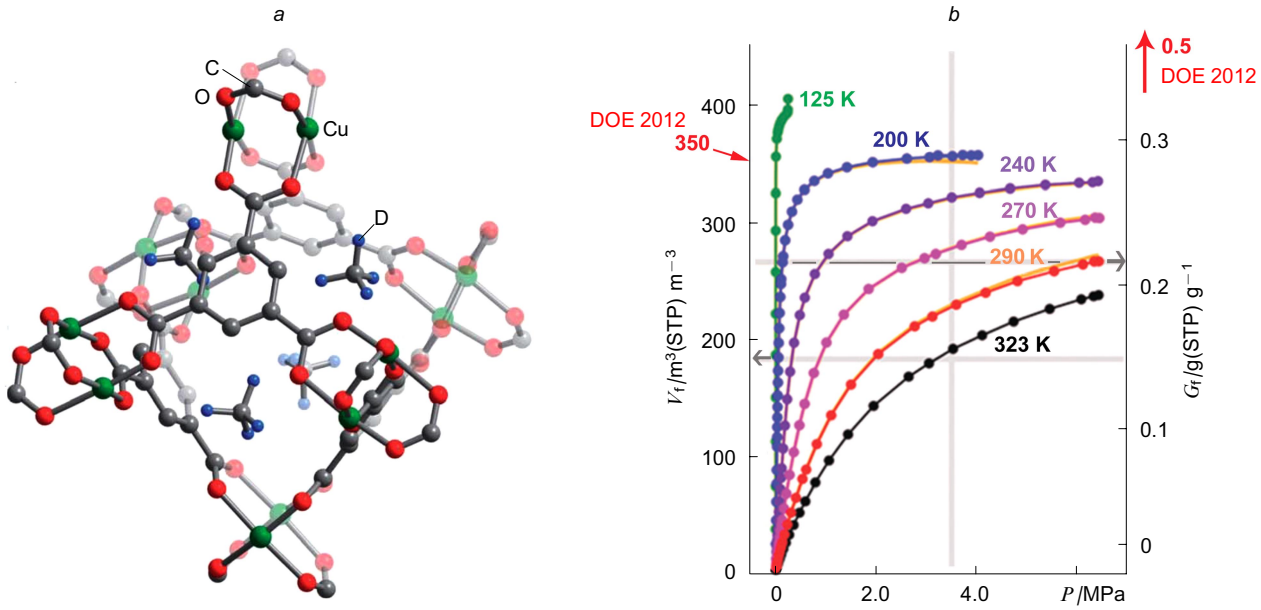


Figure 19. Positions of adsorbed CH_4 molecules in four windows of the octahedral cage derived from neutron diffraction data (*a*) and methane adsorption isotherms in HKUST-1 at different temperatures (*b*).
The hydrogen atoms are omitted. The grey lines indicate the DOE requirement for ANG systems set in 2000; the red arrows mark the target total volumetric (V_f) and gravimetric (G_f) capacities for methane storage determined in 2012 taking account of the adsorbent packing density.[20] The Figure is based on Refs 85, 150, 186.

[185 cm^3(STP) g^{-1}] compared to that observed for Ni-MOF-74 [144 cm^3(STP) g^{-1}].

Particularly, the predominant number of the sites of interaction between methane molecules and framework atoms in the cage windows is responsible for the higher methane deliverable capacity inherent in HKUST-1 compared with Ni-MOF-74 [the V_d values at 3.5 and 6.5 MPa are 150 and 190 m^3(STP) m^{-3}, respectively]. Note that both adsorbents meet the DOE criterion of 2000 under standard conditions; however, to meet the new requirement of 2012, taking account of the packing density [350 m^3(STP) m^{-3}], it is necessary to lower the methane storage temperature, for example, for HKUST-1, down to 200 K.[85] Similar recommendations to change the thermodynamic conditions of methane storage were also stated for other MOFs, for example, in the review of Li *et al.*[149] and in the computer simulation and screening studies.[171, 183, 184]

However, Gomez-Gualdron *et al.*[184] assumed that the V_f and V_d values of 350 and 315 m^3(STP) m^{-3}, respectively, are also possible at 298 K for a functionalized MOF with sufficiently flexible ligands containing coordinatively unsaturated adsorption sites. The key paths towards this goal are associated with the rational selection or functionalization of ligands and with the complexity of implementing the conditions of synthesis and functionalization of optimal MOFs.

3.4. Ligand functionalization as a way to increase the efficiency of metal-organic frameworks

The key methods used to attain the highest efficiency of MOFs for methane adsorption imply increase in the concentration of adsorption sites and certain tuning of the porosity by functionalization of ligands.

Indeed, experimental measurements of methane adsorption in MOFs demonstrated that the introduction of functional groups that act as adsorption sites leads to increasing volumetric uptake.[162, 166, 168, 178] For example, UTSA-75, 76 and ZJU-5a (Fig. 20) and UTSA-78, 79a enriched with pyrimidine groups have higher V_f [~260 m^3(STP) m^{-3} at 298 K and 6.5 MPa for UTSA-76a] than the prototype NOTT-101a.[166] In addition, functionalized MOFs are distinguished by higher productivity at 298 K and 6.5 MPa [from 188 m^3(STP) m^{-3} for UTSA-77 and ZJU-5a to 194 m^3(STP) m^{-3} for UTSA-76a] than NOTT-101 [188 m^3(STP) m^{-3}].

The porous system of UTSA-76 is formed by two types of cages: cubic (1.2 nm) and elongated polyhedron-shaped cages (0.9 × 2.3 nm). The concentrations of OMS (Cu^{2+}) and Lewis nitrogen sites in UTSA-76 proved to be equal, amounting to 2.64 mmol cm^{-3}, which provides moderate methane uptake at 0.5 MPa [~60 m^3(STP) m^{-3}] and considerable uptake at 3.5 MPa [211 m^3(STP) m^{-3}]. Li *et al.*[166] asserted that at 6.5 MPa, the UTSA-76 framework has a higher productivity than HKUST-1. The isosteric heat of methane adsorption by UTSA-76 amounts to 15.44 kJ mol^{-1} and barely changes with increasing coverage.

Further elongation of the organic ligand and incorporation of two pyrimidine heteroatoms *via* isoreticular synthesis afforded the UTSA-110 metal-organic framework [168] with high density of amide groups and a mesoporous structure formed by two types of cages, shaped as elongated polyhedra (0.96 × 2.86 nm) and as cuboctahedra (1.05 × 1.4 nm). The performed measurements of methane adsorption in UTSA-110 demonstrated a high methane storage capacity at 298 K and 6.5 MPa [241 m^3(STP) m^{-3}]. In combination with moderate methane uptake at 0.58 MPa [51 m^3(STP) m^{-3}], this gives V_d = 190 m^3(STP) m^{-3}, which is greater than this value

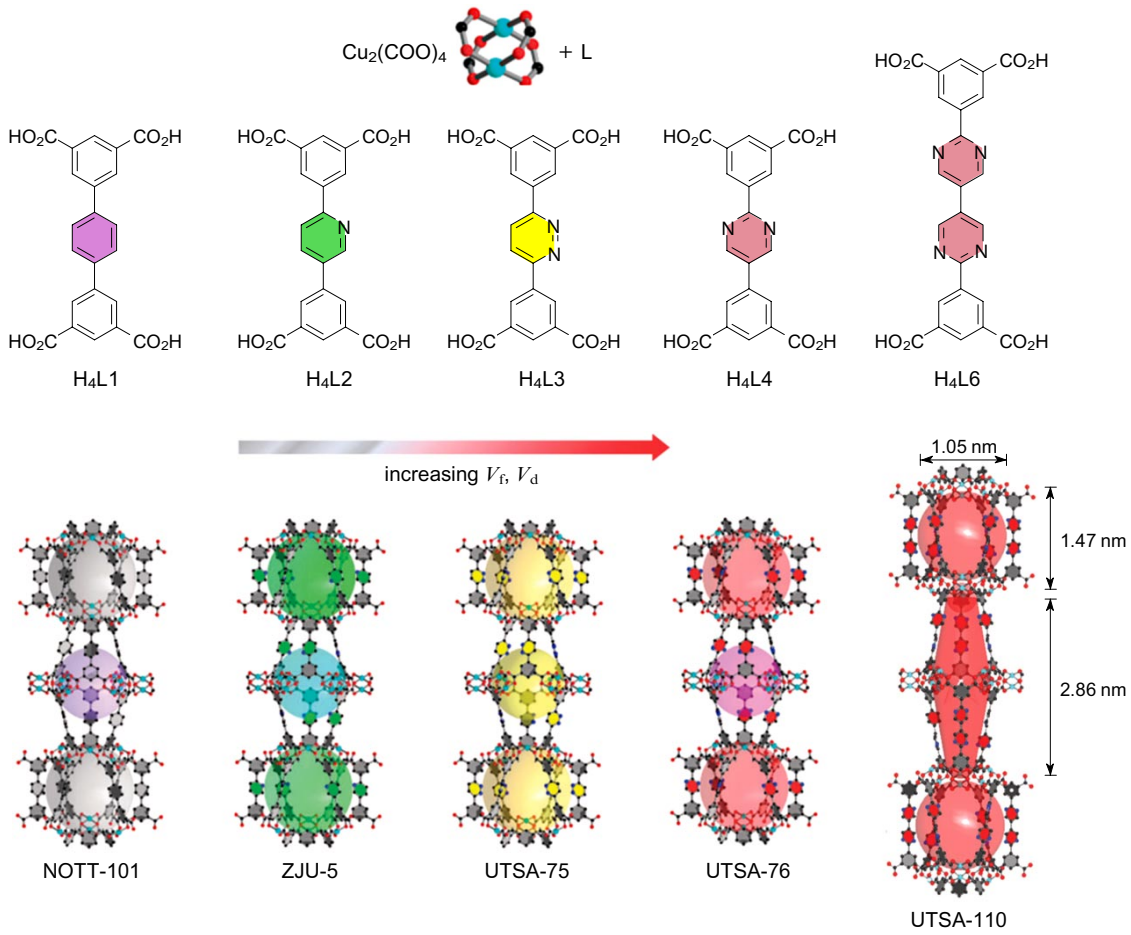


Figure 20. Tuning of a porous system and MOF functionality by elongation of the ligand and incorporation of functional groups (L2, pyridine; L3, pyridazine; L4 and L6, pyrimidine) for the following metal-organic frameworks: NOTT-101, ZJU-5, UTSA-75, UTSA-76 and UTSA-110.
Spheres designate free volumes within the MOF cages; the hydrogen atoms of MOFs are omitted. The Figure is based on Refs 166–168.

for known efficient MOFs such as HKUST-1 [183 m^3(STP) m^{-3}] [26] and UTSA-76 [187 m^3(STP) m^{-3}].[166]

An example of the rational approach to the synthesis of optimal MOF is the fabrication sequence of NJU-Bai-*n* frameworks, which can be regarded as evolution of the quite efficient methane adsorbent PCN-14 (Fig. 21).[167, 187, 188] The amide groups in the ligands L1–L3 incorporated between the carboxyl groups and phenyl groups of the ligand L = ADIP, first, increase the flexibility of the framework and, second, participate in the hydrogen bonding and, hence, in coordination; this changes the topology and porosity of the MOF (see Fig. 21).[167, 187, 188]

The NJU-Bai-43 framework resulting from the replacement of half of the oxamide groups in NJU-Bai-42 by pyridine rings has rather high methane deliverable capacity at 298 K. The method for incorporation of amide functional groups between the carboxyl and phenyl groups of the organic ligand is described in detail in a review,[188] which also analyzes the changes in the MOF topology and the applicability of MOFs for methane absorption. Comparison of the methane adsorption isotherms for the prepared NJU-Bai-*n* and PCN-14 metal-organic frameworks (Fig. 22) indicates that higher methane deliverable capacities in NJU-Bai-43 [V_d = 198 m^3(STP) m^{-3} at 6.5 MPa and 298 K] and NJU-Bai-42 [193 m^3(STP) m^{-3}] compared with NJU-Bai-41 [172 m^3(STP) m^{-3}] and PCN-14 [157 m^3(STP) m^{-3}] are due to their lower methane uptakes at low pressure in comparison with other MOFs and higher uptakes at $P > 4.0$ MPa.

A review of Bai and co-workers[188] considers the synthesis involving two types of secondary building units, $[Cu_2(COO)_4]$ and $[Cu_3COO)_6]$, and the asymmetrical tricarboxylate ligand with amide groups. This synthesis gave the NJU-Bai-3 adsorbent, $Cu_3L_2(H_2O)_5$, where H_3L is 5-(4-carboxybenzoylamino)isophthalic acid, with mesoporous structure comprising three types of cages, each containing amide groups, which serve as primary methane adsorption sites. One more efficient adsorbent belonging to this series, NJU-Bai-9, was obtained by solvothermal synthesis from $Zn(NO_3)_2 \cdot 6H_2O$ and an organic ligand (dicarboxylate ligand based on pyridine functionalized by two amine groups, H_2BCP, where H2BCP is 3,5-bis(4-carboxyanilinocarbonyl)pyridine), which acts as a donor of pyridine and amide electron pairs.[188] This resulted in high gravimetric capacity for methane storage at 7.0 MPa: 0.21 and 0.4 g g^{-1} at 298 and 273 K, respectively.

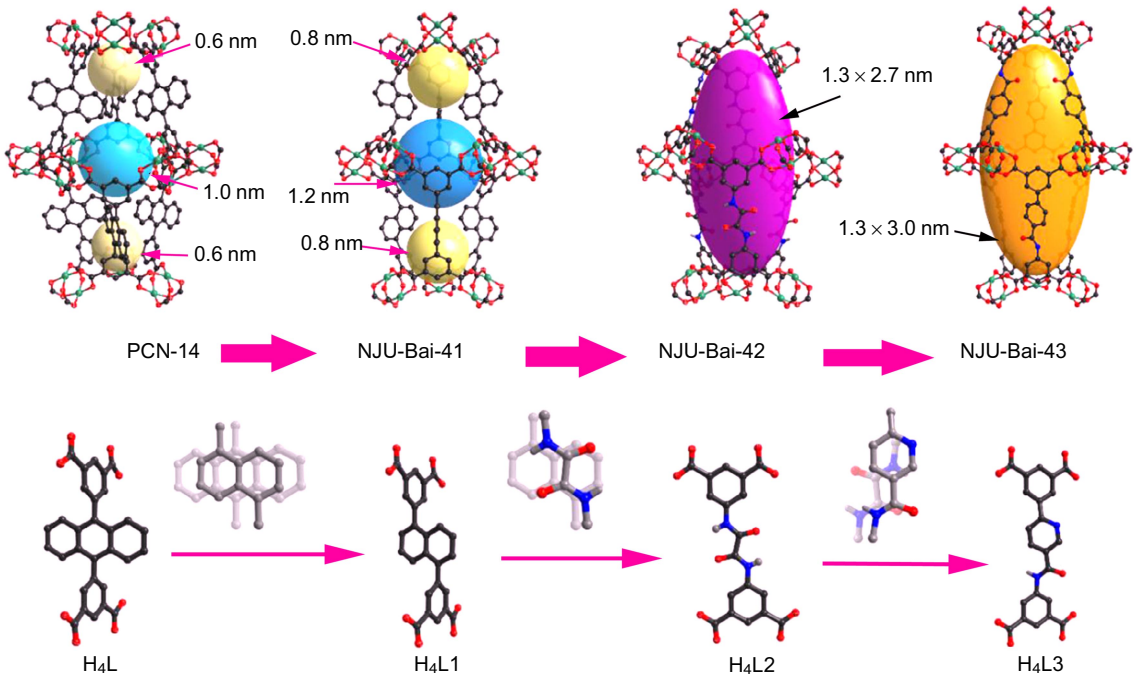


Figure 21. Evolution of metal-organic frameworks from PCN-14 to NJU-Bai-43 by functionalization of the organic ligand ADIP (L) with amide groups.
Spheres designate free volumes within the MOF cages. The hydrogen atoms are omitted. The Figure is based on Refs 167, 187, 188.

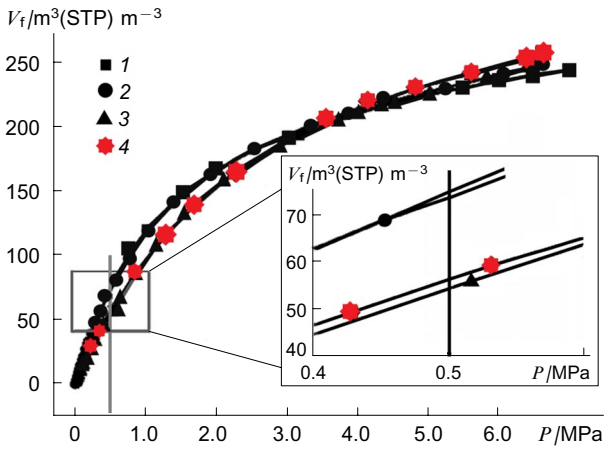


Figure 22. Experimental isotherms of methane adsorption by PCN-14 (*1*), NJU-Bai-41 (*2*), NJU-Bai-42 (*3*) and NJU-Bai-43 (*4*) at 298 K.
The Figure is adapted from Refs 187, 188.

Worthy of note is the study by Liang *et al.*,[189] who used several ligands to carry out solvothermal synthesis of a series of ST-*n* frameworks (n = 1, 2, 3, 4).‡ By combining the ligand derived from the tribasic acid H_3TATAB (TATAB is 4,4′,4″-triazine-2,4,6-triyltribenzoate) with the carboxylate ligands derived from dibasic acids H_2BDC, H_2NDC (1,4-naphthalenedicarboxylate) and H_2BPDC, the following frameworks were prepared: $(Zn_4O)_3(TATAB)_4(BDC)_3$ (ST-1), $(Zn_4O)_3(TATAB)_4(NDC)_3$ (ST-2) and $(Zn_4O)_5(TATAB)_6(BPDC)_6$ (ST-4). The ST-3 framework described as $(Zn_4O)_3(TATAB)_4(BPDC)_2(BDC)$ was obtained[189] by using three ligands: TATAB, BDC and BPDC. The ST-2 sample (umt topology) proved to be the most efficient for methane adsorption; its porous structure comprises four types of pores, with sizes varying from 0.8 to 3.3 nm. Apparently, the presence of pores with an optimal size for a methane molecule and the presence of an additional heteroatom are responsible for high methane total and deliverable capacities of the ST-2 framework in the 0.5–8.9 MPa pressure range [187 and 160 m³(STP) m⁻³] and a record-high productivity equal to 289 m³(STP) m⁻³ at 0.5–20.0 MPa. It is also noteworthy that methane adsorption in ST-2 has a moderate isosteric heat (9.2 kJ mol⁻¹).

Mention should be made of ambiguous outcome of incorporation of functional groups found by measuring the methane adsorption for MOF-905 [Zn_4(BTAC)$_2$, pyr topology, BTAC is benzene-1,3,5-tri-β-acrylate], the porous structure of which is formed by 1D channels 0.85 nm in diameter, and for isoreticular derivatives based on this framework that were synthesized using two ligands, one being BTAC and the other being selected out of BDC (MOF-950), BDC-Me (MOF-905-Me_2), H_2NDC (MOF-905-Naph) and H_2BDC-NO_2 (MOF-905-NO_2).[181] Initially, the authors attempted to increase the methane uptake by incorporating the functional groups of the second ligand. It was found that the mesopore size decreased from 2.5 to 1.5 nm and the micropore size increased from 0.5 to 0.68 nm. The authors' expectations came true for 298 K and 3.5 MPa, with the highest uptake being observed for MOF-950-Naph [146 m³(STP) m⁻³]. However, when pressure was increased to 8.0 MPa, the total methane uptake

‡ ST are a series of MOFs synthesized at the Shanghai Tech University.

was lower for MOF-950-Naph than for the initial framework. The deliverable capacity of MOF-905, equal to 203 m^3(STP) m^{-3} at 6.5 MPa, proved to be the highest among the deliverable capacity values of all known zinc-based MOFs. Note also the ambiguous relationship between heats of adsorption (Q_{st}) for the series of MOFs prepared by Lu *et al.*:[181] for all isoreticular MOFs with added functionality, except MOF-905-Me_2, the heat of adsorption (10.3–11.3 kJ mol^{-1}) was lower than that for the initial MOF-905 (11.7 kJ mol^{-1}). The authors suggested that the added functional groups block the access of methane molecules to the primary adsorption sites of $Zn_4O(COO)_6$.[190]

A doubt of whether the concentration of the open metal sites in the MOF lattice is correlated with the methane uptake was expressed for the MAF-38 framework ($[Zn_3(PYPZ)_3(BTC)]$), which has no OMS.[191] The MAF-38 material was obtained by a solvothermal reaction between a Zn(II) salt and organic acids HPYPZ and H_3BTC. The hierarchical porous 3D structure comprises two types of polyhedral cages formed by different structural units and ligand groups differing in size and connected by six trigonal windows. Regarding the methane uptake and deliverable capacity, MAF-38 differs little from other efficient methane adsorbents.

P/MPa	3.5	6.5	8
V_f/m^3(STP) m^{-3}	226	263	273
V_d/m^3(STP) m^{-3}	150	187	197

The hierarchy of the methane adsorption sites in MAF-38 was determined using Monte Carlo simulation and periodic density functional theory calculations. The advantage of the primary adsorption sites located in narrow windows connecting the framework cages is due to multiple host–guest contacts including C–H···O and C–H···N hydrogen bonds and C–H π interactions. In this hierarchical porous system, adsorption of methane molecules occurs *via* interaction with both the framework and methane molecules located in the adsorption sites, *i.e.*, the adsorption is cooperative. The initial heat of adsorption in MAF-38 (21.6 ± 1.8 kJ mol^{-1}) is close to the analogous value for Ni-MOF-74 (21.4 kJ mol^{-1})[85] in which the adsorption mechanism is mainly determined by OMS.

Yan *et al.*[168] proposed a method for tuning the porous system of MOFs towards methane adsorption in relation to the series MFM-112a, MFM-115a and MFM-132a ($[Cu_3(BTAT)(H_2O)]$) by changing the functionality of the central core of the hexacarboxylate organic ligand (at the connection point of three isophthalate groups during the solvothermal synthesis: $Cu(NO_3)_2 \cdot 2.5\,H_2O + H_6BTAT$ {H_6BTAT is 5,5′,5″-(benzene-1,3,5-triyl-tris(anthracene-10,9-diyl)]triisophthalic acid}. Indeed, adsorption measurements for MFM-112a, MFM-115a and MFM-132a showed rather high methane deliverable capacity, m^3(STP) m^{-3}:

MFM-112a	MFM-115a	MFM-132a
6.5 MPa *pressure;* 298 K *temperature*		
181	191	150
8 MPa *pressure;* 298 K *temperature*		
200	208	162

The molecular mobility in the MOF–methane adsorption systems was studied by ^2H NMR spectroscopy; it was shown that narrow pores with an optimal size for a methane molecule are the primary adsorption sites. The isosteric heats of adsorption at low coverages were 16.2, 16.3 and 15.7 kJ mol^{-1} for MFM-112a, MFM-115a and MFM-132a, respectively; these values are close to those for MOFs with open Cu^{II} metal sites.[192]

It is noteworthy that highly porous MOF-519 $[Al_8(OH)_8(BTB)_4(H_2BTB)_4]$ and MOF-520 $[Al_8(OH)_8(BTB)_4(HCOO)_4]$ are among the most efficient adsorbents for methane.[178] The two materials have similar structure, but in MOF-520, four formate groups replace four terminal BTB ligands, which produces a larger pore volume compared with MOF-519. Nevertheless, the total capacity values found for MOF-519, which amount to 200, 250 and 279 m^3(STP) m^{-3} at 298 K and pressures of 3.5, 6.5 and 8 MPa, respectively, exceed the V_f values for MOF-520, which are 162, 215 and 231 m^3(NTP) m^{-3} under the same conditions. MOF-519 also shows a very high desorption performance, being able to release a large amount of methane: 151 and 230 m^3(NTP) m^{-3} as pressure drops from 3.5 to 0.5 MPa and from 8 to 0.5 MPa, respectively.

3.5. Structure–property relationship for metal-organic frameworks

A series of studies carried out at the Frumkin Institute of Physical Chemistry and Electrochemistry, Russian Academy of Sciences,[25,193–197] partly together with the Public Joint Stock Company Gazprom, addressed heats of methane adsorption and the effects of precursors, porous system parameters and packing density on methane adsorption. Methane adsorption isotherms for various MOFs were measured at pressures of up to 40 MPa and temperatures of 303, 313, 323 and 333 K. The MOFs for investigation included industrial samples provided by BASF and laboratory samples synthesized by the solvothermal method. The crystal structures and compositions of laboratory samples were determined and confirmed by small- and medium-angle X-ray scattering, powder X-ray diffraction and scanning electron microscopy. The stability of MOFs prepared in laboratory was studied by thermogravimetry.

The porous structure parameters of MOFs obtained from nitrogen adsorption isotherms at 77 K using the Dubinin–Radushkevich equation are summarized in Table 7.

For estimation of the heats of methane adsorption in MOFs, the differential molar isosteric heats of adsorption q_{st} (kJ mol^{-1}), *i.e.*, the heats released at a definite absorbed amount n_a, were determined from adsorption isotherms at different temperatures. The calculations were performed using the Bakaev equation (see Ref. 10 in Ref. 196) derived by a statistical thermodynamics method taking account of system deformation, non-ideality of the gas phase and other factors. It was found that almost for all MOFs, q_{st} decreases with increasing adsorbed amount (see, for example, Fig. 23), which is attributable to energetic inhomogeneity of the adsorbents towards adsorption.

The maxima observed in the dependences $q_{st} = f(n_a)$ for C300 in the n_a range from 4 to 5 mmol g^{-1} and MOF-199 for n_a = 1.5 mmol g^{-1} (Ref. 196) are caused by the contribution of adsorbate–adsorbate interactions, which are inherent in adsorbents with narrow pore size distributions. Note that the size of pores in C300 (0.8 nm) is close to

Table 7. Parameters of porous MOFs: specific surface area (a_s), total pore volume (W_t), micropore volume (W_0) and size (X_0), packing density (d_p).

MOF	a_s (BET) /m^2 g^{-1}	W_0	W_t	X_0 /nm	d_p /g cm^{-3}	Ref.
		cm^3 g^{-1}				
MOF-199 [a]	1400	0.32	—	0.7	0.511	25
Al-BTC [a]	1422	0.59	1.17	0.8	0.436	193, 196, 197
C300 (BASF) or HKUST-1	1667	0.75 (0.73)	—	0.80	0.473	193, 196
Z205 (BASF), $Zn_4O(ADC)_4$	5399	2.74 (2.83)	—	2.12	0.231	193, 196
A520 (BASF)	1033	0.57 (0.54)	—	1.24	0.201	193, 196

Note. The adsorption volumes calculated from total methane uptake isotherms at 303–333 K according to the method reported in Ref. 198 are given in parentheses. [a] Laboratory samples.

$X_0 = 0.85–0.95$ nm, which was found from the average effective pore width (1.0–1.1 nm), taking account of the carbon atom radius; according to calculations,[198] this pore width corresponds to the highest density of methane upon adsorption in micropores. Large-pore samples (A520, Al-BTC, Z205), which are characterized by lower density of adsorbed methane, show a decrease in q_{st}. When adsorption occurs in micro- and mesopores, the adsorbate–adsorbent interaction energy rapidly decreases with increasing pore size, which determines the form of the dependence of adsorption heats on the uptake observed for Al-BTC (see curve *2* in Fig. 23). In the case of methane adsorption in the Z205 sample, both the initial heat of adsorption and the heat of complete filling were markedly lower than these values for C300 or Al-BTC (see curve *3* in Fig. 23). The capacity characteristics of ANG systems are determined by the amount of heat evolved upon filling, as this determines the temperature regime of the process, with temperature rise resulting in a decrease in the adsorption.

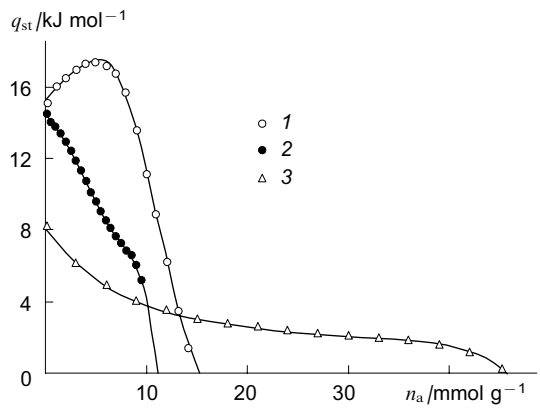


Figure 23. Differential isosteric heat of methane adsorption *vs.* methane uptake in C300 (*1*), Al-BTC (*2*), Z205 (*3*) at 303 K.[195]

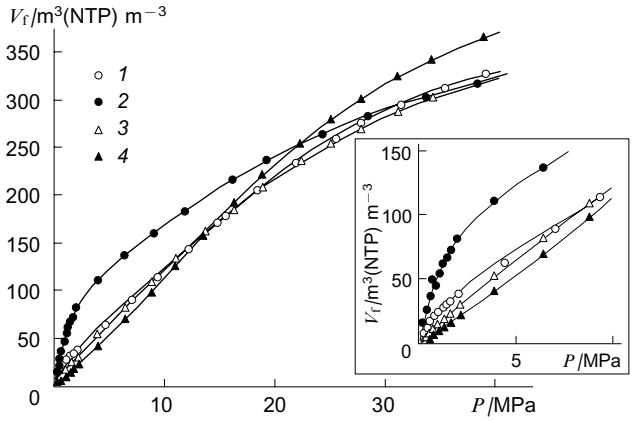


Figure 24. Volumetric methane storage capacity *vs.* pressure at a temperature of 303 K in an adsorption storage system packed by powdered adsorbents A250 (*1*), C300 (*2*), Z205 (*3*) in comparison with the system without an adsorbent (*4*).[193]

Estimates of the principal parameter determining the efficiency of MOFs as adsorbents, namely, the volumetric specific capacity of MOF-based methane storage systems, as a function of pressure at a temperature of 303 K are depicted in Fig. 24.

It is evident that packing of an ANG system with any of these MOFs increases the amount of methane stored at pressures below ~13–15 MPa (A250 and Z205) and below 22 MPa (C300). At higher pressures, the adsorption isotherms tend to saturation and adsorption activity does not make up for the effect of gas displacement.[193]

The pressure dependences of the absolute adsorption storage efficiency defined as the difference between the volumetric specific capacity of a storage system with (V_f) and without (V_g) an adsorbent at various temperatures for the Al-BTC-based storage system are presented in Fig. 25.

The pressure dependences of the absolute adsorption efficiency of ANG systems with MOFs pass through a maximum at ~5 MPa (as an example, see Fig. 25), which reveals the pressure range in which these MOFs can act as efficient methane adsorbents at various temperatures. It is clear that with increasing temperature, the methane uptake

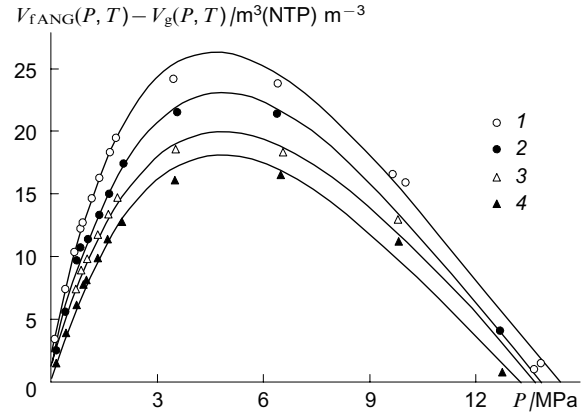


Figure 25. Total adsorption efficiency of adsorption storage of methane in Al-BTC at temperatures of 303 (*1*), 313 (*2*), 323 (*3*), 333 K (*4*).[193]

decreases. This should be taken into account in the development of operating conditions of ANG systems.

Analysis of variation of the volumetric capacity of a methane storage system with the given MOFs as a function of packing density demonstrated that in the 3.5–20 MPa pressure range, the highest volumetric specific capacity for methane storage is inherent in C300, which has a rather large micropore volume and high packing density (see Table 7). The volumetric specific capacities for methane storage of industrial Z205 and A520 samples and laboratory Al-BTC sample are approximately equal at pressures below 20 MPa, although the specific surface areas and pore volumes of these MOFs differ. If the packing density of adsorbents is increased by processing techniques, the volumetric specific capacity for methane storage can considerably increase. Thus, the performance of MOFs as methane adsorbents is determined by parameters of the pore structure (specific surface area and pore volume and size) and by the density of the framework.

We will make an attempt to elucidate the general patterns of methane adsorption in MOFs by considering the structure–property relationships and by analyzing data on methane adsorption obtained by different research groups,[199–254] depending on the MOF pore structure parameters and crystal density.

According to the data in Table 8, the specific surface area of MOFs with different pore structures can reach 7000 $m^2\ g^{-1}$. However, as shown by analysis (the results of which are depicted in Fig. 26), a very large surface area of the adsorbent is not a necessary condition for attaining high methane uptakes.

Indeed, at a pressure of 3.5 MPa, a temperature of 298 K and $a_s(BET) \leqslant 1500\ m^2\ g^{-1}$, the total volumetric capacity for methane storage increases with increasing MOF specific surface area and reaches the highest values of 226–228 $m^3(STP)\ m^{-3}$ for HKUST-1, Ni-MOF-74 and MAF-38 in the range of $1350 \leqslant a_s(BET) \leqslant 2000\ m^2\ g^{-1}$. The range of specific surface areas of MOFs in which the total capacity for methane storage reaches 80% of the DOE requirement of 2012 for a monolithic crystal ($V_f \geqslant 0.8\ V_f^{DOE}$) is $1400 \leqslant a_s(BET) \leqslant 2800\ m^2\ g^{-1}$. These data, at least the upper limit of the optimal range of a_s(BET) for efficient MOFs, do not contradict the estimates made by screening and computer simulation.[169, 171] It was noted above that Ni-MOF-74 (0.8 and 1.1 nm pore size) has a high concentration of OMS, which act as primary methane adsorption sites.[85, 185, 186] It was reported[85, 186] that high V_f values for HKUST-1 are due to the equivalence of adsorption sites formed by both OMS (Cu^{2+}) and oxygen atoms of each of the four windows of the octahedral lattice (see Figs 9, 19, Table 8).

A further increase in a_s(BET) is accompanied by a gradual decrease in the volume of adsorbed methane. According to the theory of adsorption in micropores,[92] the adsorbed amount is determined by two factors: the first one is related to the pore space accessible for gas molecules and the second one is associated with the adsorption energy, which is determined by the size of pores and interactions between the gas molecules and the framework ($E_0 = 24/X_0$, where E_0 is the standard characteristic energy of adsorption).[92] An increase in the specific surface area of MOF pores is accompanied by:

— an increase in the MOF pore volume and size; for example, in MOF-210 $[Zn_4O(BTE)_{4/3}(BPDC)]$,[205] the porous system is formed by three types of cages with the greatest voids of 2.7×4.8 nm (the fraction of voids in the framework is ~89%); however, on going to meso- and macropores, the degree of filling of the pore volume with methane decreases, that is, the methane volumetric density decreases;

— a decrease in the framework density, *i.e.*, the density of MOF adsorption sites, and finally weakening of the adsorption force field in the MOF pore space, which is consistent with calculations of Snurr's group[170] (see Fig. 17).

At a certain ratio of the porosity to energy factors, the highest volumetric density is attained; this is the case for methane adsorption in the pores of the most efficient adsorbents Ni-MOF-74 and HKUST-1 (see Fig. 8, Table 8).

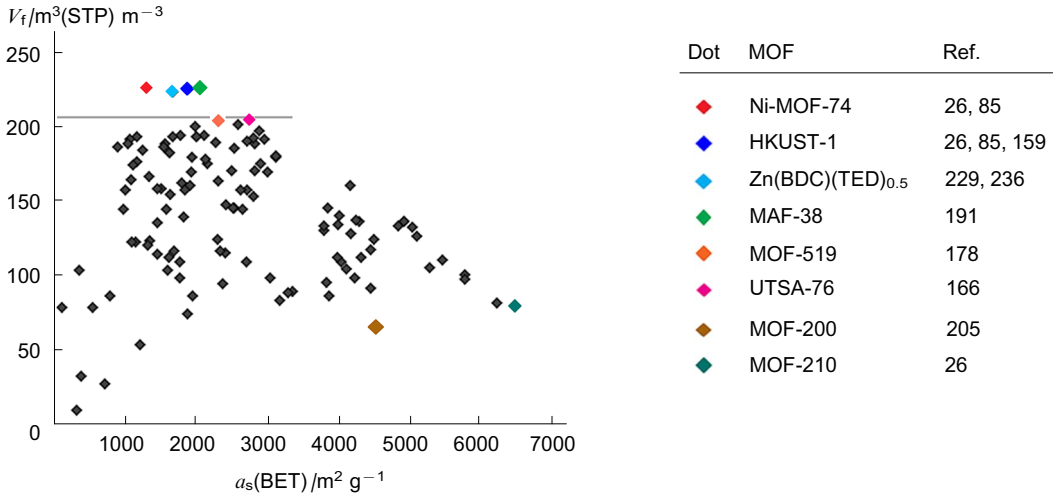


Figure 26. Array of experimental data for MOFs presented in Table 8 (P = 3.5 MPa, T = 298 K) characterizing the correlation between V_f and a_s(BET). The grey line marks the 80% level of the DOE target of 2012 for a monolithic MOF crystal. The dots described in the notation correspond to MOFs discussed in the text.

Table 8. Total and deliverable adsorption capacity for methane of MOFs with different pore structure parameters.

MOF	d_{cr} /g cm^{-3}	W_0 /cm^3 g^{-1}	a_s(BET) /m^2 g^{-1}	3.5 MPa, 298 K		6.5 MPa, 298 K		Q_{st} /kJ mol^{-1}	Ref.
				V_f /m^3(STP) m^{-3}	V_d /m^3(STP) m^{-3}	V_f /m^3(STP) m^{-3}	V_d /m^3(STP) m^{-3}		
MOF-519	0.953	0.938	2400	200	259	150	210	14.6	178
Al-soc-MOF-1	0.34	2.3	5585	122	197	101	176	11	200
MOF-210	0.25	3.6	6240	83	71	143	131	–	26
DUT-49	0.31	2.91	5476	112	92	176	156	–	201
SNU-70	0.41	2.17	5290	107	91	–	–	9.4	202
PCN-68	0.38	2.13	5109	128	98	187	157	–	203
NU-111	0.41	2.09	4930	138	111	206	179	15.2	162
DUT-23(Co)	0.40	2.03	4850	135	112	197	174	–	204
MOF-200	0.22	3.59	4530	67	56	117	106	–	205
MOF-177	0.43	1.89	4500	126	108	193	175	–	205
MOF-205	0.38	2.16	4460	119	100	183	164	–	205
IRMOF-8	0.45	1.83	4326	114	71	–	–	–	206
NU-140	0.43	1.97	4300	138	108	200	170	14	207
FJI-H5	0.46	1.92	4255	139	106	199	166	10.8	208
NOTT-119	0.36	2.35	4118	106	86	154	134	–	209
FJI-1	0.41	1.43	4043	111	90	164	143	–	210
ZJU-36	0.50	1.60	4014	142	114	203	175	–	211
PCN-66	0.45	1.63	4000	136	101	187	152	–	203
PCN-69	0.36	2.17	3989	114	94	–	–	–	203
MIL-101(Cr)	0.45	1.57	3870	88	68	130	110	–	160
PCN-80	0.57	1.47	3850	147	117	196	166	–	212
ZJU-32	0.43	1.48	3831	97	77	140	120	14.6	213
Cu_3(TATB)	0.42	1.91	3360	91	–	–	–	–	214
NOTT-102	0.59	1.27	3342	181	136	237	192	16	192
Cu_3(BTB)	0.41	1.77	3288	90	–	–	–	–	214
UTSA-28a-Cu	0.50	1.33	3179	85	65	–	–	16.9	215
NU-125	0.58	1.29	3120	181	133	228	180	15.5	163
NJU-Bai-12	0.52	1.14	3038	100	–	–	–	15.7	216
PCN-61	0.56	1.36	3000	171	127	219	174	–	212
NOTT-103	0.64	1.16	2958	193	140	236	183	15.9	192
ZJU-35	0.66	1.16	2899	177	132	227	182	–	211
NJU-Bai-9	0.668	1. 11	2883	199	107	–	–	14.9	166, 188
SDU-6	0.61	1.17	2826	172	127	–	–		217
ZJU-5	0.68	1.074	2823	190	130	228	168	15.3	218
NOTT-101	0.68	1.08	2805	188	138	239	183	15.5	192
IRMOF-6	0.65	1.18	3025	135	–	–	–	12.1	219
$[Zn_3(OH)]_4 \cdot (TBCPPM) \cdot (H_2TBCPPM)_2$	0.68	1.14	2718	192	146	275	230	–	220
SDU-7	0.61	1.10	2713	159	114	–	–	–	217
UiO(BPDC)	0.77	1.057	2646	146	–	–	–	15	221
NOTT-140	0.68	1.07	2620	159	–	–	–	16.6	222
DUT-8(Cu)	0.68	1.04	2535	147	112	188	153		223
NU-135	0.75	1.02	2530	187	127	230	170	16.6	224
SDU-8	0.63	1.02	2516	147	105	–	–	–	217
PCN-46	0.62	1.01	2500	172	132	206	166	–	225
HNUST-3	0.69	0.99	2412	149	–	–	–	15.4	226
MIL-100(Fe)	0.7	0.99	2410	117	92	158	133	–	227
HNUST-2	0.57	0.97	2366	96	–	–	–	15	226
DUT-51(Zr)	0.66	1.08	2335	118	87	161	130	–	228
$Ni(NDC)(TED)_{0.5}$	0.79	1.34	2307	165	129	–	–	13.8	229
SNU-50	0.65	1.08	2300	126	–	–	–	26.8	230
PCN-16	0.72	1.06	2273	191	134	–	–	–	175
$Zn_4O(L1)_2$	0.80	0.80	2151	177	117	213	153	11.3	231
ZJU-25	0.62	1.18	2124	180	132	229	181	15.1	232
NOTT-109	0.79	0.85	2110	196	125	242	170	17.1	192

Table 8 (continued).

MOF	d_{cr} /g cm^{-3}	W_0 /cm^3 g^{-1}	a_s(BET) /m^2 g^{-1}	3.5 MPa, 298 K		6.5 MPa, 298 K		Q_{st}	Ref.
				V_f /m^3(STP) m^{-3}	V_d /m^3(STP) m^{-3}	V_f /m^3(STP) m^{-3}	V_d /m^3(STP) m^{-3}	/kJ mol^{-1}	
PCN-14	0.83	0.83	1984	202	125	239	160	17.6	26
Cu-TDPAT	0.78	0.93	1938	181	122	222	163	–	233
PCN-11	0.749	0.91	1931	194	–	–	–	–	85
$Zn_4O(L1-CH_3)_2$	0.81	0.75	1908	162	110	196	144	11.8	231
$Li_3[(Cu_4Cl)_3(TTCA)$	0.70	0.72	1870	76	–	85	–	15.3	234
PMOF-3	0.88	0.72	1840	159	101	–	–	–	235
MIL-125(Ti)	0.81	0.67	1820	141	–	–	–	–	227
$Zn(BDC)(TED)_{0.5}$	0.89	0.73	1794	222	168	–	–	15.1	236–238
$Zn_4O(L1-Cl)_2$	0.84	0.71	1791	164	105	195	136	12.5	231
NOTT-107	0.76	0.77	1770	196	110	–	–	–	169
PCN-160	0.76	0.84	1760	111	70	–	–	–	175
$(Et_2NH_2)_3\cdot$ $\cdot[(Cu_4C_l)_3(TTCA)_8]$	0.74	0.64	1680	118	–	145	–	18.1	235
NOTT-100	0.93	0.68	1661	195	104	230	139	18.1	192
UTSA-40	0.83	0.65	1630	156	102	192	138	–	161
UTSA-20	0.91	0.63	1156	195	101	230	170	18.2	26, 161
DUT-5	0.63	0.81	1613	114	94	134	114	–	228
MTAF-4	0.67	0.65	1590	105	79	136	110	–	234
UiO-67(Zr)	0.71	0.69	1575	146	–	–	–	–	239
HKUST-1	0.88	0.71	1850	225	150	267	190	17.0	85, 159
Mg-MOF-74	0.91	0.63	1542	188	104	211	127	18.5	85
$Zn_2(BDC)_2(DABCO)$	0.83	0.68	1450	160	117	–	–	13.6	240
Ni-MOF-74	1.21	0.44	1027	230	115	251	142	20.6	85, 185, 186
DUT-4	0.77	0.68	1308	122	82	164	124	–	241
MIL-53(Al)	0.98	0.54	1235	186	–	–	–	17	242
$Ni_3L2(TPT)_2$	0.60		1206	71	–	–	–	21	243
MIL-53(Cu)	0.65		1150	191	–	–	–	–	244
NPC-5	0.82	0.50	1140	124	–	–	–	16.1	245
$Zn_4O(Fma)_3$	0.81		1120	98	–	–	–	12	246
Mn-MOF-74	1.08	0.50	1102	176	100	–	–	19.1	85, 185, 186
UTSA-38	0.96	0.61	1090	124		–	–	–	247
UiO-66(Zr)-NH_2	1.36	0.40	1080	166	100	204	138	–	227
CoMOF-74	1.17	0.48	1056	221	110	248	136	20.6	85
MIL-47(V)	0.50		1030	143	–	–	–	–	160
UTSA-34b	0.84	0.54	991	159	99	–	–	–	248
UiO-66(Zr)	1.32	0.36	970	146	–	–	–	–	227
Zn-MOF-74	1.23	0.41	885	188	102	–	–	18.3	85
SDU-1	0.83	0.35	779	88	–	–	–	17.6	249
SNU-30	0.38	0.28	704	29	–	–	–	–	230
Cd(BPYDB)	1.21	0.35	346	105	69	125	89	–	250
SNU-31	0.46	0.14	308	11	–	–	–	–	230
DUT-13	0.39	1.98	96	80	–	150	134	–	251
$Cu_4(L3)$	0.71	–	0.97	111	–	–	–	–	252
Co-MOF-74	1.17	0.51	–	221	110	249	136	19.5	85
MOF-5	0.62	1.4	3800	150	118	214	182	12.3	85
DUT-6	0.39	2.02	–	105	89	163	147	–	253
DUT-9	0.36	2.18	–	102	83	155	136	–	254
$Cu_4(H_4L3)$	0.93	0.47	–	79	–	–	–	–	252
MOF-519	0.953	0.94	2400	200	151	260	209	–	178
UTSA-76	0.699	1.092	2820	194	151	257	197	15.5	166, 255
UTSA-110	0.600	1.263	3241	–	190	241	–	14.5	168
LIFM-82 (Zr-MOF)	0.922	0.71	1624	196	143	246	193	17.5	174

Table 8 (continued).

MOF	d_{cr} /g cm^{-3}	W_0 /cm^3 g^{-1}	a_s(BET) /m^2 g^{-1}	3.5 MPa, 298 K		6.5 MPa, 298 K		Q_{st} /kJ mol^{-1}	Ref.
				V_f /m^3(STP) m^{-3}	V_d /m^3(STP) m^{-3}	V_f /m^3(STP) m^{-3}	V_d /m^3(STP) m^{-3}		
MAF-38	0.761	0.808	2022	226	150	263	187	21.6	191
ZJNU-53	0.655	1.084	3034	188	135	241	190	15.02	176
NJU-Bai-43	0.639	1.22	3090	202	146	254	198	14.45	167, 188
MFM-115a	0.611	1.38	3394	186	138	238	191	16.2	167
MFM-112a	0.503	1.62	3800	162	125	218	181	16.3	167
Co(BDP)	0.774	1.02	2911	163	155	205	197	15.0	177
ST-1	0.345	2.39	4412	105	–	160	149	–	189
ST-2	0.366	2.44	5172	120	–	180	–	9.2	189
ST-3	0.337	2.67	5660	108	–	170	152	–	189

Note. The following designations are used: d_{cr} is crystal density; W_0 is volume of micropores; soc is the square-octahedral topology; TATB is 5,5′,5″-[1,3,5-triazine-2,4,6-triyl-tris(1,4-benzamido)]triisophthalate; TBCPPM is tetrakis{3,5-bis[(4-carboxylato)phenyl]phenyl}methane, TED is triethylenediamine; TDPAT is 2,4,6-tris(3,5-dicarboxylatophenylamino)-1,3,5-triazine; TTCA is triphenylene-2,6,10-tricarboxylate; TPT is 2,4,6-tris(4-pyridyl)-1,3,5-triazine; Fma is fumaric acid; BPYDB is 4,4′-(4,4′-bipyridine-2,6-diyl)dibenzoate; L1 is 4-[*N*,*N*-bis(4-carboxylatophenylmethyl)amino]benzoate; L2 is 2,4,6-tris(3-carboxylatophenoxymethyl)mesitylene; L3 is 5,5′,5″,5‴-[1,2,4,5-benzenetetrakis(4-methyleneoxyphenylazo)]tetraisophthalate; FJI are MOFs synthesized at the Fujian Institute of Research on the Structure of Matter; HNUST are MOFs synthesized at the Hunan University of Science and Technology; MTAF are MOFs synthesized using a triazole-based organic ligand (metal triazolate framework); SNU are MOFs synthesized at the Seoul University.

When some relationship 'pore structure–adsorption properties' has been elucidated, it is necessary to find an equation that will reflect this relationship. Among the attempts to derive an equation of this type,[237, 256] mention should be made of the study of Li *et al.*,[54] who proposed an empirical equation relating the volumetric adsorption capacity of MOF for methane at definite temperature and pressure, methane density, pore volume and MOF crystal density

$$V_f d_{cr} = -\frac{p_1 W_t^2 + p_2 W_t - p_3}{p_4 W_t + p_5} \quad (4)$$

where the parameters $p_i > 0$ depend on thermodynamic conditions and on the methane density at the specified temperature and pressure. Figure 27 shows the results of calculation, according to Eqn (4), of methane volumetric capacities of MOFs at 6.5 MPa and 270 and 298 K plotted against the specific pore volume in comparison with experimental data for several MOFs (see Table 8).

Despite the deviations of experimental points from the theoretical curve, it can be seen that Eqn (4) reflects a correlation between the total volumetric capacity of MOFs for methane storage and the pore volume of the material. The efficiency of MOF as an adsorbent for methane can be considerably increased by decreasing the temperature to 270 K,[54] which is in line with conclusions made by other authors (*e.g.*, Refs 26 and 85).

It was noted above that methane deliverable capacity is a highly important characteristic of an ANG system. The experimental V_d values for MOFs corresponding to the pressure drop from 3.5 to 0.5 MPa at 298 K are shown in Fig. 28 depending on the specific surface area. It can be seen that the dependence of the methane deliverable capacity of

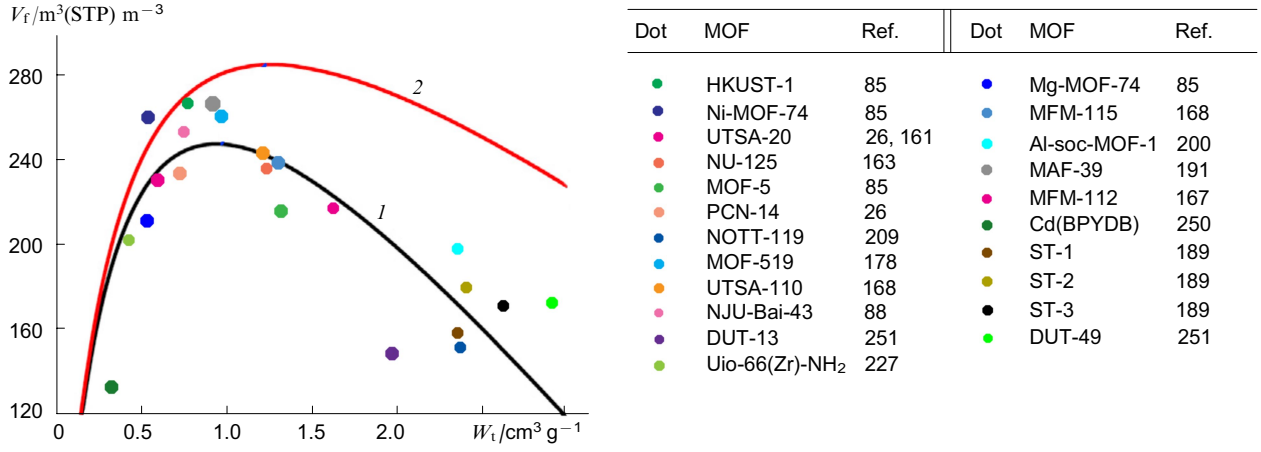


Figure 27. Specific total capacity of MOFs for methane *vs.* specific pore volume at 298 (*1*) and 270 K (*2*) calculated by empirical equation (4).[54] The dots correspond to experimental values for some MOFs.

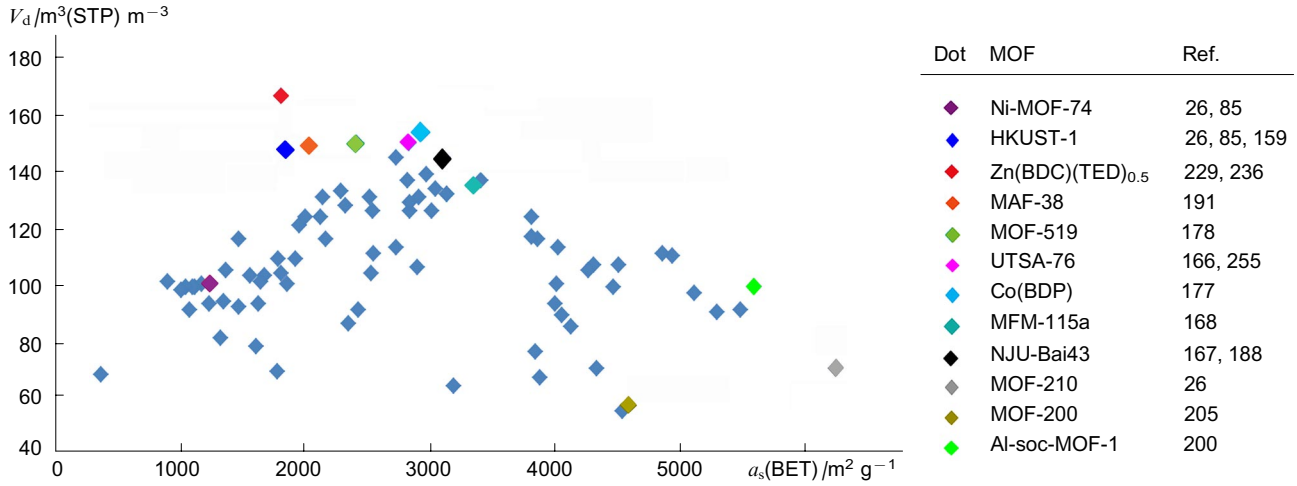


Figure 28. Array of experimental data for MOFs presented in Table 8 (P = 3.5 MPa, T = 298 K) characterizing the correlation between V_d and a_s(BET). The dots described in the notation correspond to MOFs discussed in the text.

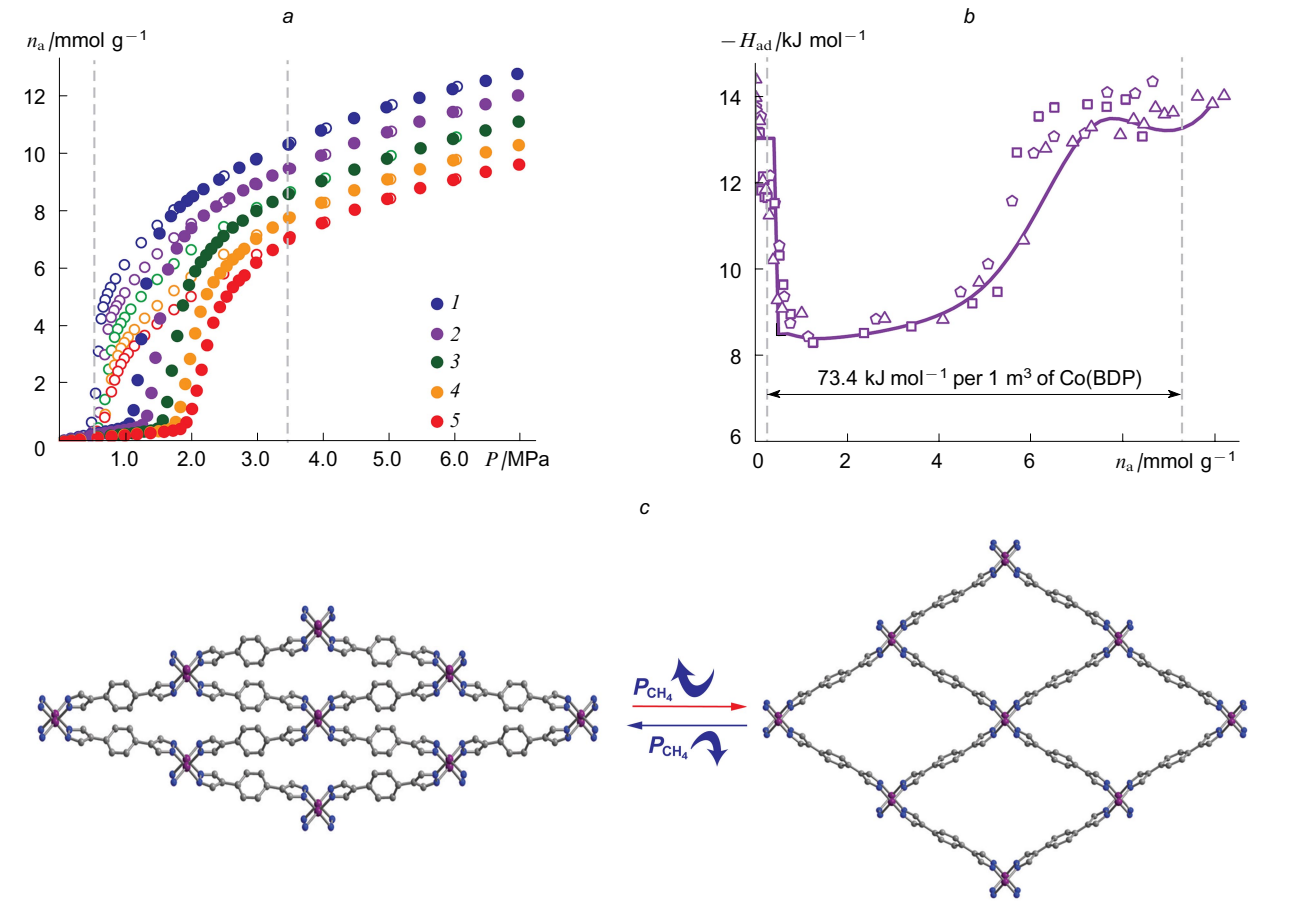


Figure 29. Isotherms of methane adsorption (colour-filled dots) and desorption (empty dots) in Co(BDP) at various temperatures (*a*), change in the enthalpy of methane adsorption with filling of the pore space of the framework (*b*) and framework transformation upon methane adsorption and desorption (*c*).
(*a*) T = 273 (*1*), 285 (*2*), 298 (*3*), 311 (*4*), 323 K (*5*); dashed lines mark the region corresponding to the minimum desorption pressure (0.5 MPa) and the maximum adsorption pressure (3.5 MPa); *b*: calculation from the isotherms (continuous line) and data of several calorimetric measurements (dots), the dashed lines confine the region of adsorption in the pressure range of 0.5–3.5 MPa. The Figure is adapted from Ref. 177.

MOFs on the specific surface area also reaches a maximum (at about 2000 $m^2\ g^{-1}$). The V_d values for adsorbents with equal total volumetric capacities for methane storage may considerably differ, depending on the amount of methane adsorbed at pressures up to 0.58 MPa (*e.g.*, Ni-MOF-74 and HKUST-1). The highest V_d values were obtained for MOFs with a regular porous structure and a pore size accommodating one to three methane molecules. For instance, the structure of pores of $Zn(BDC)(TED)_{0.5}$ representing channels with square cross-sections and characteristic size of 0.78 nm[236] is optimal for the adsorption of methane molecules. The equivalence of adsorption sites accounts for moderate methane uptakes in the initial pressure range and considerable uptakes at 3.5–4.0 MPa, which is optimal for high deliverable capacity values.

The S-shape of the methane adsorption isotherm for the non-rigid Co(BDP) structure with flexible BDP ligands (BDP is 1,4-benzenedipyrazolate) (Fig. 29 *a*) is caused by reversible endothermic phase transitions that result in framework expansion due to cleavage of π–π contacts between the neighbouring benzene rings of the ligand upon adsorption (see Fig. 29 *b*).[177] This shape of the isotherm is optimal for attaining high V_d. It is noteworthy that desorption of methane is accompanied by the collapse of the pore structure of Co(BDP) with heat evolution (see Fig. 29 *b*,*c*); as a result, the heat evolved upon methane adsorption in 1 m^3 of Co(BDP) is 33% lower than that of methane adsorption in HKUST-1.

A drawback of MOFs with flexible organic linkers is uncertainty of their configurations and possible decrease in the thermal stability.

Thus, to choose a metal-organic framework as a methane adsorbent, it is very important to consider its adsorption and desorption properties (see Figs 26 and 28). Considering large V_f and V_d values, HKUST-1, UTSA-76, MOF-519, MAF-38 and $Zn(BDC)(TED)_{0.5}$ are the most efficient adsorbents for methane in ANG systems.

The isosteric heat of adsorption, which reflects the change in the adsorbent temperature upon adsorption (desorption), is a key thermodynamic characteristic, which should obviously be taken into account for planning adsorption processes. The heat of adsorption is directly correlated with the binding energy between the adsorbed molecules and the adsorbent and with adsorbate–adsorbate interactions and also depends on the specific adsorption sites and average effective micropore size.

The correlation between the isosteric heats of methane adsorption and the volumetric density of the stored methane for MOFs is reflected in Fig. 30. Some publications (*e.g.* Refs 26, 85 and 148) indicate that for efficient operation of ANG systems (298 K, desorption in the 3.5–0.5 MPa range), the isosteric heat of adsorption should be ~17–18 kJ mol^{-1}. In Fig. 30, it can be seen that for most MOFs, the heat of methane adsorption is in the range from 14 to 22 kJ mol^{-1}, which corresponds to the values required for efficient methane adsorbents. A fairly high isosteric heat of methane adsorption is inherent in Ni-MOF-74, which is consistent with the mechanism of adsorption on open metal sites. Some researchers attempted to increase the adsorption capacity by incorporating alkali metal (*e.g.*, lithium) atoms into MOFs;[257–259] however, this gave no significant benefits.[259] In particular, it was shown that the replacement of $Et_2NH_2^+$ counter-ions in an anionic MOF by Li^+ cations decreases the methane adsorption capacity.[234] The highest Q_{st} = 26.7 kJ mol^{-1} among the given MOFs (see Table 8), which was found for SNU-50 $\{[Cu_2(BDCPPI)(DMF)_2 \cdot 10\,DMF] \cdot 2\,H_2O\}_n$ [BDCPPI is *N*,*N*′-bis(3,5-dicarboxylatophenyl)pyromellitic diimide] functionalized by bulky imide groups, is attributable to strong interaction of methane with framework molecules and narrow pores (channels with the maximum diameter of 0.45 nm);[230] meanwhile, the absorbed amount is moderate.

Low heats of adsorption are associated with a low concentration of specific adsorption sites (in particular, OMS) and relatively wide pores in the adsorbent, as noted, for example, by Batrakova *et al.*[195] Structures of this type possess relatively low total and deliverable volumetric capacities for methane storage, *i.e.*, they are of low utility for ANG technologies.

We will evaluate the efficiency of MOFs that are considered as potential methane adsorbents by analyzing the dependence $V_d = f(V_f)$ shown in Fig. 31. The straight line corresponds to $V_f = V_d$; dashed lines mark the relative efficiency values [see Eqn (2)], which makes it possible to compare the methane volume recovered from the system without an adsorbent upon pressure drop from 3.5 to 0.5

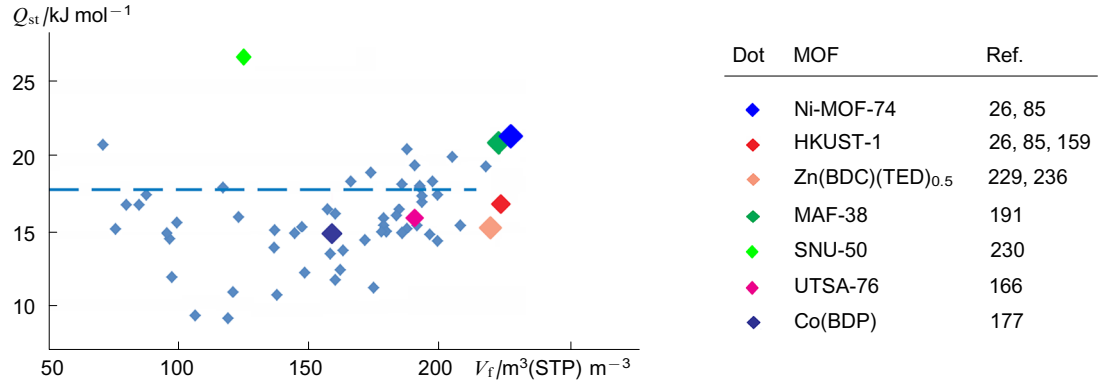


Figure 30. Array of experimental data for MOFs presented in Table 8 (P = 3.5 MPa, T = 298 K) characterizing the correlation between Q_{st} and V_f.
The dashed line marks the heat of adsorption (~18 kJ mol^{-1}) optimal for efficient operation of an ANG system with a MOF adsorbent. The dots described in the notation correspond to MOFs discussed in the text.

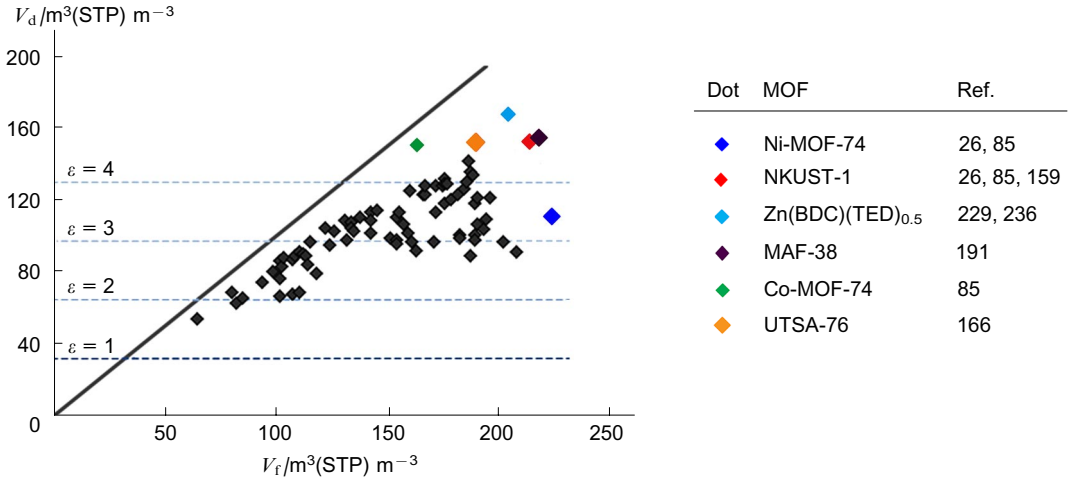


Figure 31. Array of experimental data for MOFs presented in Table 8 (P = 3.5 MPa, T = 298 K) characterizing the correlation between V_d and V_f.
The straight line corresponds to the condition $V_f = V_d$. The dashed lines designate the relative efficiency levels [see Eqn (2)] of methane storage (ε) in comparison with a CNG system at 298 K and 3.5 MPa. The dots described in the notation correspond to MOFs discussed in the text.

MPa with the rated methane volume stored in the system with an adsorbent in the same pressure range. It is clear that methane storage in MOF adsorption systems is 2–3 times more efficient than the gas-cylinder storage (under similar conditions); for the best samples of MOFs, it is more than 4 times more efficient.

Analysis of the data presented in Fig. 31 leads to an unambiguous conclusion that the methane deliverable capacity of MOFs, defined as the amount of methane delivered to the consumer upon desorption, is always lower than the total gas uptake: $V_d < V_f$. Nevertheless, the pattern of dependence of V_d on V_f shown in this Figure attests that the residual amount of methane in MOFs increases with increasing amount of adsorbed gas, which is definitely related to specific features of the adsorption mechanism. As a result, a part of methane (5%–25% of the adsorbed amount) is retained in the MOF-based ANG system at a pressure of 0.5 MPa. To recover this remaining methane, external energy supply is required. The flexible Co(BDP) structure exhibiting an S-shaped adsorption isotherm is an exception.

An important criterion of adsorbent efficiency for ANG systems is the relationship between the total volumetric and gravimetric (G_f) capacities for the adsorbed gas (Fig. 32 *a*). In view of the restricted weight of the adsorber (cylinder with the adsorbent), an optimal ratio of the volumetric to gravimetric capacities for the adsorbed methane is required, in particular, for a specified methane volumetric density, the microporous structure should possess the minimum weight. The relationship between the deliverable volumetric and gravimetric (G_d) capacities for some MOFs is depicted in Fig. 32 *b*. It can be seen that high values of the total and deliverable gravimetric capacities for methane are associated with extensive porosity, in particular, with rather high specific surface areas (see Table 8), as, for example, for Al-soc-MOF-1 (Ref. 200) and DUT-49 (Ref. 201) at

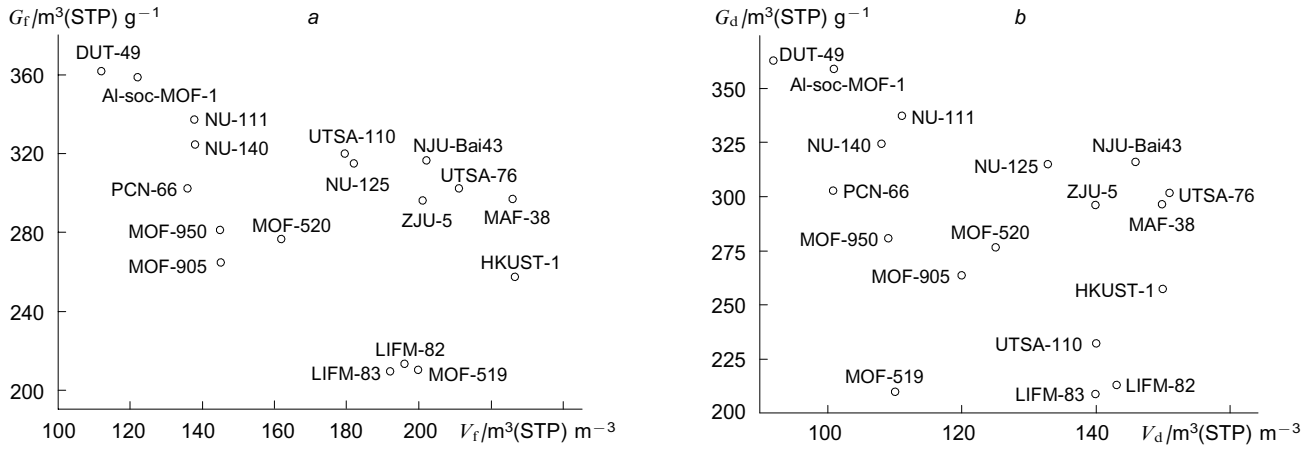


Figure 32. Relationship of total (*a*) and deliverable (*b*) volumetric and gravimetric capacities for methane of a number of MOFs at 3.5 MPa and 298 K. The Figure is based on Refs 26, 85, 162, 163 167, 168, 174, 181, 191, 200, 201, 203, 207, 218 and 255–260.

3.5 MPa and 298 K; the volumetric capacities of MOFs are largely determined by the nature and concentration of the adsorption sites.

It is worth noting that, according to rough estimates,[85] an increase in the deliverable gravimetric capacity for methane by 10% implies a decrease in the adsorbent weight (if HKUST is chosen as the adsorbent) in an ANG system by 19 kg, but the fuel economy (for example, an increase in the running distance of an ANG-operated vehicle) would be only 0.8%. Meanwhile, an increase in V_d by 10% with the adsorber volume remaining the same would provide a fuel economy of $\sim$10%.

The optimal adsorbent should maintain a balance between these characteristics, in order to attain a sufficiently high methane uptake and delivery volume at the lowest possible weight of the adsorbent packed into the ANG tank. In terms of the ratio of total and deliverable volumetric [m^3(STP) m^{-3}] and gravimetric [m^3(STP) g^{-1} or g g^{-1}] specific capacities, the optimal frameworks are HKUST-1,[26] MAF-38,[191] UTSA-76,[173,255] NJU-Bai-43 [167] and ZJU-5.[218] Upon pressure rise to 6.5 MPa at 298 K, the best relationship between these parameters was found for UTSA-110: 402 m^3(STP) g^{-1} and 241 m^3(STP) m^{-3} (Ref. 168).

Thus, analysis of the adsorption characteristics demonstrated that MOFs exhibit high methane storage performance regarding both the total (up to 220 m^3 m^{-3}) and deliverable (up to 170 m^3 m^{-3}) volumetric capacities. Most MOFs possess the optimal energy characteristics for the operation as adsorbents within ANG systems. Furthermore, MOFs were shown to have relatively high gravimetric storage characteristics (up to 0.25 g g^{-1}). This attests to good prospects for the use of these materials as adsorbents in ANG systems. However, as noted above, the target values of the methane total and deliverable capacities of MOFs at specified temperature and pressure have not yet been attained. In addition, despite the excellent methane adsorption properties, effective application of MOFs for the adsorption storage of natural gas in the near future would require solution of a number of problems associated with the physicochemical properties of these frameworks.

4. Composite materials based on metal-organic frameworks

It was noted above (see Section 2) that the scope of applicability of MOFs is markedly extended by using various functionalization methods both during and after the synthesis. Combinations of MOFs with some other materials (metal nanoparticles and oxides, polymers, enzymes, carbon nanotubes, *etc.*) may give composites with enhanced performance characteristics.[41–50]

Below we consider the preparation methods of MOF-based composites with better adsorption characteristics in more detail.

The effective use of microporous carbon adsorbents in ANG systems is determined by their physicochemical and mechanical properties: mechanical strength, hydrophobicity and high packing density. It is also important that the carbon surface is electrically neutral and adsorption is mainly due to dispersion forces.[12,13] In real ANG systems, the application of MOFs is limited due to their poor operating characteristics: low stability, hydrophilicity and susceptibility of the porous structure to degradation. This problem is solved by fabrication of composites that combine highly efficient but unstable MOFs and carbon materials possessing all of the above-listed benefits. Kayal and Chakraborty [41] described the synthesis of the MAX-MIL composite based on the high-performance carbon adsorbent, Maxsorb III, and the metal-organic framework, MIL-101(Cr); the composite was investigated for the structure and energy characteristics and morphology as well as methane adsorption characteristics.

The composite was prepared in the following way: $Cr(NO_3)_3 \cdot 9H_2O$, terephthalic acid and the Maxsorb-III activated carbon were mixed, HCl and water were added, and the mixture was kept in an autoclave for 12 h at 473 K; after the mixture was cooled, DMF was added in order to remove unreacted terephthalic acid from the pores. The resulting composite was activated in ethanol for 12 h at 353 K, separated and dried. It should be noted that the carbon adsorbent was considered as an ancillary binding agent ($\sim$1 mass %) and MOF was considered as the functional agent.

The MAX-MIL composite adsorbs more methane than the MIL-101(Cr) framework and the Maxsorb-III carbon adsorbent (Fig. 33). Enhanced operating characteristics were noted for the composite, in particular, pronounced hydrophobic properties, as opposed to hydrophilicity of the initial MOF. Thus, this preparation process of the composite material may become useful to make MOFs applicable for ANG systems.

The unique mechanical, electrical and thermophysical properties and high chemical stability of carbon allotropes such as graphene, fullerenes and carbon nanotubes (CNTs) [260] provide conditions for successful use of these materials in MOF composites.

As an example, consider the CNTs/MOF-5 composite obtained by mixing a dispersion of CNTs in DMF with a solution of MOF-5 precursors;[261] that is, the insertion of CNTs into the crystal lattice of MOF-5 takes place *in situ*. In order to accelerate the dissolution of CNTs and nucleation of MOFs, the carbon nanotubes were initially treated with an acid. It was found that the CNTs/MOF-5 composite had the same crystal structure and morphology as the

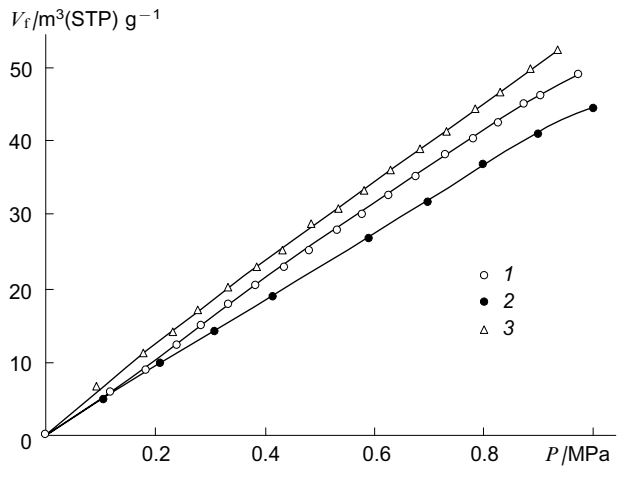


Figure 33. Total specific capacity of adsorption systems based on MIL-101(Cr) (*1*), Maxsorb-III adsorbent (*2*) and MAX-MIL composite (*3*) *vs.* pressure at 300 K.
The Figure is adapted from Ref. 41.

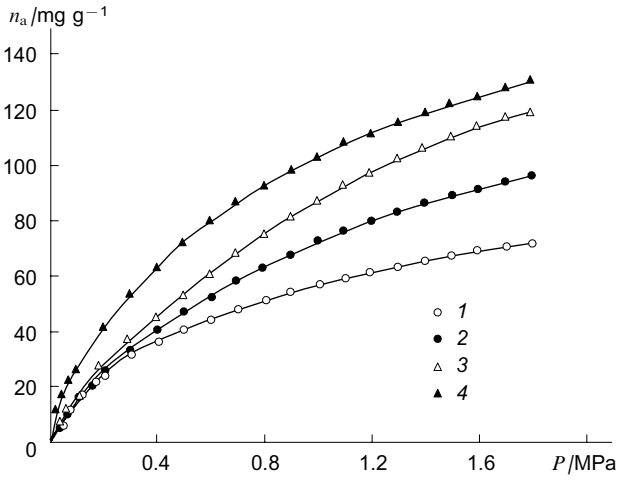


Figure 34. Isotherms of methane adsorption in the pores of HKUST-1 (*1*), Li^+@HKUST-1 (*2*), MCNTs@HKUST-1 (*3*), MCNTs–Li^+@ HKUST-1 (*4*) at 298 K.
Adsorption and desorption data coincide. The Figure is adapted from Ref. 262.

starting MOF-5; the transmission electron microscopy data confirmed the presence of multiwalled CNTs (MWCNTs). The last-mentioned fact was responsible for composite stability, in particular, stability to electron beam irradiation and to atmospheric moisture. Furthermore, the specific surface area increased from 2160 to 3550 $m^2\ g^{-1}$ and the fraction of ultramicropores ($X_0 < 0.7$ nm) increased; besides, stability of the MOF-5 structure was noted.[261]

The HKUST-1 metal-organic framework has a high adsorption activity towards methane (see Section 2), but low mechanical stability. This precludes consideration of this material as an efficient adsorbent for ANG systems. However, as shown by Xiang *et al.*,[262] the lithium cation-doped MCNTs@HKUST-1 composite fabricated by synthesizing the MOF on the carboxylated surface of acid-pretreated MCNTs with subsequent introduction of Li^+ ions is stable and possesses a higher (by 200%) methane uptake than initial HKUST-1 (Fig. 34). The incorporation of either lithium ions or CNTs into the HKUST-1 framework also resulted in higher methane uptake, but the increase was not so pronounced as for the CNTs–Li^+@HKUST-1 composite.

Although incorporation of Li^+ ions and CNTs into the framework resulted in a considerable decrease in a_s(BET) of the composite, the pore volume barely changed. The authors attributed the increase in the methane adsorption capacity to the presence of ultramicropores at the CNTs–Li^+/HKUST-1 interface separating the two lattices in the composite and to the affinity of lithium ions towards gas molecules.

4.1. Shaped composite materials based on metal-organic frameworks

The use of MOFs in the natural gas storage systems implies that they meet the requirements imposed on such systems, in particular:

— high chemical stability, since natural gas contains (although in minor amounts) corrosive compounds such as H_2O, H_2S and CO_2;

— minimized affinity to heavier natural gas components (ethane, propane and butane), which can irreversibly fill the MOF pores;

— thermal stability and thermal conductivity, as the adsorption (desorption) processes are accompanied by heat release (absorption);

— ability to provide a high gas flow rate to rapidly fill the adsorber and deliver the gas to the consumer;

— mechanical strength needed for densification of MOFs in order to achieve the highest volumetric capacity of the ANG system;

— accessibility and simplicity of the synthesis, low cost of reactants and the final product.

In addition, it is important to minimize the pressure differences within the adsorbent bed loaded into the tank of the ANG system.

These properties formed the basis for the development of production processes for shaped MOF-based materials with enhanced performance (pellets,[263–267] monoliths,[268–272] hollow fibres[273] and foams[274,275]). Several procedures were developed for agglomeration of MOF crystals directly during the synthesis[35,127] or by introducing them into substrate of a particular shape, *e.g.*, by filling the pores of a porous silica monolith with a MOF powder.[52,276]

Currently, two approaches to MOF shaping are known. The first approach implies the use of a substrate: MOF layers are deposited on the substrate[277] or MOF films are formed *via* cathode deposition (electrochemical synthesis).[127] Falcaro *et al.*[49] described techniques that allow exact positioning and fixing of MOFs on various substrates including fabrics[277] and polymer fibres.[278,279]

The second approach implies MOF processing *via* extrusion, granulation, templating, uniaxial pressing, pulsed current treatment or foaming.[280–293] Virtually any process related to pressing or extrusion involves the use of a plasticizer (water or a mixture of water with an organic solvent) to decrease the viscosity of the slurry. After extrusion, the plasticizer is removed by heating or vacuum thermal treatment. A binding agent is used to increase the cohesive properties and mechanical stability of the shaped MOFs.

Among publications devoted to various methods for shaping of MOFs to be used as adsorbents, mention should be made of several reviews.[35,264,274,277,280] The data presented in these reviews and in some original papers[281–293] are summarized in Table 9. Note that the method chosen for shaping depends on the MOF synthesis, properties and potential applications.

Since this review is devoted to the application of MOFs as adsorbents in ANG systems, we will consider shaping methods directed towards increasing packing density of MOFs formed as granules or pellets in comparison with the packing density of powders, in particular, extrusion, pressing and granulation. The possibility to prepare MOF monoliths on a substrate by the sol–gel method are also considered.

Analysis of the properties and crystal structure of shaped MOFs showed their advantages over the initial powders, consisting in higher mechanical strength, thermal conductivity, moisture resistance, packing density and chemical resistance. However, most of methods related to densification of MOF powders result in decreasing crystallinity and porosity of shaped materials.[35,264,282–294] For example, Bazer-Bachi *et al.*[295] noted that pelletizing of

Table 9. Methods of shaping of metal-organic frameworks.

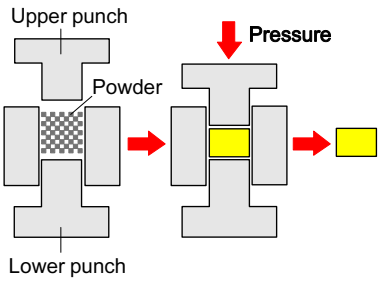
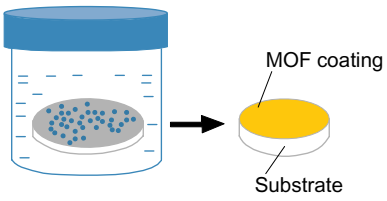
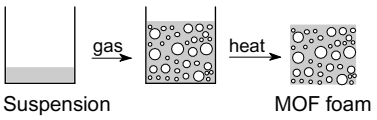
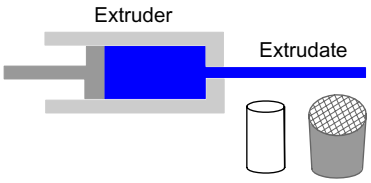
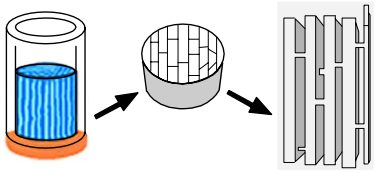
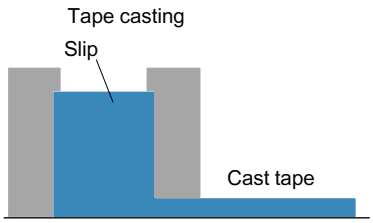
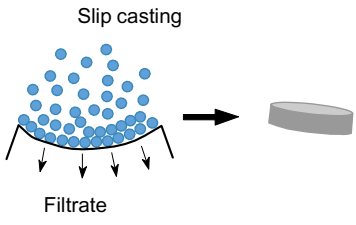
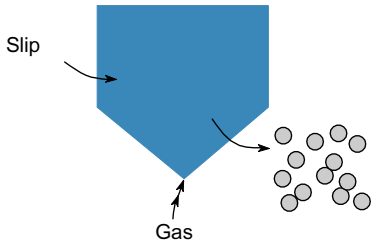
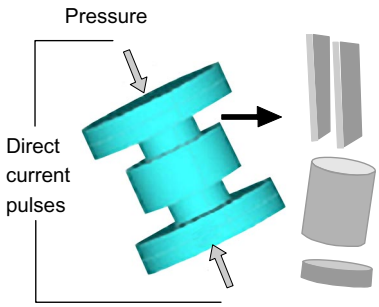
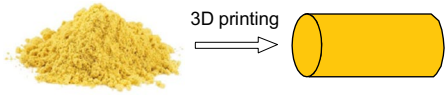
Scheme	Description	Productivity	Ref.
	*Uniaxial pressing* Mixing of the active MOF component with a binder (water + ethanol/methanol) and pressing into moulds. Pressing without a binder is possible	Low	282 – 284
	*Coating* MOF deposition as a coating on a chosen substrate. In particular, honeycomb cordierite can be used as the substrate	Medium	127, 269, 270, 274, 285, 286
	*Foaming* Incorporation of a gas into a particulate MOF suspension and drying to give a foam. Polyurethane or nickel foam are used as binders	High	274, 275, 287
	*Extrusion* Extrusion of a mixture of MOF precursors (without a solvent, in a melt, with a minor amount of methanol) and cutting into desired lengths	High; product yield per unit volume in unit time, kg m^{-3} per day: Al(OH)-fumarate, 27 000; HKUST-1, 144 000; ZIF-8, 144 000	288, 289
	*Templating* Solid or emulsion templates are used to form desired shapes and ordered morphology	Low	289
	*Casting* Casting a slurry of MOF mixed with a binder (*e.g.*, a chitosan solution) on a substrate	Medium	274, 290
	Casting a slurry of MOF mixed with a binder (*e.g.*, a chitosan solution) on a substrate	Medium	274, 290

Table 9 (continued).

Scheme	Description	Productivity	Ref.
	Granulation		
	Granulation of a mixture of the active MOF component with a binder (PVA, polysaccharides, mesoporous alumina) to form pellets	High	264, 292
	Pulsed current processing		
	MOF powders are subjected to pulsed electrical current and pressed	Medium	293
	3D printing		
	MOF powders are mixed with binders (bentonitic clay, PVA) and printed into desired shapes	Low	271

HKUST-1 at pressures above 80 MPa decreased the specific surface area by 50%.

In some cases, the loss of MOF porosity is induced by the incorporation of a binding agent into the solution before shaping. Indeed, inorganic binders, for example, graphite,[296] ensure hardness of MOF pellets after annealing above 700 K. Organic compounds such as cellulose esters[265, 274,] or, most often, poly(vinyl alcohol) (PVA)[297] are also used. The review of Rubio-Martinez *et al.*[35] notes insufficient number of systematic studies of the effect of the binder nature and concentration in the processed mixture on the specific surface area and other MOF parameters.

For determination of the optimal binder, HKUST-1 was shaped using various compounds: a 5% solution of PVA, a 2% solution of chitosan in 2% acetic acid or a 0.1% solution of oxycellulose and latex. After that, the density, strength and changes in the pore structure parameters of MOFs were determined.[297]

According to the results summarized in Table 10, the lowest strength is inherent in the sample shaped upon the addition of a 0.1% solution of oxycellulose (sample *2*); in this case, the a_s(BET) value decreased by 35% compared with that of the initial MOF. The use of a 2% solution of chitosan in 2% acetic acid affords stronger pellets; however, a_s(BET) decreases by 43% (sample *1*). After the addition of *N*,*N*-dimethylformamide (the solvent used in the synthesis of Cu-BTC), the pore structure of the initial Cu-BTC was retained, but the strength of the resulting adsorbent decreased (sample *3*). The composite shaped with addition of latex as a binding agent into the mixture proved to be insufficiently strong (sample *5*). A 5% solution of PVA was most appropriate for the Cu-BTC-based composite adsorbents when taken in 1 : 1 ratio by mass with the MOF; the introduction of this agent provided sufficient strength of the shaped material with retention of the porosity (sample *4*).

Agueda and co-workers[263, 298] produced extrudates of the UTSA-16 metal-organic framework

Table 10. Properties of samples shaped using various binders and changes in their pore structure parameters [Δa_s(BET), ΔW_0] in comparison with parameters of the initial Cu-BTC powder (HKUST-1).[297]

Sample	Binder content (%) (see [a])	d_p /g cm^{-3}	Δa_s(BET) (%)	ΔW_0 (%)	Strength /kg mm^{-2}
1	2% chitosan solution (1 : 1)	1.33	43	0	0.50
2	0.1% oxycellulose solution (1 : 1)	1.28	35	38	The sample collapsed
3	2% chitosan solution (1 : 1) + 1 ml of DMF	1.16	4	3	0.57
4	5% of PVA (1 : 1)	1.18	0	0	2.26
5	10 mass % of latex + 1 ml of water (80%) (9 : 1)	1.16	28	30	The sample collapsed

[a] The value in parentheses is the mass ratio of MOF to the binder solution.

{$K(H_2O)_2Co_3(cit)(Hcit)$], where cit is the fully dehydroxylated citrate ion (4−), Hcit is the citrate-ion (3−)}, which is an efficient hydrogen, carbon dioxide and methane adsorbent (the uptake is 2.5 mol kg^{-1} at 298 K), also using PVA and using a propanol–water mixture as a plasticizer. Since the chosen binder chemically resembles the solvent (ethanol) employed for the synthesis of UTSA-16, considerable changes of the MOF structure were avoided. The strength and density of the resulting UTSA-16 pellets of size 1 to 5 μm proved to be comparable with the corresponding characteristics for the commercial zeolite pellets containing 2% PVA. Variation of the PVA content from 0% to 6.66% demonstrated that the decrease in the specific surface area of UTSA-16 was, in some cases, proportional to the binder concentration and depended on the MOF activation temperature (Fig. 35). High activation temperatures (393 K) resulted in minimized Δa_s(BET) for the binder contents being equal: if $w_{PVA} < 2\%$, the loss of the specific surface area for the UTSA-16 extrudates was negligible; after addition of 3% PVA, the Δa_s(BET) value was $< 5\%$.[263] The results demonstrated that activation of extruded UTSA-16 pellets can be conducted at temperatures up to 423 K without damaging the MOF crystal structure.[263, 298]

Chen *et al.*[274] obtained pellets and foams by freeze-drying of HKUST-1 and Fe_3O_4 mixtures. Carboxymethylcellulose was used as the binding agent. It was suggested that other polysaccharides are also applicable.

Indeed, the use of sucrose to prepare spherical pellets of the Zr-BDC-based composite[264] in a centrifugal granulator resulted in high-strength pellets 0.5–15 mm in diameter. The sieved mixture of a Zr-BDC and a ground sucrose powder was loaded into the working chamber of the granulator in which the centrifugal force and water spraying afforded spherical pellets, the diameter of which could be controlled by varying the process duration. The pellets were dried for 24 h at 60 °C. The powder X-ray diffraction data for the powders and shaped Zr-BDC samples showed that the crystal structure remained intact after the centrifugal granulation. The optimal content of the sucrose in the composite (10%) gave Zr-BDC pellets with a better relationship between the hydrogen storage capacity and deterioration of structural characteristics. The shaping of MOFs by means of a centrifugal granulator proved to be more efficient than mechanical pressing. The preparation of 1 kg of Zr-BDC pellets required 30 min.

Finsy *et al.*[267] used PVA as the binding agent to granulate MIL-53(Al). The pellets of the MIL-53(Al) composite with PVA remained stable on heating above 300 K and at a pressure up to 0.8 MPa. However, analysis of nitrogen adsorption isotherms showed a loss of the total adsorption capacity upon the use of PVA as a binding agent: in comparison with the initial crystalline MIL-53(Al) powder, the micropore volume in the pellets of the PVA-containing (13 mass %) composite decreased by 32% (from 0.495 to 0.335 $cm^3\ g^{-1}$); however, the pore size barely changed (0.48 and 0.51 nm for the initial MOF and the PVA composite, respectively). The decrease in the pore volume for the PVA composite was also dependent on the activation temperature: after activation at 240 °C, only 11% of the initial pore volume of MIL-53(Al) proved to be accessible for the adsorption of molecules. The loss of porosity in the MIL-53(Al)/PVA composite activated at temperatures above 473 K was attributed to melting of PVA; the part of the alcohol that passed to the liquid phase formed a surface layer on the MIL-53(Al) crystals, thus preventing access to the pores.

Blanita and co-workers[283, 284] used manual compression of the MIL-101(Cr) powder to obtain hexagonal pellets with densities of 0.20 and 0.19 g cm^{-3} (Fig. 36). When adsorbers are filled with natural gas, this shape of adsorbent pellets provides the optimal packing density.[12]

The compression method used by the authors[284] increased the envelope density of MIL-101(Cr) pellets by a factor of 1.7–2.5, with the skeleton density (a ~7% decrease) and porosity being virtually retained [Δa_s(BET) = 10%–15%, ΔW_0 = 11%]. Only a minor decrease in the H_2 uptake (8%) was found for MIL-101(Cr), although the data of IR spectroscopy indicated a change in the coordination environment of the metal adsorption sites. The authors emphasized that the MIL-101(Cr) pellets were stable to mechanical and heat treatment and suitable for adsorber application.

Rezaei *et al.*[269] reported the preparation of structured monolithic composites based on UTSA-16 and Ni-MOF-74 as polycrystalline films supported on cordierite, which possesses a honeycomb structure; the MOF crystals were grown by the bottom-up method. The resulting monolithic

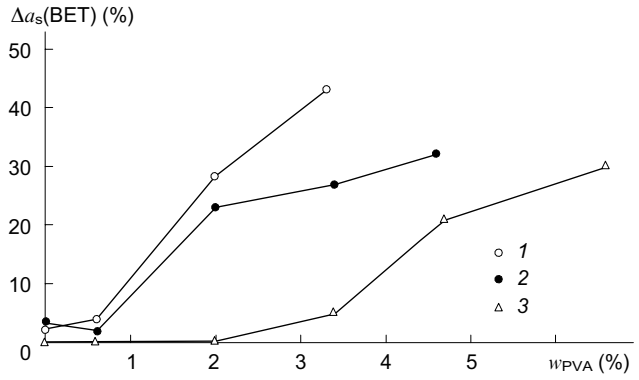


Figure 35. Loss of the specific surface area of the UTSA-16-based composite [a_s(BET)] *vs.* concentration of the PVA binder (w_{PVA}) at activation temperatures of 359 (*1*), 373 (*2*) and 393 K.
The Figure is adapted from Ref. 263.

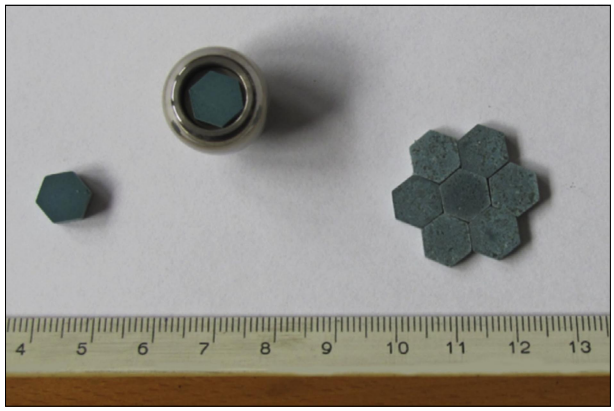


Figure 36. Hexagonal monolithic pellets of MIL-101(Cr) and a variant of their packing.
The Figure is adapted from Ref. 284.

coatings had relatively low a_s(BET) [652 $m^2\ g^{-1}$ for Ni-MOF-74 and 223 $m^2\ g^{-1}$ for UTSA-16(Co)], which had an effect on their adsorption properties. The CO_2 uptake of powdered Ni-MOF-74 was 6.54 mmol g^{-1}, that for the Ni-MOF-74–cordierite monolith was 1.7 mmol g^{-1}. The CO_2 uptake of the UTSA-16 monolith was 1.1 mmol g^{-1}.

Analogous monolithic polycrystalline MMEN-Mg_2(DOBPDC) films (MMEN is *N*,*N*′- dimethylethylenediamine, DOBPDC is 4,4′-dioxidobiphenyl-3,3′-dicarboxylate) were grown on a pretreated cordierite support using MgO nanoparticles as precursors.[270] The resulting composite adsorbent showed high carbon dioxide uptakes for adsorption from a mixture with helium (10% CO_2) or from 100% CO_2: 2.37 and 2.88 mmol g^{-1}, respectively.

The 3D printing technology is also used for MOF shaping. In 2017, Thakkar *et al.* reported[271] the fabrication of Ni-MOF-74 and UTSA-16(Co) monoliths with MOF contents of up to 80 mass % and 85 mass %, respectively, by 3D printing (Fig. 37). Measurements of CO_2 adsorption demonstrated that the Ni-MOF-74 and UTSA-16(Co) monoliths retain 79% and 87% of the adsorption capacity of their powdered analogues under the same conditions. The resulting three-dimensional printed monolithic structures with relatively fast adsorption kinetics demonstrated stable performance as adsorbents. These results point out a new potential of 3D printing technology for manufacture of MOFs with different shapes to be used in gas storage systems.

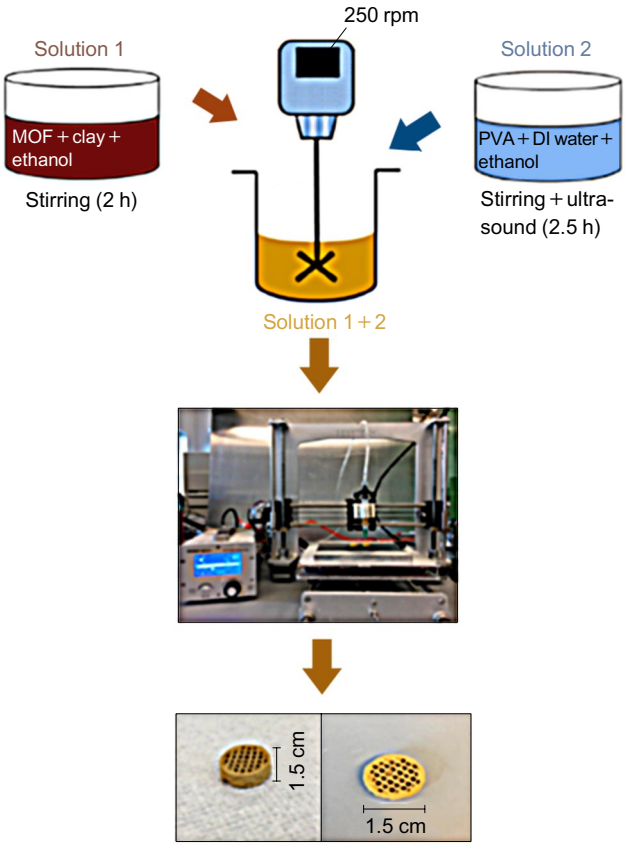


Figure 37. Flow chart of the preparation of MOF monoliths using 3D printing technology.[271]
DI stands for deionized.

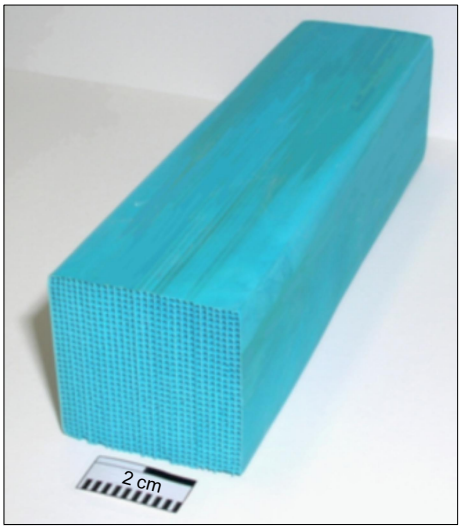


Figure 38. Photograph of the extruded HKUST-1 monolith.[288]

Two-stage extrusion was used to manufacture the first monolith of the HKUST-1 framework,[288] which is, as shown above, is a highly efficient methane adsorbent. First, a crystalline powder of HKUST-1 was mixed with silicone resin and a plasticizer (methylhydroxypropylcellulose, Culmial MHPC 20 000 P) to form a paste, which was pushed through an extruder. The monoliths thus formed had a high mechanical strength (up to 320 N), but the loss of specific surface area was substantial (70%), which was attributed to filling of some of the pores with binder molecules. However, the performance characteristics of the extruded sample were markedly superior over those of the sample grown *in situ* on a cordierite substrate. The monolith image shown in Fig. 38 is presented in many reviews (*e.g.*, Ref. 35) as a successful example of manufacture of a monolithic MOF sample.

4.2. Effect of shaping conditions on the adsorption properties of metal-organic frameworks

The data given in the previous Section indicate that shaping is most often accompanied by the loss or collapse of the pore structure of the initial MOF, which directly affects its adsorption characteristics. For increasing the adsorbent packing density in order to maximize the volumetric adsorption capacity for methane, MOF powders should be compressed. Furthermore, it is necessary to elucidate the optimal pressing conditions in order to retain (or increase) the porosity and, hence, the adsorption capacity of MOFs.

Jia *et al.*[299] investigated the effect of pressure on the structure, porosity and methane uptake for one of the most popular frameworks, MOF-5.[79] Densification under pressures of 0.5, 1.0 and 2.0 MPa increased the packing density of MOF-5 powder from 0.2569 to 0.3151, 0.4612 and 0.4890 g cm^{-3}, respectively. Analysis of methane adsorption isotherms for MOF-5 powder activated under solvothermal conditions and for pressed MOF-5 samples demonstrated the highest methane volumetric uptake at 3.5 MPa, equal to 81 m^3(STP) m^{-3}, for the sample pressed under 1.0 MPa (Fig. 39). This value exceeded the adsorp-

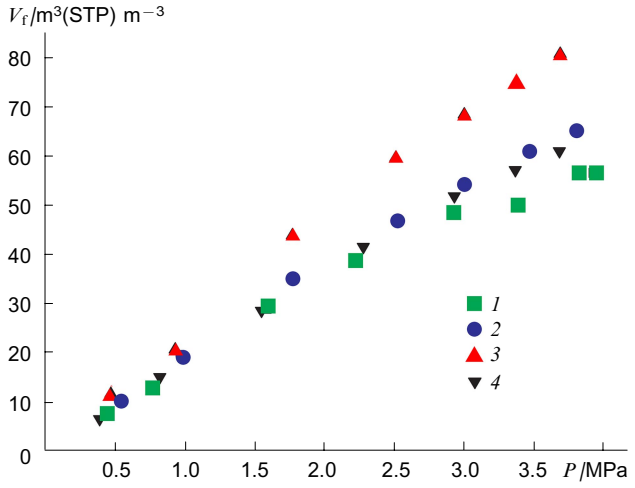


Figure 39. Isotherms (T = 300 K) for methane adsorption with the initial MOF-5 powder (*1*) and with MOF-5 pressed at 0.5 (*2*), 1.0 (*3*) and 2.0 (*4*) MPa at 300 K.[299]

tion capacity of the initial powder calculated with packing rather than crystal density. Pressing under 0.5 and 1.0 MPa decreased only slightly the concentration of adsorption sites in MOF-5; however, in the sample pressed at 2.0 MPa, the concentration of adsorption sites decreased twofold and the specific surface area and pore volume also decreased. The 0.5 MPa pressure proved to be insufficient for densification of the MOF-5 powder to increase the packing density to the optimal value providing the greatest methane uptake.

Tagliabue *et al.*[300] investigated the effect of shaping on the methane adsorption characteristics of the CPO-27-Ni metal-organic framework compressed into pellets without a binder at 0.1 and 1 GPa pressures for 30 min. It was found that compression at 1 GPa considerably changed the textural and structural properties of MOF: the crystal structure collapsed and porosity was almost completely lost. Compression of CPO-27-Ni at 0.1 GPa virtually did not change the specific surface area or pore volume and the crystal structure remained intact. Nevertheless, the gravimetric specific capacity of CPO-27-Ni pellets for methane at 303 K and 3.4 MPa was found to decrease compared with that of the initial framework under the same conditions (129 *vs* 156 $cm^3\ g^{-1}$). This attests to the necessity to optimize the compression conditions.

Peterson *et al.*[301] studied the effect of pressing on the physical and chemical properties of HKUST-1 and UiO-66. According to X-ray diffraction and Fourier transform IR spectroscopy, the crystal structures of both MOFs did not change during pressing. The porosity of HKUST-1 considerably decreased, unlike the porosity of UiO-66. Despite the decrease in the porosity of HKUST-1, its adsorption properties towards ammonia did not change. The octane uptake in the UiO-66 pellets was found to slightly decrease as compared with that for the initial structure. Nevertheless, the authors concluded that HKUST-1 and UiO-66 can well be pressed without binders, and the absence of a significant loss of adsorption activity attests to their applicability in adsorption technologies.

Now we will analyze data on the effect of solvents on the changes in the structure and properties of MOFs upon compression in relation to PCN-250, which is a promising adsorbent for methane storage.[302] The structure of PCN-250 is formed by three-dimensional $Fe_3(\mu_3\text{-oxo})$ clusters connected by six ABTC organic linkers. Extrusion under the action of uniaxial mechanical pressure of 19 MPa or more is accompanied by an irreversible change of configuration of the linkers. Analysis of nitrogen adsorption isotherms at 77 K showed a 5.2% decrease in the porosity for the shaped PCN-250. According to powder X-ray diffraction data, pressure rise to 150 MPa induces a phase transition in PCN-250: the cubic crystal lattice is irreversibly transformed into orthorhombic one. It is of interest that the solvent-saturated (DMF) sample of PCN-250 is more stable to mechanical impact and virtually does not change, unlike the sample formed without a solvent under similar conditions of extrusion. Furthermore, shaping of PCN-250 in the presence of a solvent resulted in a 21% increase in the methane volumetric capacity with a minor decrease in the gravimetric capacity. Note that on keeping in DMF, the changed PCN-250 structure is gradually restored, this process being accelerated with increasing temperature. For example, when shaped PCN-250 is kept in DMF at 150 °C, its crystal structure is completely restored in 12 h. Bennett *et al.*[303] assumed that the solvent molecules in MOF pores act as supports preventing the framework destruction. They noted this phenomenon for solvent saturation of the ZIF metal-organic framework in which the solvent molecules considerably decreased the compressibility and increased the resistance to amorphization.

Yuan *et al.*[302] also determined the optimal pressure for extrusion of PCN-250 to be 77 MPa; at this pressure, the sample packing density increases without destruction of the crystal structure or loss of porosity, and the highest methane total volumetric capacity [135 m^3(STP) m^{-3}] is attained.

The wet granulation method was used[266] to prepare spherical pellets of MIL-100(Fe), PCN-250(Fe), UiO-66(Zr) and UiO-66-NH_2(Zr) from their powders mixed with PVA and polyvinylbutyral in ethanol solution using a home-made granulator. After sieving, 1.3–1.7 mm pellets were rolled using a roller machine to enhance the spherical shape and dried in a vacuum furnace at 383 K for 12 h to remove the residual solvent. For both MOF powder and spherical pellets, the adsorption isotherms for gases (N_2, CO, CO_2, CH_4, C_2H_6, C_3H_8, C_3H_6, C_4H_{10}) were measured and adsorption enthalpies were determined. The use of a mixture of binders for granulation of UiO-66(Zr) and UiO-66-NH_2(Zr) did not have a significant effect on the enthalpy of adsorption of small molecules (N_2, CO, CH_4); the enthalpies for gases with large molecules were noted to slightly decrease. The expected decrease in the uptake per gram of the material with spherical granules corresponds to the content of the binder in the pellets. A comparison of the adsorption properties of the initial powders and pellets of MIL-100(Fe) and MIL-127(Fe) revealed two interesting effects, namely

— in the case of butane adsorption, the adsorption isotherms of powdered and pelletized MIL-100(Fe) are considerably different: adsorption with the powder produces the expected Langmuir isotherm shape, while adsorption with spherical pellets gives S-shaped isotherms typical of polymolecular adsorption; this phenomenon was attributed to different enthalpies of adsorption and partial blocking of pores by long-chain binder molecules;

— the activation of MIL-127(Fe) powder and pellets at 423 K is accompanied by a decrease in the enthalpy of adsorption for gases, the molecules of which have a dipole (CO) or quadrupole (CO_2) moment or π-electrons (C_3H_6); however, with increasing degree of pore filling, the difference between the enthalpies of adsorption for spherical pellets and powders almost disappears.

The authors [266] assumed that the addition of the binder does not have a substantial influence on the chemical properties of the framework. In the authors' opinion, the noted increase in the enthalpy during adsorption of CO, C_3H_6 and especially CO_2 with the MIL-127(Fe) powder attests to partial reduction of Fe^{III} to Fe^{II} upon the reaction with gas molecules. Since no increase in the enthalpy was observed during adsorption in spherical pellets, the authors deemed that the binder stabilizes the MOF in the more oxidized state in a certain way; however, they pointed out the need for further research. One of the conclusions they made [266] states the necessity to consider the adsorption capacity of materials in volumetric units. In this case, comparison of the adsorption isotherms indicates a higher uptake in the adsorber filled with high-density MOF spheres with the optimal packing than with powders, which is quite evident.

A decrease in the adsorption activity of MOFs upon formation of composite pellets was noted for HKUST-1.[304] It was shown that HKUST-1 is stable in an O_2 atmosphere at 25 °C, but its crystallinity decreases in moist environments. Study of the adsorption in HKUST-1 composite pellets at 308 K and pressures up to 0.7 MPa showed a decrease in the methane and carbon dioxide uptakes from 0.77 and 3.9 to 0.63 and 3.1 mol kg^{-1}, respectively. The isosteric heats of adsorption on the initial and shaped adsorbents were 22.8 and 15.0 kJ mol^{-1} for carbon dioxide and methane, respectively; therefore, in the separation of a $CO_2 + CH_4$ mixture, predominant adsorption of carbon dioxide will take place.

It is noteworthy that methane adsorption isotherms have no hysteresis and that after desorption, both powdered and pelletized HKUST-1 samples restore their initial weight. Considering the data on adsorption of mixtures and their components, the researchers [304] ascertained the following:

— at low pressures, the adsorbent has a high selectivity to $CO_2 + CH_4$ mixture (5.10 and 4.92 at 0.1 MPa and 308 K for the powder and pellets, respectively);

— adsorption capacity of HKUST-1 pellets is 20% lower than that for the powder; the methane uptake by this adsorbent is ~3 mmol g^{-1} at 308 K and 0.7 MPa (Fig. 40).

The data on methane mass transfer depending on the degree of compression of MOFs determined by NMR porosimetry also deserve attention. Analysis of the distributions of methane spin–spin relaxation times in metal-organic frameworks ZIF-8 and Basolite™ A520 (BASF) revealed [305] the difference between the exchange rates of methane molecules between the gas phase and the adsorbed state in polycrystalline and shaped ZIF-8 samples (two areas with different porosity can be distinguished in the pellets). Conversely, in the Basolite™ A520 powder and pellets, fast exchange of methane molecules between different states results in an averaged distribution of spin–spin relaxation times. The results of measurements of self-diffusion coefficients (pulsed NMR), Knudsen methane diffusion in MOFs and permeability of MOF pellets pressed under various loads were used to determine the optimal loading for compression of MOF powders (2–5 kN) in order to attain unlimited mass transport of methane in the adsorbent.

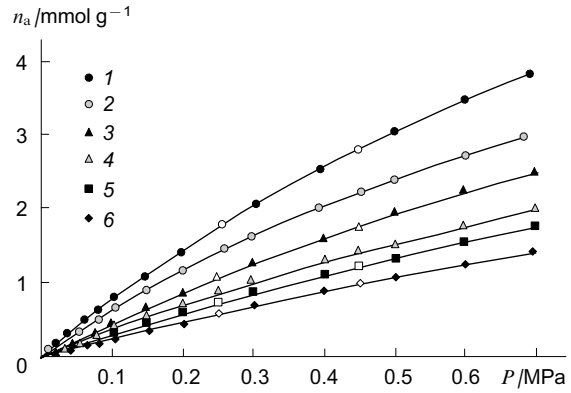


Figure 40. Isotherms of methane adsorption (colour-filled dots) and desorption (unfilled dots) in the pores of HKUST-1 as a powder (*1*, *3* and *5*) and as pellets (*2*, *4*, *6*) at temperatures of 308 (*1*, *2*), 343 (*3*, *4*) and 373 K (*5*, *6*).[304]

The effect of packing density on the methane volumetric uptake was considered [20] in relation to analysis of DOE requirements of 2012 to ANG systems. The loss of adsorption capacity for adsorbents (MOFs and activated carbons; MOF and activated carbon composites with various binders) used as powders and pellets was evaluated (5%–20%). It was shown that up to 11% of the gas passes to the intergrain space. As a strategy towards reducing the adsorption loss, the authors proposed the use of monolithic blocks. In the ideal case, this would completely eliminate the loss.

Tian *et al.*[268] reported a considerable increase in the methane uptake upon increasing the density of the metal-organic framework, which was achieved for HKUST-1 monolith. The monolith was obtained by sol–gel process (Fig. 41), used for the synthesis of organic and inorganic aerogels. The authors showed experimentally that the morphology of the final reaction product is determined by the size of primary particles, the nucleation rate of MOF crystals and the drying temperature. High-temperature drying of a wet gel consisting of primary HKUST-1 particles and residual solvent leads to rapid removal of the solvent from the space between the particles and prevents the formation of a continuous phase. As a result, a polycrystalline HKUST-1 powder with a density of 0.4 g cm^{-3} is formed. As the gel is dried at 303–313 K, self-assembly of unreacted precursors continues on the primary particles. Finally, this gives the HKUST-1 monolith with a density of ~1.1 g cm^{-3}, which is higher than the value calculated for this structure.

The phase state of the samples was determined by powder X-ray diffraction and transmission and scanning electron microscopy. It was found that the powder consisted of aggregated HKUST-1 particles, whereas the monolithic sample was a continuous phase. High density and extensive microporosity [a_s(BET) = 1193 m^2 g^{-1} and W_0 = 0.51 cm^3 g^{-1}] of the HKUST-1 monolith provided the record-high total adsorption capacity for methane

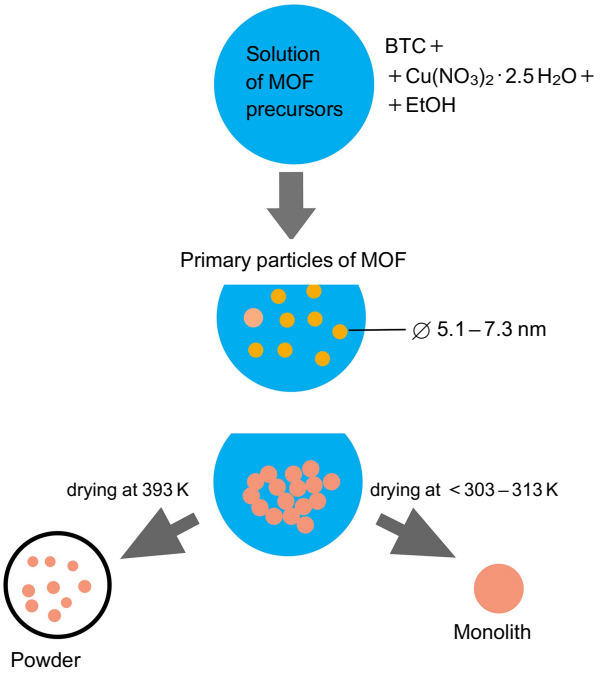


Figure 41. Flow chart of the preparation of HKUST-1 monolith with different drying regimes.
The Figure is based on Ref. 268.

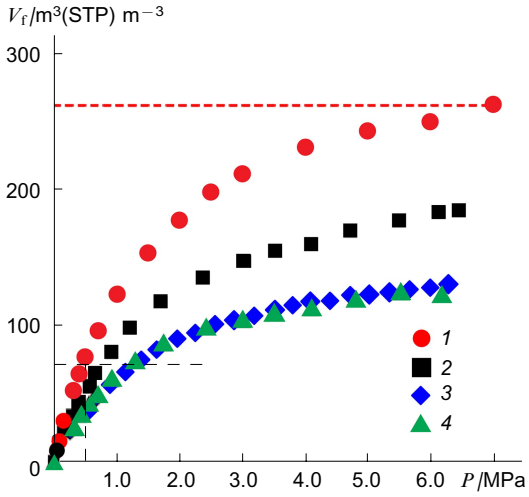


Figure 42. Change in the total volumetric capacity for methane of HKUST-1 monolith (*1*), manually packed pellets (*2*) and pellets pressed under 2 (*3*) and 5 ton (*4*) load at 298 K.[268, 26]
The dashed lines mark the V_f values at P = 3.5 and 6.5 MPa.

storage equal to 259 m³(STP) m⁻³ at 6.5 MPa (Fig. 42). It is noteworthy that now this is the highest total volumetric capacity known for shaped MOFs. Thus, the authors[268] were able to approach the target value of the total adsorption capacity for methane storage V_f = 263–266 m³(STP) m⁻³, defined by the DOE requirements of 2012 for ANG systems and also to approach the theoretical methane uptake for hypothetical MOFs [V_f = 269 m³(STP) m⁻³] calculated using the density of the ideal MOF crystal.[172] The value thus obtained exceeds the maximum V_f value [230 m³(STP) m⁻³] calculated by Peng *et al.*[26] for HKUST-1 after compression.

The adsorption isotherm shown in Fig. 42 (curve *1*) can be used to estimate the deliverable capacity of the HKUST-1 monolith from pressures of 3.5 and 6.5 MPa by Eqn (3): considering the real density of the monolith, the results are 134 and 172 m³(STP) m⁻³, respectively. The obtained V_d values also exceed the results determined by other researchers based on the crystal density of HKUST-1.[26]

Measurements of the mechanical properties of the HKUST-1 monolith confirmed its high strength, which exceeds the value for analogues obtained previously by at least 130%.

Thus, two trends can be distinguished in the shaping of MOFs:

— shaping during the synthesis;

— shaping after the synthesis as an additional processing stage for MOF functionalization.

Both methods have their benefits and drawbacks. Growing of polycrystalline MOF films on structured substrates affords monolithic composites, but the MOF content in the composites is low, which limits their application. Granulation with a binder decreases the specific surface area and the micropore volume of the adsorbent; compression under high pressure induces amorphization of the MOF structure. These drawbacks ultimately account for deterioration of the adsorption properties of shaped MOFs compared with the properties of the initial powder. The successful attempt to apply the sol–gel method for the preparation of monolithic MOF samples with high adsorption capacity for methane storage should be taken into account in elaboration of adsorbent shaping processes. In order to achieve a balance between the increased density, mechanical strength and changes in the structure (including porosity) of the shaped MOF samples, optimization of the shaping techniques is required. This would allow active use of MOFs in ANG technologies.

5. Scaled methane storage systems based on metal-organic frameworks

The reviews devoted to the use of MOFs as adsorbents for natural gas storage also discuss a number of issues that are not purely engineering, but still considerably affect the performance of ANG systems.[54, 85, 148, 150, 152, 153, 295]

First of all, note the influence of minor components[85, 148, 152] of natural gas, particularly, C_2–C_5 hydrocarbons, carbon dioxide, water and sulfur compounds, which are also adsorbed in MOFs, and their desorption requires additional energy supply (heating). This is indirectly confirmed by the results of pulsed magnetic field gradient NMR measurements of self-diffusion of natural gas components such as methane, ethane and propane in the Basolite™ A520 sample and by estimates of the activation energy for diffusion in MOF pores: 13, 24 and 38 kJ mol⁻¹, respectively.[305] The accumulation of impurities, especially sulfur compounds, leads to gradual poisoning of the adsorbent and decreases the adsorption capacity of the ANG system. Hence, to ensure the reliability and long-term efficient operation of MOF-based natural gas (methane) storage systems, the gas should be purified from heavy hydrocarbons and sulfur compounds before it enters the adsorber.

It is necessary to emphasize the importance of studies of cyclic adsorption–desorption of natural gas as a multicomponent gas mixture in MOF-based storage systems proceeding from requirements to ANG systems, which specify that 80% of the tank should be filled in ~5 min and the loss of the specific capacity over 100 adsorption–desorption cycles should be not higher than 5%.[306]

Zhang *et al.*[307] considered a theoretical model of an ANG tank under isothermal conditions. This model was used to calculate the adsorption isotherms of a methane + ethane + propane mixture (natural gas model) in terms of the ideal adsorbed solution theory[308] and the data for separate components of the mixture. As adsorbents for the model adsorber, the authors chose five metal-organic framework systems possessing high deliverable volumetric capacity for methane: HKUST-1, IRMOF-1, NU-111, NU-125 and NU-800. For each MOF, they calculated the so-called deliverable volumetric energy (measured in MJ m^{-3}), that is, the energy equivalent of the V_d value for methane and methane + ethane + propane mixture (Fig. 43). It can be seen that none of the systems complies with the DOE requirements.[19] The storage systems for model natural gas possess a lower deliverable energy than the storage systems for pure methane. The adsorbent–adsorbate interaction energy is much higher for C_{2+} alkanes than for methane; therefore, they are desorbed much less efficiently than methane under the same conditions. This results in blocking of adsorbent pores by molecules of heavy hydrocarbons after several sorption–desorption cycles and, as a consequence, in a decrease in the methane specific capacity of the system.

In addition, while modelling the adsorption of a mixture of hydrocarbon gases in MOFs, Zhang *et al.*[307] obtained an unexpected result. They found that the HKUST-1 adsorbent, which is most promising according to many authors (*e.g.*, Refs 26, 85, 268) rapidly loses the specific characteristics during cyclic operation, by 32% over 200 sorption–desorption cycles, due to irreversible blocking of pores with efficient size of 0.4–1.0 nm, which constitute almost a half of the MOF pore space, by propane molecules (see Fig. 9). Screening of 120 MOFs identified MOF-143 [$Cu_3(BTB)_2$] as the best adsorbent for natural gas,[309] which can provide the highest deliverable volumetric energy of the system of 5.43 MJ m^{-3} on the 200th cycle of operation of the ANG system. Meanwhile, note that MOF-143 has moderate specific capacities for methane: V_f = 208 m^3(STP) m^{-3}, V_d = 182 m^3(STP) m^{-3} (Ref. 309). The authors[307] emphasized that there is still no reliable method to remove the solvent molecules without destroying the crystal structure of MOF-143.

While considering the ways of increasing the performance of the ANG system, the authors[307] quantitatively estimated the effect of the tank space free from the MOF adsorbent on the deliverable volumetric energy of the adsorption storage system for two MOFs, NU-125 and MOF-143. The dependences of the deliverable volumetric energy on the degree of packing of the ANG tank space with the MOF adsorbents are shown in Fig. 44. It can be seen that the deliverable volumetric energy for both structures depends linearly on the fraction of the tank packed by MOF (100% in the abscissa corresponds to complete packing of the tank with MOF monolith). This linear dependence can be used to predict specific characteristics of the system depending on the degree of tank packing.

Other key factors determining the efficiency of the storage system are the method and characteristics of filling. In particular, an important process during filling of the adsorption storage system with natural gas is the transfer (or dissipation) of the heat released to the environment upon adsorption. It is known that fast methane filling of an ANG system containing activated carbon leads to temperature rise inside the tank by 80°C, which retards the adsorption. In turn, at high rates of gas delivery to the consumer, the temperature decreases by 37 °C and, hence, the efficiency of the system decreases by 25% with respect to that under isothermal conditions.[310]

Arnold *et al.*[305] reported modelling of three types of a MOF-based ANG system: without cooling, with external cooling and with both external and internal cooling. They intended to study heat and mass transfer processes and

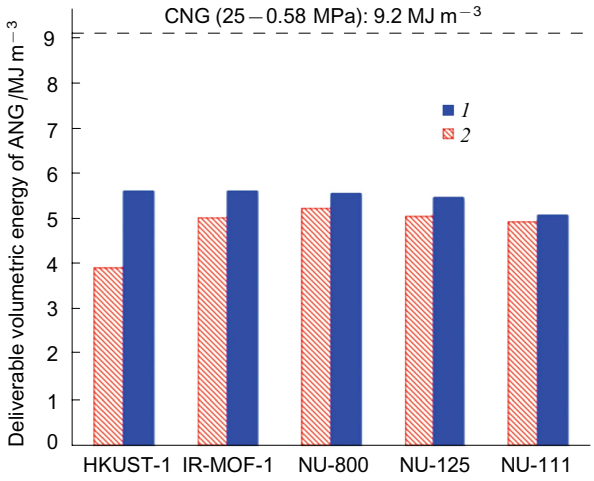


Figure 43. Calculated deliverable energy for methane (*1*) and a model gas mixture (*2*) of MOFs at 6.5 MPa.
The dashed line shows the DOE target value of 2012. The Figure is adapted from Ref. 307.

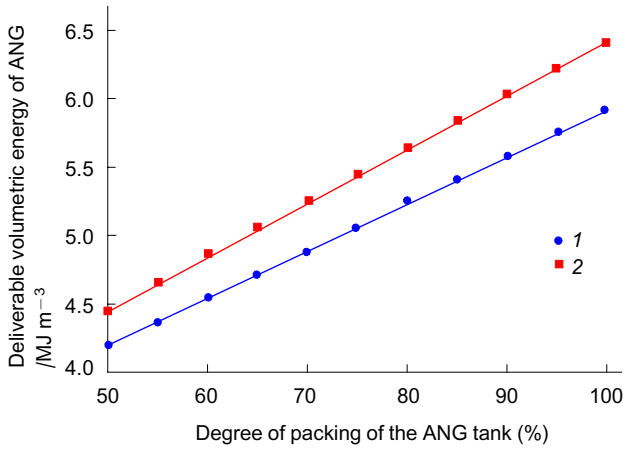


Figure 44. Deliverable volumetric energy of an ANG system (after 199 adsorption–desorption cycles) *vs.* degree of packing of the tank with NU-125 (*1*) and MOF-143 (*2*) adsorbents.
The plots are based on the data of Ref. 307.

determine the optimal cooling conditions for an ANG system to ensure fast gas filling and to maximize the storage capacity. The ambient temperature was taken to be 300 K and the adsorption tanks were filled with natural gas up to a pressure of 9.0 MPa. The authors demonstrated that combining the external and internal cooling circuits provided filling of the system to 90% of the maximum uptake in 30 min, whereas with external cooling and without cooling, filling took 53 and 412 min, respectively. Thermal calculations also showed that after filling, the adsorber is cooled down to 303 K in 79, 112 and 609 min with external and internal cooling, only external cooling and in the absence of cooling, respectively.

Thus, an important aspect of the design of adsorption methane storage systems based on MOFs is engineering analysis of the tank configuration and techniques of cooling, the lack of which puts in question the success of system application. Similar studies of an ANG system with HKUST-1 carried out by computer simulation also demonstrated the inefficiency of using only an external cooling circuit for the tank because of low heat conductivity of MOFs [0.3 W (m K)$^{-1}$].[311]

Reviews [54, 148] describe technological solutions for the problems caused by the heat of gas filling–delivery processes in MOF-based systems. These solutions are based on mathematical models [312] and engineering approaches that were used previously for activated carbon-based systems, including the geometry and material of the tank.[311, 313] In the design of real storage systems, it is necessary to take into account heat capacity and heat conductivity of MOF adsorbents by appropriate selection of precursors, conditions of synthesis, functionalization and shaping in the presence of dopants (*e.g.*, graphite).[297, 314]

Policicchio *et al.*[315] reported evaluation of vehicular adsorption storage systems with highly efficient activated carbon adsorbents, Maxsorb-III (from oil coke) and Nuchar-SA (from wood), and the metal-organic framework HKUST-1, a promising methane adsorbent (Table 11).

Table 11. Characteristics of a model on-board vehicle adsorption methane storage system filled with carbon adsorbents Maxsorb-III and Nuchar-SA and the metal-organic framework HKUST-1.[315]

Characteristics	Maxsorb-III	Nuchar-SA	HKUST-1
For the adsorbent			
Density /kg m^{-3}	0.156	0.34	0.88
a_s(BET) /m^2 g^{-1}	3140	1600	1850
W_t /cm^3 g^{-1} (pore size < 100 nm)	0.179	1.15	0.82
For the adsorption fuel supply system			
Gravimetric capacity /g(CH_4) (kg of the adsorbent)$^{-1}$ at 3.5 MPa	408 [a]	262 [a]	130 [a]
V_f /m^3 m^{-3} at 3.5 MPa	60	52	160
Methane weight in the tank /kg	3.2	4.5	5.7
Volume of the tank /m^3	0.05	0.05	0.05
Weight of the tank /kg	30	30	30
Adsorbent weight /kg	7.8	17	44
Total weight of the system /kg	41	51.5	74
Methane consumption /km kg^{-1}	20	20	20
Running distance /km	64	90	114

[a] Calculated using empirical equations proposed by Policicchio *et al.*[315]

It is noteworthy that the carbon adsorbent Maxsorb-III with the highest a_s(BET) has the highest gravimetric capacity. However, the optimal relationship between the density, porosity and the concentration of adsorption sites in HKUST-1 (see Section 3.1.3) provides a considerable advantage in the volumetric capacity and, as a consequence, ensures high mileages.

Considering the use of HKUST-1 as the adsorbent in an adsorption vehicle fueling system, mention should be made of the EcoFuel Asia Tour project in which a car with the fuel tank filled with HKUST-1 adsorbent pellets (Basolite™ C300) travelled through 14 countries. A ~30% increase in the tank capacity in comparison with the CNG system and a ~20% increase in the distance without refueling were reported.[23] Nevertheless, because of large weight and volume of the system, limited service life and high cost of MOFs, broad commercialization of these materials cannot be expected in the near future.

6. Conclusion

Metal-organic frameworks represent a new class of porous materials, the structure and morphology of which are formed *via* direct assembly of the major components, metal clusters and rigid organic linkers, into 3D frameworks with extensive porosity. The MOF parameters depend on the type of the initial components and conditions of synthesis. The virtually unlimited diversity and variability of MOFs that can be constructed from the mentioned components and the use of various synthetic procedures make these materials, along with activated carbons and zeolites, lead candidate adsorbents for separation and storage of gases, including natural gas (methane).

Currently, solvothermal synthesis is the most popular method for the preparation of MOFs. However, this method is costly in terms of the energy expenditure, cost of reactants and duration of the process and gives low yields of the final product. Optimization of known and development of new synthetic procedures allow partial (or complete) elimination of these drawbacks, in particular, the product yield can be increased and the cost can be decreased. For example, electrochemical and mechanochemical methods are already widely used. In addition, methods for MOF functionalization and modification during and after the synthesis are being actively developed; this allows tuning of physicochemical properties, morphology and pore structure towards a particular application.

A notable feature is the diversity of spatial geometry and numerous options of MOF construction; therefore, MOFs can be selected in terms of their functional properties for particular applications, including those involving sorption technologies. Using high-throughput screening of hypothetical MOFs generated by various combinations of hundreds of secondary building units in terms of compliance with structural parameters of real compounds, characteristics of real structures that meet the efficiency requirements for methane adsorbents were determined to be $V_f \geqslant 230$ m^3(STP) m^{-3} at 3.5 MPa and 298 K. The optimal pore structure parameters were found, namely

— pore size of 0.4 and 0.8 nm accommodating one or two methane molecules, respectively, and 1.1 nm corresponding to the highest density of adsorbed molecules;

— specific surface area equal to 2500–3000 m^2 g^{-1};

— fraction of the free volume equal to 0.8;
— crystal density $0.6 < d_{cr} < 0.953$ kg m^{-3}.

Comparison of the results of computer modelling of methane adsorption in hypothetical MOFs with the results of analysis of pore structure parameters, crystal density and heats of adsorption of real materials provided practically important results. It was found that for maximizing the total and deliverable capacities under particular thermodynamic conditions, a balance between the framework porosity (specific surface area and pore volume) and density is required.

The most challenging goal is to simultaneously attain the required volumetric and gravimetric capacities of a storage system taking account of the adsorber weight. It is evident that high total and deliverable gravimetric capacities are associated with extensive porosity, in particular, with relatively high specific surface areas, *e.g.*, as observed for Al-soc-MOF-1 and DUT-49. Meanwhile, extensive pore structure implies decreasing packing density of the material, which leads to lower volumetric capacity characteristics of the system.

In terms of the relationship between the total and deliverable volumetric and gravimetric capacities, HKUST-1, MAF-38, UTSA-76, NJU-Bai-43, ZJU-5 and UTSA-110 were established to be the optimal adsorbents providing the highest capacity at the minimized weight of the adsorbent packed into the system. From the standpoint of thermodynamics of methane adsorption in MOFs, the range of isosteric heats of adsorption optimal for methane storage was established to be 14 to 22 kJ mol^{-1}.

It is known that in the early period of filling, the adsorption of gas molecules is determined by the adsorbent–adsorbate interactions, which directly depend on the content of high-energy adsorption sites. High concentration of open adsorption sites at metal ions unambiguously dictates high methane uptake, but hampers the desorption. Therefore, the optimal concentration of the adsorption sites is a condition for attaining not only high total capacity for methane storage, but also, what is more important, the deliverable capacity of the adsorbent. The synthetic strategy towards a framework with the optimal ratio of the concentrations of open metal sites and pores accessible for gas sorption implies the use of ligands with different configurations (branching) and length, rigidity and functionality. The incorporation of additional functional groups into polyaromatic carboxylate and heterocyclic ligands makes it possible to increase the concentration of adsorption sites linking methane molecules to the framework *via* van der Waals forces. Polar pyrimidine and amide groups containing a donor nitrogen atom proved to be most efficient.

A series of MOFs with high performance characteristics for methane adsorption were obtained using two or three types of ligands with different lengths and different functionality. High methane deliverable capacity was also attained for frameworks formed by flexible heterocyclic ligands that undergo phase transitions upon the adsorption and desorption of methane. Heats that accompany the structural transformations of MOFs may suppress the temperature oscillations in the adsorption system during adsorption and desorption.

In parallel with the efforts directed towards the synthesis of new MOFs, the industrial production processes for the already known MOFs are being developed in laboratory. Currently, companies such as MOF Technologies, NuMat, BASF and MOFapps manufacture more than a hundred various sorts of MOFs, the best known among them being HKUST-1, ZIF-8, MOF-5, MIL-101 and MOF-177. The potential scope of applicability of these MOFs includes the adsorption-based technologies. A large-scale manufacture of a MOF as a crystalline powder has been developed; however, processes for the design of composites and processing of MOFs to various shapes are also important for commercialization of ANG systems.

The design of composites consisting of MOFs, possessing regular porosity and high crystallinity, and high-strength and hydrophobic carbon adsorbents can serve as an example of synergistic combination providing a high adsorption capacity and enhanced service characteristics (strength, stability, hardness and resistance to external impact). The most promising composites were obtained on the basis of MOFs and carbon materials (activated carbons and carbon nanotubes); this gave not only increasing specific capacity for methane storage, but also increasing hydrophobicity and stability to mechanical and thermal treatment.

Higher methane uptakes of MOFs in ANG systems can be attained by increasing the packing density *via* minimizing the space between the adsorbent grains in the adsorber. As a rule, metal-organic frameworks are obtained as polycrystalline powders of various degrees of dispersion with low density and mechanical properties. These problems can be solved by technological compression. However, the increase in the MOF strength and stability to mechanical impacts upon compression (or granulation) is accompanied by the loss of crystallinity and porosity and, hence, by deterioration of the adsorption properties. The presence of solvent in the pores during compression may help to preserve the structure and adsorption properties of MOFs. The use of binders also affects, most often, the porosity and accessibility of the adsorption sites of MOFs. The most popular binders include poly(vinyl alcohol), cellulose esters and graphite. It was shown that introduction of up to 3% PVA virtually does not affect the specific surface area of the composite. In any case, compression parameters, including pressure, type of binder, degree of dispersion of the adsorbent and the size and shape should be optimized for each MOF-based composite.

The use of MOFs as monoliths obtained by extrusion increases the density and resistance to mechanical impacts; in this case, it is necessary to select the optimal pressure and solvent in such a way that the inevitable change in the porous structure does not affect the methane uptake. The uniform and long-term drying of the dense MOF gel afforded a monolith with a homogeneous phase composition and with adsorption properties being close to the DOE requirements to methane storage and transportation systems.

Although the target total and deliverable capacities of MOFs for methane at the temperature and pressure specified by DOE have not been attained, nevertheless, in view of high total volumetric densities of stored methane [up to 220 m^3(STP) m^{-3}], high methane deliverable capacity [up to 170 m^3(STP) m^{-3}], optimal energy characteristics and relatively high gravimetric storage characteristics (up to 0.25 g(CH_4) g(adsorbent)$^{-1}$), MOFs can be considered as promising adsorbents for ANG systems. However, despite the excellent methane adsorption, for efficient use of MOFs as adsorption systems for natural gas storage, a number of

issues related to physicochemical properties of MOFs should be solved in the near future.

Transition to large-scale use of MOFs in storage systems implies systematic studies of cyclic adsorption – desorption of natural gas as a multicomponent mixture in MOF-based systems in terms of requirements to ANG systems, which specify that 80% of the tank volume should be filled in ~5 min and the loss of the specific capacity over 100 adsorption – desorption cycles should be < 5%. Computer modelling of the adsorption of natural gas as a multicomponent mixture can help to identify the optimal framework that is able to retain the deliverable energy after 200 adsorption – desorption cycles under conditions of predominant adsorption of heavier hydrocarbons. Analysis of heat and mass transfer processes makes it possible to determine the optimal conditions of cooling of ANG systems to ensure fast filling and the highest capacity of the storage system; this implies a combination of external and internal cooling circuits for the adsorbers, providing the highest filling and cooling rates for the system.

In the design of real storage systems, it is necessary to take into account the heat capacity and heat conductivity of MOF adsorbents, which are determined by appropriate selection of precursors, conditions of synthesis, functionalization and shaping with binders.

Thus, the development of industrial processes for the synthesis, functionalization and shaping for large-scale regular manufacture of MOFs would make it possible to obtain sufficient amounts of efficient adsorbents for methane storage and thus actively implement the adsorption storage of natural gas into practice.

Figures 2, 5, 6, 34, 38, 40 are courtesy of Wiley publishers; Figures 9 *b*, 18, 33, 35, 36, 39 are courtesy of Elsevier; Figures 9 *a*, 19, 43 are courtesy of the Royal Society of Chemistry; Figures 29, 42 are courtesy of Springer Nature.

References

1. V.S.Arutyunov, G.V.Lisichkin. *Russ. Chem. Rev.*, **86**, 777 (2017)
2. *International Energy Agency. Monthly Gas Statistics. September 2018*; https://www.iea.org/topics/naturalgas/; https://www.iea.org/media/statistics/surveys/gas/Natgas.pdf/ (Last accessed on 19.07.2019)
3. B.Viswanathan. In *Energy Sources. Fundamentals of Chemical Processes and Applications. Ch. 3. Natural Gas.* (Amsterdam, Boston, Heidelberg, London, New York, Oxford, Paris, San Diego, San Francisco, Singapore, Sydney, Tokyo: Elsevier, 2017). P. 408
4. D.V.Kotov, L.R.Urazmetova. *Neftegaz. Delo*, (1) (2014); http://ogbus.ru/article/view/sovremennoe-sostoyanie-perspektivy-i-problemy-razvitiya-rynka-gazomotornogo-topliva-v-rossii/(Last accessed on 19.07.2019)
5. L.P.Kalacheva, A.F.Fedorova. *Mezhd. Zh. Prikl. Fund. Issl.*, (6 – 3), 395 (2015)
6. Ph.Cleaver, M.Johnson, B.Ho. *J. Hazard. Mater.*, **140**, 429 (2007)
7. O.N.Aneziris, I.A.Papazoglou, M.Konstantinidou, Z.Nivolianitou. *J. Loss Prevent. Proc. Ind.*, **28**, 23 (2014)
8. I.M.Abduragimov, G.N.Kuprin. *Pozharovzryvobezopacnost'*, **23**, 42 (2014)
9. S.Thomas, R.A.Dawe. *Energy*, **28**, 1461 (2003)
10. S.Takeya, H.Mimachi, T.Murayama. *Appl. Energy*, **230**, 86 (2018)
11. C.Solar, A.G.Blanco, A.Vallone, K.Sapag. In *Natural Gas.* (Ed. P.Potočnik). (Sciyo, InTech., 2010). P. 205
12. I.E.Men'shchikov, A.A.Fomkin, A.Yu.Tsivadze, A.V.Shkolin, E.M.Strizhenov, E.V.Khozina. *Adsorption*, **23**, 327 (2017)
13. A.Yu.Tsivadze, O.E Aksyutin, A.Ishkov, I.E.Men'shchikov, A.A.Fomkin, A.V.Shkolin, E.V.Khozina, V.A.Grachev. *Russ. Chem. Rev.*, **87**, 950 (2018)
14. A.Golovoy. In *SAE Technical Paper Series of the Conference on Compressed Natural Gas as Motor Vehicle Fuel, Pittsburg, PA, 1983* P. 831070
15. L.Mentasty, R.J.Faccio, G.Zgrablich. *Adsorpt. Sci. Technol.*, **8**, 105 (1991)
16. K.R.Matranga, A.L.Myers, E.D.Glandt. *Chem. Eng. Sci.*, **47**, 1569 (1992)
17. M.J.Bojana, R.Slootenb, W.Steele. *Sep. Sci. Technol.*, **27**, 1873 (1992)
18. R.F.Cracknell, P.Gordon, K.E.Gubbins. *J. Phys. Chem.*, **97**, 4 (1993)
19. *MOVE Program Overview*. Advanced Research Project Agency, US DOE, 2012; http://arpa-e. energy.gov/sites/default/files/documents/files/MOVEProgram Overview.pdf
20. B.P.Prajwal, K.G.Ayappa. *Adsorption*, **20**, 769 (2014)
21. M.Beckner, A.Dailly. *Appl. Energy*, **162**, 506 (2016)
22. Z.Nie, Y.Lin, X.Jin. *Front. Mech. Eng.*, **11**, 258 (2016)
23. P.Silva, S.M.F.Vilela, J.P.C.Tomer, F.A.Paz. *Chem. Soc. Rev.*, **44**, 6774 (2015)
24. V.V.Butova, M.A.Soldatov, A.A.Guda, K.A.Lomachenko, C.Lamberti. *Russ. Chem. Rev.*, **85**, 280 (2016)
25. A.Yu.Tsivadze, O.E.Aksyutin, A.G.Ishkov, A.A.Fomkin, I.E.Men'shchikov, A.A.Pribylov, V.I.Isaeva, L.M.Kustov, A.V.Shkolin, E.M.Strizhenov. *Prot. Met. Phys. Chem. Surf.*, **52**, 24 (2016)
26. Y.Peng, V.Krungleviciute, I.Eryazici, J.T.Hupp. *J. Am. Chem. Soc.*, **135**, 11887 (2013)
27. L.J.Murray, M.Dinc, J.R.Long. *Chem. Soc. Rev.*, **38**, 1294 (2009)
28. H.Sato, R.Matsuda, K.Sugimoto, M.Takata, S.Kitagawa. *Nat. Mater.*, **9**, 661 (2010)
29. E.A.Berdonosova, K.A.Kovalenko, E.V.Polyakova, S.N.Klyamkin, V.P.Fedin. *J. Phys. Chem. C*, **119**, 13098 (2015)
30. B.R.Saifutdinov, V.I.Isaeva, L.M.Kustov, E.V.Alexandrov. *Russ. Chem. Bull.*, **64**, 1039 (2015)
31. V.I.Isaeva, L.M.Kustov. *Petrol. Chem.*, **50**, 167 (2010)
32. A.A.Simagina, M.V.Polynski, A.V.Vinogradov, E.A.Pidko. *Russ. Chem. Rev.*, **87**, 831 (2018)
33. A.U.Czaja, N.Trukhan, U.Müller. *Chem. Soc. Rev.*, **38**, 1284 (2009)
34. L.R.Mingabudinova, V.V.Vinogradov, V.A.Milichko, E.Hey-Hawkins, A.V.Vinogradov. *Chem. Soc. Rev.*, **45**, 5408 (2016)
35. M.Rubio-Martinez, C.Avci-Camur, A.W.Thornton, I.Imaz, D.Maspochbc, M.R.Hill. *Chem. Soc. Rev.*, **46**, 3453 (2017)
36. http://www.moftechnologies.com/products/ (Last accessed on 19.07.2019)
37. https://www.sigmaaldrich.com/technical-documents/articles/materials-science/metal-organic-frameworks/alohbdc.html (Last accessed on 19.07.2019)

38. https://www.americanelements.com/iron-azobenzene-tetracarboxylic-porous-1771755-22-6/ (Last accessed on 01.03.2019)
39. https://www.strem.com/uploads/resources/documents/krictmof.pdf/ (Last accessed on 19.07.2019)
40. https://www.numat-tech.com/ion-x-oem-data/ (Last accessed on 19.07.2019)
41. S.Kayal, A.Chakraborty. *Chem. – Eng. J.*, **334**, 780 (2018)
42. B.Szczęśniak, J.Choma, M.Jaroniec. *J. Colloid Interface Sci.*, **514**, 801 (2018)
43. A.Domán, B.Nagy, L.P.Nichele, D.Srankó, J.Madarász, K.László. *Appl. Surface Sci.*, **434**, 1300 (2018)
44. X.Dai, X.Shi, C.Huo, X.Wang. *Thermochim. Acta*, **657**, 39 (2017)
45. H.You, S.Yang, B.Ding, H.Yang. *Chem. Soc. Rev.*, **42**, 2880 (2013)
46. G.Lu, S.Li, Z.Guo, O.K.Farha, B.G.Hauser, X.Qi, Y.Wang, X.Wang, S.Han, X.Liu, J.S.DuChene, H.Zhang, Q.Zhang, X.Chen, J.Ma, S.C.J.Loo, W.D.Wei, Y.Yang, J.T.Hupp, F.Huo. *Nat. Chem.*, **4**, 310 (2012)
47. A.J.Nozik, M.C.Beard, J.M.Luther, M.Law, R.J.Ellingson, J.C.Johnson. *Chem. Rev.*, **110**, 6873 (2010)
48. D.Buso, J.Jasieniak, M.D.H.Lay, P.Schiavuta, P.Scopece, J.Laird, H.Amenitsch, A.J.Hill, P.Falcaro. *Small*, **8**, 80 (2012)
49. P.Falcaro, R.Ricco, C.M.Doherty, K.Liang, A.J.Hill, M.J.Styles. *Chem. Soc. Rev.*, **43**, 5513 (2014)
50. Q.-L.Zhu, Q.Xu. *Chem. Soc. Rev.*, **43**, 5468 (2014)
51. O.Shekhah, L.Fu, R.Sougrat, Y.Belmabkhout, A.J.Cairns, E.P.Giannelis, M.Eddaoudi. *Chem. Commun.*, **48**, 11434 (2012)
52. A.Sachse, R.Ameloot, B.Coq, F.Fajula, B.Coasne, D.De Vos, A.Galarneau. *Chem. Commun.*, **48**, 4749 (2012)
53. A.W.Thornton, K.M.Nairn, J.M.Hill, A.J.Hill, M.R.Hill. *J. Am. Chem. Soc.*, **131**, 10662 (2009)
54. B.Li, H.-M.Wen, W.Zhou, J.Q.Xu, B.Chen. *Chemistry.*, **1**, 557 (2016)
55. B.F.Hoskins, R.Robson *J. Am. Chem. Soc.*, **111**, 5962 (1989)
56. S.R.Batten, N.R.Champness, X.-M.Chen, J.Garcia-Martinez, S.Kitagawa, L.Ohrstrom, M.O'Keeffe, M.P.Suh, J.Reedijk. *Cryst. Eng. Commun.*, **14**, 3001 (2012)
57. S.R.Batten, N.R.Champness, X.-M.Chen, J.Garcia-Martinez, S.Kitagawa, L.Öhrström, M.O'Keeffe, M.P.Suh, J.Reedijk. *Pure Appl. Chem.*, **85**, 1715 (2013)
58. C.Baerlocher, W.M.Meier, D.H.Olson. *Atlas of Zeolite Framework Types*. Elsevier, Amsterdam, 2001
59. O.M.Yaghi, C.E.Davis, G.Li, H.Li. *J. Am. Chem. Soc.*, **119**, (1997)
60. O.M.Yaghi, M.O'Keefi, N.W.Ockwig, M.Eddaoudi, J.Kim. *Nature (London)*, **423**, 705 (2003)
61. D.J.Tranchemontagne, J.L.Mendoza-Corters, M.O'Keeffe, O.M.Yaghi. *Chem. Soc. Rev.*, **38**, 1257 (2009)
62. B.Jha, D.N.Singh. *Fly Ash Zeolites, Ser. Adv. Struct. Mater.*, **78**, 92 (2016)
63. J.L.C.Rowsell, O.M.Yaghi. *Microporous Mesoporous Mater.*, **73**, 3 (2004)
64. http://www.crystal.unito.it/animations-of-vibrational-modes.php (Last accessed on 19.07.2019)
65. J.H.Cavka, S.Jakobsen, U.Olsbye, N.Guillou, C.Lamberti, S.Bordiga K.P.Lillerud. *J. Am. Chem. Soc.*, **130**, 13850 (2008)
66. S.Yuan, L.Feng, K.Wang, J.Pang, M.Bosch, C.Lollar, Y.Sun, J.Qin, X.Yang, P.Zhang, Q.Wang, L.Zou, Y.Zhang, L.Zhang, Y.Fang, J.Li, H.-C.Zhou. *Adv. Mater.*, **30**, 1704303 (2018)
67. H.Furukawa, K.E.Cordova, M.O'Keeffe, O.M.Yaghi. *Science*, **341**, 1230444 (2013)
68. M.O'Keeffe, M.A.Peskov, S.J.Ramsden, O.M.Yaghi. *Acc. Chem. Res.*, **41**, 1782 (2008)
69. M.Li, D.Li, M.O'Keeffe, O.M.Yaghi. *Chem. Rev.*, **114**, 1343 (2014)
70. M.Eddaoudi, J.Kim, J.B.Wachter, H.K.Chae, M.O'Keeffe, O.M.Yaghi. *J. Am. Chem. Soc.*, **123**, 4368 (2001)
71. M.Eddaoudi, J.Kim, J.B.Wachter, H.K.Chae, M.O'Keeffe, O.M.Yaghi. *J. Am. Chem. Soc.*, **124**, 376 (2001)
72. R.Anderson, D.A.Gómez-Gualdrón. *CrystEngComm.*, **21**, 1653 (2019)
73. P.Z.Moghadam, A.Li, S.B.Wiggin, A.Tao, A.G.P.Maloney, P.A.Wood, S.C.Ward, D.Fairen-Jimenez. *Chem. Mater.*, **29**, 2618 (2017)
74. Y.-R.Lee, J.Kim, W.-S.Ahn. *Korean J. Chem. Eng.*, **30**, 1667 (2013)
75. *IUPAC Manual of Symbols and Terminology. Pure Appl. Chem.*, **57**, 603 (1985)
76. H.Li, M.Eddaoudi, T.L.Groy, O.M.Yaghi. *J. Am. Chem. Soc.*, **120**, 8571 (1998)
77. M.Eddaoudi, D.B.Moler, H.Li, B.Chen, T.M.Reineke, M.O'Keeffe, O.M.Yaghi. *Acc. Chem. Res.*, **34**, 319 (2001)
78. H.Li, M.Eddaoudi, M.O'Keeffe, O.M.Yaghi. *Nature (London)*, **402**, 276 (1999)
79. A.Schoedel, O.M.Yaghi. In *Macrocyclic and Supramolecular Chemistry: How Izatt-Christensen Award Winners Shaped the Field*. (Ed. M.Izatt). (Chichester: Wiley, 2016). P. 200
80. S.J.Gregg, K.S.W.Sing. *Adsorption, Surface Area and Porosity*. Academic Press, San Diego, CA, 1982
81. M.Thommes, K.Kaneko, A.V.Neimark, J.P.Olivier, F.Rodríguez-Reinoso, J.Rouquerol, K.S.W.Sing. *Pure Appl. Chem.*, **87**, 1051 (2015)
82. M.Eddaoudi, J.Kim, N.Rosi, D.Vodak, J.Wachter, M.O'Keeffe, O.M.Yaghi. *Science*, **295**, 469 (2002)
83. J.Zheng, R.S.Vemuri, L.Estevez, P.K.Koech, T.Varga, D.M.Camaioni, T.A.Blake, B.P.McGrail, R.K.Motkuri. *J. Am. Chem. Soc.*, **139**, 10601 (2017)
84. M.C.Bernini, D.Fairen-Jimenez, M.Pasinetti, A.J.Ramirez-Pastor, R.Q.Snurr. *J. Mater. Chem. B*, **2**, 766 (2014)
85. J.A.Mason, M.Veenstra, J.R.Long. *Chem. Sci.*, **5**, 32 (2014)
86. F.-X.Coudert, A.H.Fuchs. *Coord. Chem. Rev.*, **307** (Pt. 2), 211 (2016)
87. I.M.Hönicke, I.Senkovska, V.Bon, I.A.Baburin, N.Bönisch, S.Raschke, J.D.Evans, S.Kaskel. *Angew. Chem., Int. Ed.*, **57**, 13780 (2018)
88. S.Brunauer, P.H.Emmett, E.Teller. *J. Am. Chem. Soc.*, **60**, 309 (1938)
89. O.K.Farha, I.Eryazici, N.C.Jeong, B.G.Hauser, C.E.Wilmer, A.A.Sarjeant, R.Q.Snurr, S.T.Nguyen, A.Yazaydin. *J. Am. Chem. Soc.*, **134**, 15016 (2012)
90. V.I.Isaeva, L.M.Kustov. *Russ. Chem. Bull., Int. Ed.*, **65**, 2103 (2016)

91. V.I.Isaeva, L.M.Kustov. In *Zeolites and Zeolite-like Materials*. (Eds B.F.Sels, L.M.Kustov). (Amsterdam: Elsevier, 2016). p. 33
92. M.M.Dubinin. *Prog. Surf. Membr. Sci.*, **9**, 1 (1975)
93. K.V.Kumar, K.Preuss, M.M.Titirici, F.Rodríguez-Reinoso. *Chem. Rev.*, **117**, 1796 (2017)
94. Y.Zhang, B.E.G.Lucier, M.Fischer, Z.Gan, P.D.Boyle, B.Desveaux, Y.Huang. *Chem. – Eur. J.*, **24**, 7866 (2018)
95. Y.-R.Lee, J.Kim, W.-S.Ahn. *Korean J. Chem. Eng.*, **30**, 1667 (2013)
96. N.Stock, S.Biswas. *Chem. Rev.*, **112**, 933 (2012)
97. V.F.Cheong, P.Y.Moh. *Mater. Sci. Technol.*, **34**, 1025 (2018)
98. D.DeSantis, J.A.Mason, B.D.James, C.Houchins, J.R.Long, M.Veenstra. *Energy Fuels*, **31**, 2024 (2017)
99. O.M.Yaghi, H.Li. *J. Am. Chem. Soc.*, **117**, 10401 (1995)
100. J.Li, S.Cheng, Q.Zhao, P.Long, J.Dong. *Int. J. Hydrogen. Energy*, **34**, 1377 (2009)
101. G.Ferey. *Chem. Soc. Rev.*, **37**, 191 (2008)
102. H.R.Abid, H.Tian, H.M.Ang, M.O.Tade, C.E.Buckley, S.Wang. *Chem. Eng. J.*, **187**, 415 (2012)
103. G.Férey, C.M.Drazniekes, C.Serre, F.Millange, J.Dutour, S.Surblé, I.Margiolaki. *Science*, **309**, 2040 (2005)
104. S.S.-Y.Chui, S.M.-F.Lo, J.P.H.Charmant, A.G.Orpen, I.D.Williams. *Science*, **283**, 1148 (1999)
105. P.Horcajada, S.Surblé, C.Serre, D.Y.Hong, Y.K.Seo, J.S.Chang, J.M.Grenèche, I.Margiolaki, G.Férey. *Chem. Commun.*, 2820 (2007)
106. R.Banerjee, A.Phan, B.Wang, C.Knobler, H.Furukawa, M.O'Keeffe, O.M.Yaghi. *Science*, **319**, 939 (2008)
107. S.H.Jhung, J.H.Lee, J.S.Chang. *Bull. Korean Chem. Soc.*, **26**, 880 (2005)
108. J.S.Choi, W.J.Son, J.Kim, W.S.Ahn. *Microporous Mesoporous Mater.*, **116**, 727 (2008)
109. Y.K.Seo, G.Hundal, I.T.Jang, Y.K.Hwang, C.H.Jun, J.S.Chang. *Microporous Mesoporous Mater.*, **119**, 331 (2009)
110. M.Schlesinger, S.Schulze, M.Hietschold, M.Mehring. *Microporous Mesoporous Mater.*, **132**, 121 (2010)
111. V.I.Isaeva, A.L.Tarasov, L.E.Starannikova, Yu.P.Yampol'skii, A.Yu.Alent'ev, L.M.Kustov. *Russ. Chem. Bull., Int. Ed.*, **64**, 2791 (2015)
112. W.-J.Son, J.Kim, J.Kim, W.-S.Ahn. *Chem. Commun.*, 6336 (2008)
113. Z.Q.Li, L.G.Qiu, T.Su, Y.Wu, W.Wang, Z.Y.Wu, X.Jiang. *Mater. Lett.*, **63**, 78 (2009)
114. H.Y.Cho, J.Kim, S.N.Kim, W.S.Ahn. *Microporous Mesoporous Mater.*, **169**, 180 (2013)
115. A.Pichon, A.Lazuen-Garay, S.L.James. *Cryst. Eng. Commun.*, **8**, 211 (2006)
116. P.J.Beldon, L.Fábián, R.S.Stein, A.Thirumurugan, A.K.Cheetham, T.Friši. *Angew. Chem., Int. Ed.*, **49**, 9640 (2010)
117. Patent PCT 049892 (2005)
118. Patent US 20120297982A1 (2012)
119. A.Martinez Joaristi, J.Juan-Alcaniz, P.Serra-Crespo, F.Kapteijn, J.Gascon. *Cryst. Growth Des.*, **12**, 3489 (2012)
120. M.Li, M.Dinca. *Chem. Sci.*, **5**, 107 (2014)
121. E.R.Parnham, R.E.Morris. *Acc. Chem. Res.*, **40**, 1005 (2007)
122. D.N.Dybtsev, H.Chun, K.Kim. *Chem. Commun.*, 1594 (2004)
123. M.G.Del P'opolo, G.A.Voth. *J. Phys. Chem. B*, **108**, 1744 (2004)
124. L.Huang, H.Wang, J.Chen, Z.Wang, J.Sun, D.Zhao, Y.Yan. *Microporous Mesoporous Mater.*, **58**, 105 (2003)
125. D.L.Tranchemontagne, J.R.Hunt, O.M.Yaghi. *Tetrahedron*, **64**, 8553 (2008)
126. C.Duan, F.Li, J.Xiao, Z.Liu, C.Li, H.Xi. *Sci. China Mater.*, **60**, 1205 (2017)
127. R.Ameloot, F.Vermoortele, W.Vanhove, M.B.Roeffaers, B.F.Sels, D.E De Vos. *Nat. Chem.*, **3**, 382 (2011)
128. M.Rubio-Martinez, T.D.Hadley, M.P.Batten, K.Constanti-Carey, T.Barton, D.Marley, A.Mçnch, K.-S.Lim, M.R.Hill. *ChemSusChem.*, **9**, 938 (2016)
129. A.Carne-Sanchez, I.Imaz, M.Cano-Sarabia, D.Maspoch. *Nat. Chem.*, **5**, 203 (2013)
130. www.mofapps.com/mofapps-sucessfully-produce-large-batch-of-mof-materials-using-spray-drying-material-simulating-industrial-conditions-2/ (Last accessed on 19.07.2019)
131. J.Rouquerol, F.Rouquerol, P.Llewellyn, G.Maurin, K.S.W.Sing. *Adsorption by Powders, and Porous Solids. Principles, Methodology and Applications*. (2nd Edn). (Amsterdam: Elsevier, Academic Press, 2014)
132. K.S.Park, A.P.Cote, J.Y.Choi, R.Huang, F.J.Uribe-Romo, H.K.Chae, P.M.O'Keeffe. *Proc. Natl. Acad. Sci.*, **103**, 10186 (2006)
133. B.F.Hoskins, R.Robson. *J. Am. Chem. Soc.*, **112**, 1546 (1990)
134. Y.Cui, B.Li, H.He, W.Zhou, B.Chen, G.Qian. *Acc. Chem. Res.*, **49**, 483 (2016)
135. J.Juan-Alcañiz, J.Gascon, F.Kapteijn. *J. Mater. Chem.*, **22**, 10102 (2012)
136. K.Sugikawa, Y.Furukawa, K.Sada. *Chem. Mater.*, **23**, 3132 (2011)
137. S.M.Cohen. *Chem. Rev.*, **112**, 970 (2011)
138. Z.Wang, K.K.Tanabe, S.M.Cohen. *Chem. – Eur. J.*, **16**, 212 (2010)
139. J.A.Greathouse, M.D.Allendorf. *J. Am. Chem. Soc.*, **128**, 10678 (2006)
140. S.S.Kaye, A.Dailly, O.M.Yaghi, J.R.Long. *J. Am. Chem. Soc.*, **129**, 14176 (2007)
141. *IUPAC. Compendium of Chemical Terminology*. (2nd Edn). (Oxford: Blackwell Science, 1997)
142. *GOST 2939-63 Gasy. Usloviya dlya Opredeleniya Ob'ema*. (GOST 2939-63 Gases. Conditions for Determination of Volume). (Moscow: Izd. Standartov, 1988)
143. J.D.Wright, A.N.Johnson, M.R.Moldover. *J. Res. Natl. Inst. Stand. Technol.*, **108**, 21 (2003)
144. J.Sun, T.A.Brady, M.J.Rood, C.M.Lehmann. *Energy Fuels*, **11**, 316 (1997)
145. E.M.Strizhenov, A.V.Shkolin, A.A.Fomkin, A.A.Pribylov, A.A.Zherdev, I.A.Smirnov. *Prot. Met. Phys. Chem. Surf.*, **49**, 521 (2013)
146. A.E.Koveshnikov. *Geologiya Nefti i Gaza*. (Geology of Oil and Gas). (Tomsk: Tomsk Polytechnic University, 2010)
147. T.A.Makal, J.R.Li, W.Lu, H.C.Zhou. *Chem. Soc. Rev.*, **41**, 7761 (2012)
148. K.Konstas, T.Osl, Y.Yang, M.Batten, N.Burke, A.J.Hill, M.R.Hill. *J. Mater. Chem.*, **22**, 16698 (2012)
149. B.Li, H.M.Wen, W.Zhou, B.Chen. *J. Phys. Chem. Lett.*, **5** 3468 (2014)
150. Y.He, W.Zhou, G.Qian, B.Chen. *Chem. Soc. Rev.*, **43**, 5657 (2014)

151. A.Schoedel, Z.Ji, O.M.Yaghi. *Nat. Energy*, **1**, 16034 (2016)
152. Y.He, F.Chen, B.Li, G.Qian, W.Zhou, B.Chen. *Coord. Chem. Rev.*, **373**, 167 (2018)
153. H.Li, K.Wang, Y.Sun, C.T.Lollar, J.Li, H.-C.Zhou. *Mater. Today*, **21**, 108 (2018)
154. L.Öhrström. *Crystals*, **5**, 154 (2015)
155. J.P.Zhang, P.Q.Liao, H.L.Zhou, R.B.Lin, X.M.Chen. *Chem. Soc. Rev.*, **43**, 5789 (2014)
156. S.-I.Noro, S.Kitagawa, M.Kondo, K.Seki. *Angew. Chem., Int. Ed.*, **39**, 2082 (2000)
157. M.Kondo, T.Yoshitomi, K.Seki, H.Matsuzaka, S.Kitagawa. *Angew. Chem., Int. Ed. Engl.*, **36**, 1725 (1997)
158. S.Kitagawa, R.Kitaura, S.-I.Noro. *Angew. Chem., Int. Ed.*, **43**, 2334 (2004)
159. I.Senkovska, S.Kaskel. *Microporous Mesoporous Mater.*, **112**, 108 (2008)
160. P.L.Llewellyn, S.Bourrelly, C.Vagner, N.Heymans, H.Leclerc, A.Ghoufi, P.Bazin, A.Vimont, M.Daturi, T.Devic, C.Serre, G.D.Weireld, G.Maurin. *J. Phys. Chem. C*, **117**, 962 (2013)
161. Z.Guo, H.Wu, G.Srinivas, Y.Zhou, S.Xiang, Z.Chen, Y.Yang, W.Zhou, M.O'Keeffe, B.Chen. *Angew. Chem., Int. Ed.*, **50**, 3178 (2011)
162. Y.Peng, G.Srinivas, C.E.Wilmer, I.Eryazici, R.Q.Snurr, J.T.Hupp, T.Yildirim, O.K.Farh. *Chem. Commun.*, **49**, 2992 (2013)
163. C.E.Wilmer, O.K.Farha, T.Yildirim, I.Eryazici, V.Krungleviciute, A.A.Sarjeant, R.Q.Snurr, J.T.Hupp. *Energy Environ. Sci.*, **6**, 1158 (2013)
164. S.Q.Ma, D.F.Sun, J.M.Simmons, C.D.Collier, D.Q.Yuan, H.C.Zhou. *J. Am. Chem. Soc.*, **130**, 1012 (2008)
165. Y.Yan, M.Suyetin, E.Bichoutskaia, A.J.Blake, D.R.Allan, S.A.Barnett. M.Schröder. *Chem. Sci.*, **4**, 1731 (2013)
166. B.Li, H.M.Wen, H.L.Wang, H.Wu, M.Tyagi, T.Yildirim, W.Zhou, B.L.Chen. *J. Am. Chem. Soc.*, **136**, 6207 (2014)
167. M.Zhang, W.Zhou, T.Pham, K.A.Forrest, W.Liu, Y.He, H.Wu, T.Yildirim, B.Chen, B.Space, Y.Pan, M.J.Zaworotko, J.Bai. *Angew. Chem., Int. Ed.*, **56**, 11426 (2017)
168. Y.Yan, D.I.Kolokolov, I.da Silva, A.G.Stepanov, A.J.Blake, A.Dailly, P.Manuel, C.C.Tang, S.Yang, M.Schröder. *J. Am. Chem. Soc.*, **139**, 13349 (2017)
169. H.-M.Wen, B.Li, L.Li, R.-B.Lin, W.Zhou, G.Qian, B.Chen. *Adv. Mater.*, **30**, 1704792 (2018)
170. C.E.Wilmer, M.Leaf, C.Y.Lee, O.K.Farha, B.G.Hauser, J.T.Hupp, R.Q.Snurr. *Nat. Chem.*, **4**, 83 (2011)
171. X.Lin, I.Telepeni, A.J.Blake, A.Dailly, C.M.Brown, J.M.Simmons, M.Zoppi, G.S.Walker, K.M.Thomas, T.J.Mays, P.Hubberstey, N.R.Champness, M.Schröder. *J. Am. Chem. Soc.*, **131**, 2159 (2009)
172. C.M.Simon, J.Kim, D.A.Gomez-Gualdron, J.S.Camp, Y.G.Chung, R.L.Martin, R.Mercado, M.W.Deem, D.Gunter, M.Haranczyk, D.S.Sholl, R.Q.Snurr, B.Smit. *Energy Environ. Sci.*, **8**, 1190 (2015)
173. Y.G.Chung, J.Camp, M.Haranczyk, B.Sikora, D.S.Sholl, R.Q.Snurr. *Chem. Mater.*, **26**, 6185 (2014)
174. C.-X.Chen, Z.-W.Wei, J.-J.Jiang, S.-P.Zheng, H.-P.Wang, Q.-F.Qiu, C.-C.Cao, D.Fenske, C.-Y.Su. *J. Am. Chem. Soc.*, **139**, 6034 (2017)
175. D.Sun, S.Ma, J.M.Simmons, J.-R.Li, D.Yuan, H.-C.Zhou. *Chem. Commun.*, **46**, 1329 (2010)
176. C.Song, H.Liu, J.Jiao, D.Bai, W.Zhou, T.Yildirim, Y.He. *Dalton Trans.*, **45**, 7559 (2016)
177. J.A.Mason, J.Oktawiec, M.K.Taylor, M.R.Hudson, J.Rodriguez, J.E.Bachman, M.I.Gonzalez, A.Cervellino, A.Guagliardi, C.M.Brown, P.L.Llewellyn, N.Masciocchi, J.R.Long. *Nature (London)*, **527**, 357 (2015)
178. F.Gandara, H.Furukawa, S.Lee, O.M.Yaghi. *J. Am. Chem. Soc.*, **136**, 5271 (2014)
179. S.Himeno, T.Tomita, K.Suzuki, S.Yoshida. *Microporous Mesoporous Mater.*, **98**, 62 (2007)
180. E.Flanigen, J.Bennett, R.Grose, J.Cohen, R.Patton, R.Kirchner, J.Smith. *Nature (London)*, **271**, 512 (1978)
181. W.Lu, D.Yuan, D.Zhao, C.I.Schilling, O.Plietzsch, T.Muller, S.Brase, J.Guenther, J.Blumel, R.Krishna, Z.Li, H.-C.Zhou. *Chem. Mater.*, **22**, 5964 (2010)
182. J.Perez-Pellitero, H.Amrouche, F.R.Siperstein, G.Pirngruber, C.Nieto-Draghi, G.Chaplais, A.Simon-Masseron, D.Bazer-Bachi, D.Peralta, N.Bats. *Chem. – Eur. J.*, **16**, 1560 (2010)
183. C.M.Simon, E.Braun, C.Carraro, B.Smit. *Proc. Natl. Acad. Sci.*, **114**, E287 (2017)
184. D.A.Gomez-Gualdron, C.M.Simon, W.Lassman, D.Chen, R.L.Martin, M.Haranczyk, O.K.Farha, B.Smit, R.Q.Snurr. *Chem. Eng. Sci.*, **159**, 18 (2017)
185. H.Wu, W.Zhou, T.Yildirim. *J. Am. Chem. Soc.*, **131**, 4995 (2009)
186. H.Wu, J.M.Simmons, Y.Liu, C.M.Brown, X.-S.Wang, S.Ma, V.K.Peterson, P.D.Southon, C.J.Kepert, H.-C.Zhou, T.Yildirim, W.Zhou. *Chem. – Eur. J.*, **16**, 5205 (2010)
187. R.Yun, Z.Lu, Y.Pan, X.You, J.Bai. *Angew. Chem., Int. Ed.*, **52**, 11282 (2013)
188. D.-X.Xue, Q.Wang, J.Bai. *Coord. Chem. Rev.*, **378**, 2 (2019)
189. C.-C.Liang, Z.-L.Shi, C.-T.He, J.Tan, H.-D.Zhou, H.-L.Zhou. *J. Am. Chem. Soc.*, **139**, 13300 (2017)
190. J.Jiang, H.Furukawa, Y.-B.Zhang, O.M.Yaghi. *J. Am. Chem. Soc.*, **138**, 10244 (2016)
191. J.-M.Lin, C.-T.He, Y.Liu, P.-Q.Liao, D.-D.Zhou, J.-P.Zhang, X.-M.Chen. *Angew. Chem., Int. Ed.*, **55**, 4674 (2016)
192. J.Jiao, H.Liu, D.Bai, Y.He. *Inorg. Chem.*, **55**, 3974 (2016)
193. A.A.Fomkin, A.Yu.Tsivadze, O.E.Aksyutin, A.G.Ishkov, A.A.Pribylov, A.V.Shkolin, I.E.Men'shchikov, K.V.Romanov, R.V.Teterevlev, U.Müller, L.Arnold, M.Piontek. *Prot. Met. Phys. Chem. Surf.*, **54**, 347 (2018)
194. M.K.Knyazeva, A.V.Shkolin, A.A.Fomkin, A.Yu.Tsivadze, O.V.Solovtsova, N.P.Platonova, A.L.Pulin, I.E.Men'shchikov, A.A.Shiryaev, V.V.Vysotskii, M.R.Kiselev. *Prot. Met. Phys. Chem. Surf.*, **54**, 1004 (2018)
195. M.K.Batrakova, O.V.Solovtsova, A.A.Fomkin, A.Yu.Tsivadze, A.V.Shkolin, A.A.Shiryaev, V.V.Vysotskii. *Prot. Met. Phys. Chem. Surf.*, **53**, 961 (2017)
196. A.A.Pribylov, K.O.Murdmaa, O.V.Solovtsova, M.K.Knyazeva. *Russ. Chem. Bull., Int. Ed.*, **67**, 1807 (2018)
197. M.K.Knyazeva, A.Yu.Tsivadze, O.V.Solovtsova, A.A.Fomkin, A.A.Pribylov, A.V.Shkolin, A.L.Pulin, I.E.Men'shchikov. *Prot. Met. Phys. Chem. Surf.*, **55**, 11 (2019)

198. A.V.Shkolin, A.A.Fomkin, A.Yu.Tsivadze, K.M.Anuchin, I.E.Men'shchikov, A.L.Pulin. *Prot. Met. Phys. Chem. Surf.*, **52**, 955 (2016)
199. A.A.Fomkin, K.M.Anuchin, A.P.Korotych, A.M.Tolmachev. *Prot. Met. Phys. Chem. Surf.*, **50**, 173 (2014)
200. D.Alezi, Y.Belmabkhout, M.Suetin, P.M.Bhatt, L.J.Weselinski, V.Solovyeva, K.Adil, I.Spanopoulos, P.N.Trikalitis, A.H.Emwas, M.Eddaoudi. *J. Am. Chem. Soc.*, **137**, 13308 (2015)
201. U.Stoeck, S.Krause, V.Bon, I.Senkovska, S.Kaskel. *Chem. Commun.*, **48**, 10841 (2012)
202. T.K.Prasad, M.P.Suh. *Chem. – Eur. J.*, **18**, 8673 (2012)
203. Y.He, H.Furukawa, C.Wu, M.O'Keeffe, R.Krishna, B.Chen. *Chem. Commun.*, **49**, 6773 (2013)
204. N.Klein, I.Senkovska, I.A.Baburin, R.Gruünker, U.Stoeck, M.Schlichtenmayer, B.Streppel, U.Mueller, S.Leoni, M.Hirscher, S.Kaskel. *Chem. – Eur. J.*, **17**, 13007 (2011)
205. H.Furukawa, N.Ko, Y.B.Go, N.Aratani, S.B.Choi, E.Choi, A.O.Yazaydin, R.Q.Snurr, M.O'Keeffe, J.Kim, O.M.Yaghi. *Science*, **329**, 424 (2010)
206. J.I.Feldblyum, D.Dutta, A.G.Wong-Foy, A.Dailly, J.Imirzian, D.W.Gidley, A.J.Matzger. *Langmuir*, **29**, 8146 (2013)
207. G.Barin, V.Krungleviciute, D.A.Gomez-Gualdron, A.A.Sarjeant, R.Q.Snurr, J.T.Hupp, T.Yildirim, O.K.Farha. *Chem. Mater.*, **26**, 1912 (2014)
208. J.Pang, F.Jiang, M.Wu, D.Yuan, K.Zhou, J.Qian, K.Su, M.Hong. *Chem. Commun.*, **50**, 2834 (2014)
209. Y.Yan, S.Yang, A.J.Blake, W.Lewis, E.Poirier, S.A.Barnett, N.R.Champness, M.Schröder. *Chem. Commun.*, **47**, 9995 (2011)
210. D.Han, F.-L.Jiang, M.-Y.Wu, L.Chen, Q.-H.Chen, M.-C.Hong. *Chem. Commun.*, **47**, 9861 (2011)
211. T.Pham, K.Forest, K.McDonald, B.Space. *Cryst. Growth Des.*, **14**, 5599 (2014)
212. W.Lu, D.Yuan, T.A.Makal, J.-R.Li, H.-C.Zhou. *Angew. Chem., Int. Ed.*, **51**, 1580 (2012)
213. J.Cai, X.Rao, Y.He, J.Yu, C.Wu, W.Zhou, T.Yildirim, B.Chen, G.Qian. *Chem. Commun.*, **50**, 1552 (2014)
214. B.Zheng, Z.Yang, J.Bai, Y.Li, S.Li. *Chem. Commun.*, **48**, 7025 (2012)
215. Y.He, Z.Guo, S.Xiang, Z.Zhang, W.Zhou, F.R.Fronczek, S.Parkin, S.T.Hyde, M.O'Keeffe, B.Chen. *Inorg. Chem.*, **52**, 11580 (2013)
216. B.Zheng, R.Yun, J.Bai, Z.Lu, L.Du, Y.Li. *Inorg. Chem.*, **52**, 2823 (2013)
217. X.Zhao, D.Sun, S.Yuan, S.Feng, R.Cao, D.Yuan, S.Wang, J.Dou, D.Sun. *Inorg. Chem.*, **51**, 10350 (2012)
218. X.Rao, J. Cai, J.Yu, Y.He, C.Wu, W.Zhou, T.Yildirim, B.Chen, G.Qian. *Chem. Commun.*, **49**, 6719 (2013)
219. T.Düren, L.Sarkisov, O.M.Yaghi, R.Q.Snurr. *Langmuir*, **20**, 2683 (2004)
220. D.Liu, H.Wu, S.Wang, Z.Xie, J.Li, W.Lin. *Chem. Sci.*, **3**, 3032 (2012)
221. L.Li, S.Tang, C.Wang, X.Lv, M.Jiang, H.Wu, X. Zhao. *Chem. Commun.*, **50**, 2304 (2014)
222. C.Tan, S.Yang, N.R.Champness, X.Lin, A.J.Blake, W.Lewis, M.Schröder. *Chem. Commun.*, **47**, 4487 (2011)
223. N.Klein, H.C.Hoffmann, A.Cadiau, J.Getzschmann, M.R.Lohe, S.Paasch, T.Heydenreich, K.Adil, I.Senkovska, E.Brunner, S.Kaskel. *J. Mater. Chem.*, **22**, 10303 (2012)
224. R.D.Kennedy, V.Krungleviciute, D.J.Clingerman, J.E.Mondloch, Y.Peng, C.E.Wilmer, A.A.Sarjeant, R.Q.Snurr, J.T.Hupp, T.Yildirim, O.K.Farha, C.A.Mirkin. *Chem. Mater.*, **25**, 3539 (2013)
225. D.Zhao, D.Yuan, A.Yakovenko, H.-C.Zhou. *Chem. Commun.*, **46**, 4196 (2010)
226. Z.Wang, B.Zheng, H.Liu, X.Lin, X.Yu, P.Yi, R.Yun. *Cryst. Growth Des.*, **13**, 5001 (2013)
227. A.D.Wiersum, J.-S.Chang, C.Serre, P.L.Llewellyn. *Langmuir*, **29**, 3301 (2013)
228. V.Bon, V.Senkovskyy, I.Senkovska, S.Kaskel. *Chem. Commun.*, **48**, 8407 (2012)
229. J.Y.Lee, L.Pan, X.Huang, T.J.Emge, J.Li. *Adv. Funct. Mater.*, **21**, 993 (2011)
230. T.K.Prasad, D.H.Hong, M.P.Suh. *Chem. – Eur. J.*, **16**, 14043 (2010)
231. Y.Wang, C.Tan, Z.Sun, Z.Xue, Q.Zhu, C.Shen, Y.Wen, S.Hu, Y.Wang, T.Sheng, X.Wu. *Chem. – Eur. J.*, **20**, 1341 (2014)
232. X.Duan, J.Yu, J.Cai, Y.He, C.Wu, W.Zhou, T.Yildirim, Z.Zhang, S.Xiang, M.O'Keeffe, B.Chen, G.Qian. *Chem. Commun.*, **49**, 2043 (2013)
233. B.Li, Z.Zhang, Y.Li, K.Yao, Y.Zhu, Z.Deng, F.Yang, X.Zhou, G.Li, H.Wu, N.Nijem, Y.J.Chabal, Z.Lai, Y.Han, Z.Shi, S.Feng, J.Li. *Angew. Chem., Int. Ed.*, **51**, 1412 (2012)
234. Y.-N.Gong, M.Meng, D.-C.Zhong, Y.-L.Huang, L.Jiang, T.-B.Lu. *Chem. Commun.*, **48**, 12002 (2012)
235. X.Liu, M.Park, S.Hong, M.Oh, J.W.Yoon, J.-S.Chang, M.S.Lah. *Inorg. Chem.*, **48**, 11507 (2009)
236. V.Krungleviciute, S.Pramanic, A.D.Migone, J.Li. *Microporous Mesoporous Mater.*, **161**, 134 (2012)
237. Y.He, W.Zhou, T.Yildirim, B.Chen. *Energy Environ. Sci.*, **6**, 2735 (2013)
238. Y.He, S.Xiang, Z.Zhang, S.Xiong, C.Wu, W.Zhou, T.Yildirim, R.Krishna, B.Chen. *J. Mater. Chem. A*, **1**, 2543 (2013)
239. Q.Yang, V.Guillerm, F.Ragon, A.D.Wiersum, P.L.Llewellyn, C.Zhong, T.Devic, C.Serre, G.Maurin. *Chem. Commun.*, **48**, 9831 (2012)
240. H.Kim, D.G.Samsonenko, S.Das, G.-H.Kim, H.-S.Lee, D.N.Dybtsev, E.A.Berdonosova, K.Kim. *Chem. – Asian J.*, **4**, 886 (2009)
241. I.Senkovska, F.Hoffmann, M.Fröba, J.Getzschmann, W.Böhlmann, S.Kaskel. *Microporous Mesoporous Mater.*, **122**, 93 (2009)
242. P.Rallapalli, D.Patil, K.P.Prasanth, R.S.Somani, R.V.Jasra, H.C.Bajaj. *J. Porous Mater.*, **17**, 523 (2010)
243. D.Tian, Q.Chen, Y.Li, Y.-H.Zhang, Z.Chang, X.-H.Bu. *Angew. Chem., Int. Ed.*, **53**, 837 (2014)
244. M.Anbia, S.Sheykhi. *J. Nat. Gas Chem.*, **21**, 680 (2012)
245. L.Li, S.Tang, X.Lv, M.Jiang, C.Wang, X.Zhao. *New J. Chem.*, **37**, 3662 (2013)
246. M.Xue, Y.Liu, R.M.Schaffino, S.Xiang, X.Zhao, G.-S.Zhu, S.-L.Qiu, B.Chen. *Inorg. Chem.*, **48**, 4649 (2009)
247. M.C.Das, H.Xu, Z.Wang, G.Srinivas, W.Zhou, Y.-F.Yue, V.N.Nesterov, G.Qian, B.Chen. *Chem. Commun.*, **47**, 11715 (2011)
248. Y.He, Z.Zhang, S.Xiang, H.Wu, F.R.Fronczek, W.Zhou, R.Krishna, M.O'Keeffe, B.Chen. *Chem. – Eur. J.*, **18**, 1901 (2012)
249. X.Zhao, X.Wang, S.Wang, J.Dou, P.Cui, Z.Chen, D.Sun, X.Wang, D.Sun. *Cryst. Growth Des.*, **12**, 2736 (2012)

250. H.J.Park, Y.E.Cheon, M.P.Suh. *Chem. – Eur. J.*, **16**, 11662 (2010)
251. R.Grunker, I.Senkovska, R.Biedermann, N.Klein, M.R.Lohe, P.Müller, S.Kaskel. *Chem. Commun.*, **47**, 490 (2011)
252. J.F.Eubank, H.Mouttaki, A.J.Cairns, Y.Belmabkhout, L.Wojtas, R.Luebke, M.Alkordi, M.Eddaoudi. *J. Am. Chem. Soc.*, **133**, 14204 (2011)
253. N.Klein, I.Senkovska, K.Gedrich, U.Stoeck, A.Henschel, U.Mueller, S.Kaskel. *Angew. Chem., Int. Ed.*, **48**, 9954 (2009)
254. K.Gedrich, I.Senkovska, N.Klein, U.Stoeck, A.Henschel, M.R.Lohe, I.A.Baburin, U.Mueller, S.Kaskel. *Angew. Chem., Int. Ed.*, **49**, 8489 (2010)
255. B.Li, H.-M.Wen, H.Wang, H.Wu, T.Yildirim, W.Zhou, B.Chen. *Energy Environ. Sci.*, **8**, 2504 (2015)
256. G.Q.Kong, Z.D.Han, Y.He, S.Ou, W.Zhou, T.Yildirim, R.Krishna, C.Zou, C.B.Hen, C.D.Wu. *Chem. – Eur. J.*, **19**, 14886 (2013)
257. R.B.Getman, Y.-S.Bae, C.E.Wilmer, R.Q.Snurr. *Chem. Rev.*, **112**, 703 (2012)
258. K.Konstas, J.W.Taylor, A.W.Thornton, C.M.Doherty, W.X.Lim, T.J.Bastow, D.F.Kennedy, C.D.Wood, B.J.Cox, J.M.Hill, A.J.Hill, M.R.Hill. *Angew. Chem., Int. Ed.*, **51**, 6639 (2012)
259. S.Yeganegi, V.Sokhanvaran. *Adsorption*, **22**, 277 (2016)
260. E.Frackowiak, F.Berguin. *Carbon*, **39**, 937 (2001)
261. S.J.Yang, J.Y.Choi, H.K.Chae, J.H.Cho, K.S.Nahm, C.R.Park. *Chem. Mater.*, **21**, 1893 (2009)
262. Z.Xiang, Z.Hu, D.Cao, W.Yang, J.Lu, B.Han, W.Wang. *Angew. Chem., Int. Ed.*, **50**, 491 (2011)
263. C.A.Grande, V.I.Agueda, A.Spjelkavik, R.Blom. *Chem. Eng. Sci.*, **124**, 154 (2015)
264. J.Ren, N.M.Musyoka, H.W.Langmi, A.Swartbooi, B.C.North, M.Mathe. *Int. J. Hydrogen Energy*, **40**, 4617 (2015)
265. S.Cavenati, C.A.Grande, A.E.Rodrigues, C.Kiener, U.Mueller. *Ind. Eng. Chem. Res.*, **47**, 6333 (2008)
266. N.Chanut, A.D.Wiersum, U.H.Lee, Y.K.Hwang, F.Ragon, H.Chevreau, S.Bourrelly, B.Kuchta, J.S.Chang, C.Serre, P.L.Llewellyn. *Eur. J. Inorg. Chem.*, 4416 (2016)
267. V.Finsy, L.Ma, A.L.Laert, D.E.DeVos, G.V.Baron, J.F.M.Denayer. *Microporous Mesoporous Mater.*, **120**, 221 (2009)
268. T.Tian, Z.Zeng, D.Vulpe, M.E.Casco, G.Divitini, P.A.Midgley, J.S.Albero, J.C.Tan, P.Z.Moghadam, D.Fairen-Jimenez. *Nat. Mater.*, **17**, 174 (2018)
269. F.Rezaei, S.Lawson, H.Hosseini, H.Thakkar, A.Hajari, S.Monjezi, A.A.Rownaghi. *Chem. Eng. J.*, **313**, 1346 (2017)
270. L.A.Darunte, Y.Terada, C.R.Murdock, K.S.Walton, D.S.Sholl, C.W.Jones. *ACS Appl. Mater. Interfaces*, **9**, 17042 (2017)
271. H.Thakkar, S.Eastman, Q.Al-Naddaf, A.A.Rownaghi, F.Rezaei. *ACS Appl. Mater. Interfaces*, **9**, 35908 (2017)
272. W.Y.Hong, S.P.Perera, A.D.Burrows. *Microporous Mesoporous Mater.*, **214**, 149 (2015)
273. Y.Chen, F.Chen, S.Zhang, Y.Cai, S.Cao, S.Li, W.Zhao, S.Yuan, X.Feng, A.Cao, X.Ma, B.Wang. *J. Am. Chem. Soc.*, **139**, 16482 (2017)
274. Y.Chen, X.Huang, S.Zhang, S.Li, S.Cao, X.Pei, J.Zhou, X.Feng, B.Wang. *J. Am. Chem. Soc.*, **138**, 10810 (2016)
275. M.Pinto, S.Dias, J.Pires. *ACS Appl. Mater. Interfaces*, **5**, 2360 (2013)
276. U.H.Lee, A.H.Valekar, Y.K.Hwang, J.S.Chang. In *The Chemistry of Metal-Organic Frameworks: Synthesis, Characterization, and Applications*. (Ed. S.Kaskel). (Weinheim: Wiley, 2016). P. 1449
277. J.Zhao, M.D.Losego, P.C.Lemaire, P.S.Williams, B.Gong, S.E.Atanasov, T.M.Blevins, C.J.Oldham, H.J.Walls, S.D.Shepherd, M.Browe, G.W.Peterson, G.N.Parsons. *Adv. Mater. Interfaces*, **1**, 1400040 (2014)
278. A.X.Lu, M.McEntee, M.A.Browe, M.G.Hall, J.B.DeCoste, G.W.Peterson. *ACS Appl. Mater. Interfaces*, **9**, 13632 (2017)
279. J.Shangguan, L.Bai, Y.Li, T.Zhang, Z.Liu, G.Zhao, Y.Liu. *RSC Adv.*, **8**, 10509 (2018)
280. M.I.Nandasiri, S.R.Jambovanea, B.P.McGrail, H.T.Schaef, S.K.Nune. *Coord. Chem. Rev.*, **311**, 38 (2016)
281. J.Ren, H.W.Langmi, B.C.North, M.Mathe. *Int. J. Energy Res.*, **39**, 607 (2015)
282. A.J.Graham, J.C.Tan, D.R.Allan, S.A.Moggach. *Chem. Commun.*, **48**, 1535 (2012)
283. O.Ardelean, G.Blanita, G.Borodi, M.D.Lazar, I.Misan, I.Coldea, D.Lupu. *Int. J. Hydrogen Energy*, **38**, 7046 (2013)
284. G.Blanita, I.Coldea, I.Misan, D.Lupu. *Int. J. Hydrogen Energy*, **42**, 3064 (2017)
285. T.R.C.Van Assche, N.Campagnol, T.Muselle, H.Terryn, J.Fransaer, J.F.M.Denayer. *Microporous Mesoporous Mater.*, **224**, 302 (2016)
286. Z.Wang, J.Liu, S.Grosjean, D.Wagner, W.Guo, Z.Gu, L.Heinke, H.Gliemann, S.Bräse, C.Wäll. *Chem. NanoMater.*, **1**, 338 (2015)
287. J.Ren, T.Segakweng, H.W.Langmi, B.C.North, M.Mathe. *J. Alloys Compd.*, **645**, S170 (2015)
288. P.Kusgens, A.Zgaverdea, H.G.Fritz, S.Siegle, S.Kaskel. *J. Am. Ceram. Soc.*, **93**, 2476 (2010)
289. D.Crawford, J.Casaban, R.Haydon, N.Giri, T.McNally, S.L.James. *Chem. Sci.*, **6**, 1645 (2015)
290. L.D.O'Neill, H.Zhang, D.Bradshaw. *J. Mater. Chem.*, **20**, 5720 (2010)
291. C.Rogers, D.Pun, Q.Fu, H.Zhang. *Ceramics*, **1**, 353 (2018)
292. A.N.Valekar, K.-H.Cho, U.-H.Lee, J.S.Lee, J.W.Yoon, Y.K.Hwang, S.G.Lee, S.J.Cho, J.-S.Chang. *RSC Adv.*, **7**, 55767 (2017)
293. F.Akhtar, L.Andersson, S.Ogunwumi, N.Hedin, L.Bergstroma. *J. Eur. Ceram. Soc.*, **34**, 1643 (2014)
294. C.Petit. *Curr. Opin. Chem. Eng.*, **20**, 132 (2018)
295. D.Bazer-Bachi, L.Assie, V.Lecocq, B.Harbuzaru, V.Falk. *Powder Technol.*, **255**, 52 (2014)
296. C.Petit, B.Mendoza, D.O'Donnel, T.J.Bandosz. *Langmuir*, **27**, 10234 (2011)
297. O.V.Solovtsova, A.V.Shkolin, I.E.Men'shchikov, M.K.Knyazeva, A.L.Pulin, A.A.Fomkin, A.Y.Tsivadze, O.E.Aksyutin, A.G.Ishkov. *Prot. Met. Phys. Chem. Surf.*, **55**, 826 (2019)
298. V.I.Agueda, J.A.Delgado, M.A.Uguina, P.Brea, A.I.Spjelkavik, R.Blom, C.Grande. *Chem. Eng. Sci.*, **124**, 159 (2015)
299. Z.Jia, H.Li, Z.Yu, P.Wang, X.Fan. *Mater. Lett.*, **65**, 2445 (2011)
300. M.Tagliabue, C.Rizzo, R.Millini, P.D.C.Dietzel, R.Blom, S.Zanardi. *J. Porous Mater.*, **18**, 289 (2011)

301. G.W.Peterson, J.B.DeCoste, T.G.Glover, Y.Huang, H.Jasuja, K.S.Walton. *Microporous Mesoporous Mater.*, **179**, 48 (2013)
302. S.Yuan, X.Sun, J.Pang, C.Lollar, J.S.Qin, Z.Perry, E.Joseph, X.Wang, Y.Fang, M.Bosch, D.Sun, D.Liu, H.-C.Zhou. *Joule*, **1**, 806 (2017)
303. T.D.Bennett, P.Simoncic, S.A.Moggach, F.Gozzo, P.Macchi, D.A.Keen, J.C.Tan, A.K.Cheetham. *Chem. Commun.*, **47**, 7983 (2011)
304. T.Asadl, M.R.Ehsanl, A.M.Ribeiro, J.M.Loureiro, A.E.Rodrigues. *Chem. Eng. Technol.*, **36**. 1231 (2013)
305. L.Arnold, G.Averlant, S.Marx, M.Weickert. *Chem. Ing. Technol.*, **85**, 1726 (2013)
306. J.Wegrzyn, M.Gurevich. *Appl. Energy*, **55**, 71 (1996)
307. H.Zhang, P.Deria, O.K.Farha, J.T.Hupp, R.Q.Snurr. *Energy Environ. Sci.*, **8**, 1501 (2015)
308. A.L.Myers, J.M. Prausnitz. *A.J.Ch.E. J.*, **11**, 121 (1965)
309. H.Furukawa, Y.B.Go, N.Ko, Y.K.Park, F.J.Uribe-Romo, J.Kim, M.O'Keeffe, O.M.Yaghi. *Inorg. Chem.*, **50**, 9147 (2011)
310. K.J.Chang, O.Talu. *Appl. Therm. Eng.*, **16**, 359 (1996)
311. Y.Muharam, E.Kusrini, N.Saubryani, M.Ulfa. *Int. J. Technol.*, **9**, 412 (2018)
312. V.A.Babenko, L.E.Kanonchik. *J. Eng. Phys. Therm.*, **73**, 3 (2000)
313. L.L.Vasiliev, L.E.Kanonchik, D.A.Mishkinis, M.I.Rabetsky. *Int. J. Therm. Sci.*, **39**, 1047 (2000)
314. D.Liu, J.J.Purewal, J.Yang, A.Sudik, S.Maurer, U.Müller, J.Ni, D.J.Siegel. *Int. J. Hydrogen Energy*, **37**, 6109 (2012)
315. A.Policicchio, R.Filosa, S.Abate, G.Desiderio, E.Colavita. *J. Porous Mater.*, **24**, 905 (2017)